

SUAS-SFM REMOTE SENSING OF RANGELAND VEGETATION: OBIA  
SEGMENT CLASSIFICATION AND STRUCTURAL PREDICTION OF  
PRICKLY PEAR CACTI IN CENTRAL TEXAS

by

Ethan L. Roberts, B.S.

A thesis submitted to the Graduate Council of  
Texas State University in partial fulfillment  
of the requirements for the degree of  
Master of Science  
with a Major in Geography  
August 2016

Committee Members:

Jennifer Jensen, Chair

Nate Currit

Yongmei Lu

**COPYRIGHT**

by

Ethan L. Roberts

2016

## **FAIR USE AND AUTHOR'S PERMISSION STATEMENT**

### **Fair Use**

This work is protected by the Copyright Laws of the United States (Public Law 94-553, section 107). Consistent with fair use as defined in the Copyright Laws, brief quotations from this material are allowed with proper acknowledgment. Use of this material for financial gain without the author's express written permission is not allowed.

### **Duplication Permission**

As the copyright holder of this work I, Ethan L. Roberts, authorize duplication of this work, in whole or in part, for educational or scholarly purposes only.

## **DEDICATION**

I dedicate this research to my beautiful and totally awesome wife whom continually inspires a soulful admiration for all things on God's green Earth.

## **ACKNOWLEDGEMENTS**

I would like to thank my graduate advisor Dr. Jennifer L. Jensen, whose mentorship and previous research in sUAS-SfM remote sensing with Dr. Adam J. Mathews and Dr. James T. Dietrich has guided and inspired the following research. I would also like to thank my wife Hailey Roberts whose hard work and rangeland field measurement precision goes unrivaled.

Lastly, this study was made possible through the Freeman Fellows Scholarship, a generous funding opportunity gifted to geography, agriculture, anthropology, and biology students from SWTSU alumni Mr. George Strait himself, specifically for those who wish to utilize the unique resources and ecology of the Freeman Center in order to pursue research goals.

## TABLE OF CONTENTS

	<b>Page</b>
ACKNOWLEDGEMENTS .....	v
LIST OF TABLES .....	ix
LIST OF FIGURES .....	x
CHAPTER	
1.0 INTRODUCTION.....	1
1.1 The Rangeland Problem and Data Collection Challenges.....	1
1.2 Rangeland Remote Sensing and Vegetation Modeling Limitations .....	6
1.3 sUAS-SfM Remote Sensing and Prickly Pear Cacti.....	11
1.4 SfM Processing and VHR Datasets.....	16
1.5 Problem Statement .....	18
1.6 Objectives .....	19
1.7 Justifications.....	20
2.0 LITERATURE REVIEW .....	21
2.1 sUAS-SfM Remote Sensing of Vegetation Structure .....	21
2.11 Non-forestry Related Research.....	21
2.12 Forestry Related Research.....	23
2.2 sUAS-SfM Topographic Studies and Error Identification .....	27
2.3 sUAS-SfM Optimization .....	31
2.4 OBIA Segmentation and Classification for Vegetation Analysis .....	33

3.0 STUDY SITE.....	36
3.1 Prickly Pear Cacti Morphology and Site Selection.....	36
3.2 Balcones Canyonlands Rangeland Site .....	37
4.0 DATA COLLECTION .....	43
4.1 Prickly Pear Cacti Field Measurements.....	43
4.2 GCP Design and GPS Measurements.....	47
4.3 sUAS Digital Image Acquisition.....	49
5.0 DATA PROCESSING .....	54
5.1 SfM Workflow .....	54
5.2 Generation of Dense Point Cloud.....	58
5.3 Generation of RGB Orthophoto .....	60
5.4 OBIA Segmentation and Random Forest Classification .....	63
5.5 Calculation of Predictor Variables .....	68
5.51 TIN-derived Volume and Surface Area Predictors .....	69
5.52 Point Height-derived Statistical Predictors .....	70
6.0 DATA ANALYSIS .....	72
6.1 Preliminary Statistical Analysis .....	72
6.2 MLR Model Training and General Evaluation .....	75
6.3 Final Model Selection.....	77
7.0 RESULTS AND DISCUSSION .....	80
7.1 Visual Characteristics of sUAS-SfM 3-D Datasets.....	80

7.11 Point Distribution and Elevation Results .....	80
7.2 Classification of Prickly Pear Cacti.....	92
7.21 RF-Classification and Detection Results .....	92
7.22 Classification Accuracy, Segment Geometry, and Structure .....	97
7.3 Prediction of Prickly Pear Cacti Structure.....	102
7.31 Predictive MLR Model Results .....	102
7.32 Plot Geometry, Selected Predictors, and Structure.....	110
7.4 Sources of Error and Limitations of Practical Application.....	114
8.0 CONCLUSIONS.....	118
APPENDIX SECTION .....	120
REFERENCES .....	124

## LIST OF TABLES

<b>Table</b>	<b>Page</b>
1. Field metric labels, equations and descriptions.....	46
2. Field metric descriptive and distribution statistics .....	47
3. GPS signal quality and dimensional precision for GCP/plot centerpoints .....	49
4. Flight plan collection parameters and digital image counts.....	51
5. Agisoft Photoscan report of GCP GPS positions vs. re-projection errors .....	56
6. Summary of dense point cloud properties.....	59
7. 1:1 plot-ellipse $R^2$ values: field metrics vs. descriptive predictors .....	74
8. 1:1 plot-ellipse $R^2$ values: field metrics vs. TIN-derived predictors .....	74
9. 1:1 plot-segment $R^2$ values: field metrics vs. segment/TIN-derived predictors .....	75
10. Summary accuracy report: training/testing phases of RF model.....	93
11. Confusion matrix and accuracy measures: training/testing phases of RF model.....	93
12. Confusion matrix for pixel-based accuracy assessment .....	94
13. Classification errors for pixel-based accuracy assessment .....	94
14. Results for plot-ellipse and plot-segment predictive MLR models.....	103

## LIST OF FIGURES

<b>Figure</b>	<b>Page</b>
1. Map of Balcones Canyonlands rangeland study site .....	39
2. Ground perspective images of study site .....	44
3. 3DR IRIS+ quadcopter sUAS .....	50
4. Flight plans 1 and 5 screenshots.....	52
5. Examples of sUAS digital stills.....	55
6. Examples of generated dense point cloud types.....	59
7. RGB orthophoto of BC study site.....	61
8. OBIA segments and RGB orthophoto .....	64
9. Combined dense point cloud.....	81
10. Point sum raster .....	82
11. Maximum point-Z TIN .....	86
12. Point-Z range raster .....	87
13. 3-D low oblique perspectives of dense point cloud and TIN.....	90
14. 2-D transects of dense point cloud.....	91
15. PP and non-PP thematic land cover map .....	96
16. Plot-ellipse detection graphs sorted by CLAD <sub>COUNT</sub> , PP <sub>HEIGHT</sub> , and ECC .....	100
17a. Predictive MLR models of field metrics: CLAD <sub>COUNT</sub> and PP <sub>HEIGHT</sub> .....	106
17b. Predictive MLR models of field metrics: ECC and ECV .....	107
17c. Predictive MLR models of field metrics: ECSA and FWB .....	108

17d. Predictive MLR models of field metrics: DWB.....	109
18. Sorted ascending graphs (actual vs. predicted): CLAD <sub>COUNT</sub> and PP <sub>HEIGHT</sub> .....	113

## 1.0 INTRODUCTION

### 1.1 The Rangeland Problem and Data Collection Challenges

While the definition of rangelands varies internationally as well in the U.S., rangelands can be defined as both land cover and land use (LCLU) areas that are dominated by a percentage of natural or introduced vegetation species typically below 5 m in height. This primarily includes common short statured species such as grasses, sedges, forbs, and cacti; though afforested and transitional rangelands in states of ecological change may exhibit encroachment from taller statured shrub and tree species not historically observed. Rangelands are thus ecosystems that characteristically support grazing and browsing activity from both wild and domesticated ruminants where they serve as natural resource areas that chiefly support grazing-based agronomies. Different from croplands which are anthropogenically controlled LCLU areas, rangelands are predominantly managed by the local ecology and require few external inputs (Lund 2007; Maynard et al. 2007; Reeves and Mitchell 2011).

This definition has also been expanded to include larger scale terrestrial biomes such as deserts, tundras, and steppes to more fine spatial scale regional rangeland types that are distinguished by dominant vegetation communities like the Pacific bunchgrass prairie and Texas oak savanna of the western U.S., or the Acacia bushland of South Africa (Pratt, Greenway, and Gwynne 1966). While numerous descriptors for different rangeland ecosystems exist, more recent and methodical ecological site descriptions (ESD) have sought to more meaningfully define unique local biophysical conditions at the study site scale by systematically recording key plant traits, soil properties, moisture regimes, and stages of ecological succession. ESDs in turn help to determine state-and-

transition models (STM), or models designed to follow a systematic understanding of positive or negative vegetation composition changes that are based on the documented conditions of ESDs over time. This in turn allows for reliable categorization and change detection analyses that can be performed at various scales for an important, complex, and changing biome (Boltz and Peacock 2007; Brown 2010; Talbot et al. 2010; Twidwell, Allred, and Fuhlendorf 2014).

Globally, rangelands are estimated to cover approximately half of Earth's terrestrial surface area though estimates are known to vary between definitions and sources of inventory (Follet, Kimble, and Lal 2001; Lund 2007; Eldridge, Greene, and Dean 2011). In the conterminous U.S. alone, rangelands have been estimated to cover approximately 33% (2.68 million km<sup>2</sup>) of the total land area (Reeves and Mitchell 2011), 60% (1.61 million km<sup>2</sup>) of which is privately owned (Follet, Kimble, and Lal 2001). Other countries like Australia, South Africa, and Argentina equally possess rangelands that occupy a large percentage of their total land mass, where like the U.S., they exist as vital natural resources for local and national economies primarily through the production of beef and mutton products from the grazing of cattle, sheep, and goats.

However, the sustainability of grazing-based agronomies which rely on the ecological health and productivity of rangeland vegetation is currently in question. A rising global population of approximately 7 billion people combined with the growth of a more affluent middle class in industrializing nations has resulted in an increase in demand for meat products. This steady rise in the global demand and supply of meat products has in turn placed further pressure on rangeland resources with already limited biological carrying capacities for both livestock and wildlife. Within the past century

there has also been an observed degradation of rangelands at the local, national, and global scales (Lund 2007; Bedunah and Angerer 2012; Sayre et al. 2012).

Historically, direct causes of rangeland degradation are well documented and have been long attributed in part to poor land management decisions such as overgrazing and overstocking (Milton et al. 1994; Cao et al. 2013; Villamil, Amiotti, and Peinemann 2001; Hilker et al. 2013). More complex and abstract causes such as climate change, desertification, poverty, and rural-urbanization have also been observed and discussed thoroughly in recent literature as part of a more interdisciplinary and holistic understanding of degradation processes (Milton et al. 1994; Duraiappah 1998; Glenn, Smith, and Squires 1998; Meadows and Hoffman 2002; McKreon et al. 2009; Wehrden et al. 2012; Easdale and Domptail 2014).

Similar to the degradation processes of other ecosystems, rangeland degradation can be effectively understood as an ecological downward spiral and positive feedback model that stems from resource input and output imbalances (biological, chemical, geological, etc.) that affect soil fertility. Once these imbalances reach a pivotal threshold beyond natural regenerative capabilities, they propagate further imbalances. When once healthy soil profiles progressively lose their biotic and abiotic fertility without a regenerative period or action, they eventually no longer support rangeland vegetation species, wildlife, livestock, or agronomic systems derived from them (Milton 1994; Briske, Fuhlendorf, and Smeins 2005; Bestelmeyer 2006; King and Hobbs 2006).

Therefore, understanding both negative and positive ecological changes while recognizing their tell-tale biogeochemical manifestations through systematic observation is a primary strategy for determining the multifaceted causes and solutions to rangeland

degradation. Careful monitoring allows land managers and policy makers the ability to act in the present, predict future outcomes, and make informed decisions for practical resource management strategies at local and national levels. As specified, many rangeland ecologists assigned ESD and STM categorizations to methodically describe specific rangeland site conditions, applying these observations to compare, understand, and track differences through time and space. However, collecting ESD and STM data for rangelands requires intensive field data collection efforts.

Traditionally, rangelands have proven to be difficult study areas in which to collect data and monitor change. Spatially, rangelands can occupy vast and remote areas that may encompass a complex range of environmental and socioeconomic conditions which can be difficult to represent in an efficient manner that utilizes traditional on-the-ground field collection techniques (West 2003; Mansour, Mutanga, and Everson 2012). For example, rangelands in the western U.S. like the sagebrush steppe ecosystem of the Great Basin span tens of millions of hectares and fall within multiple administrative regions, both public and private. Temporally, rangelands can also demonstrate rapid changes in relative biomass as many rangeland vegetation species such as grasses and sedges promptly respond to favorable conditions and negative trends like precipitation, extended drought, and wildfires. While natural changes in biomass due to phenology can be expected, it is difficult to account for the mosaic of differences that can occur on rangeland sites that are physically subdivided by topography, man-made features, and parent soils where a subtle difference may contribute to major inconsistencies in vegetation community types within a relatively small spatial scale (Fuhlendorf, Briske, and Smeins 2001; Bastin and Ludwig 2006; Amiraslani and Dragovich 2013; Sant et al.

2014).

As such, bottom-up land management schemes derived from even a well-represented collection of heterogeneous sample sites that are distributed across a single rangeland administrative region, may not successfully apply to the rangeland ecosystem as a whole because it is divided across multiple political boundaries with different administration systems, public or private. Similarly, data collection problems are compounded where rangeland ecosystems have been subdivided throughout history based on cultural and societal traditions of land management. Vast unfenced rangelands have become a subdivision of privately owned and fenced parcels that multiply through familial, legal, or political actions into consecutively smaller land holdings especially in areas where there have been rapid increases in land commercialization and rural urbanization rather than traditional agronomic land use activities.

The oak-juniper savanna in Texas and the bluegrass prairie in the Great Plains region are examples of well-developed ranchette-style rangeland sub-division where each parcel, along with any sub-divisions, can demonstrate a different land management or land use strategy that can be unrepresented or partially accounted for in field data collection samples. Likewise, data collection efforts become increasingly difficult for rangelands divided by a large number of private owners due to the need for legal consent and confidentiality agreement prior to many on-the-ground data collection efforts (Hilty and Merenlender 2003). Altogether, these data collection challenges cause difficulties in attempts to accurately extrapolate and model large scale rangeland health and degradation issues contributing to interdisciplinary gaps in rangeland science.

## **1.2 Rangeland Remote Sensing and Vegetation Modeling Limitations**

Over the past few decades, viable solutions to these data collection challenges have been to relate site-specific observations, such as those that have incorporated STM and ESD data, with data derived from remote sensing. The science of remote sensing and remote sensing systems is defined by the ability to collect physical data of the environment using remotely operated and deployed sensors such as multispectral cameras, laser scanners, and radar. Importantly, most remote sensing systems are thus spatially distant from their target of acquisition to provide increased data collection coverage whether the general target is Earth's surface or sub-surface features. For rangeland data collection, manned aerial or unmanned orbital remote sensing systems which operate at very high altitudes have allowed data collection with incomparable efficiency otherwise impossible from terrestrial perspectives.

The remote sensing of rangelands has traditionally utilized passive sensor systems, or systems designed to use sensors which rely on Earth's reflected solar energy for data collection. Passive remotely sensed data are then related to site-specific field data in order to further characterize rangeland conditions. This is typically accomplished by incorporating various image analysis methodologies such as pixel-based unsupervised and supervised land cover classification, band ratioing, principal component analysis (PCA), and tasseled cap analysis (TCA) (Hunt et al. 2003; Svoray, Perevolotsky, and Atkinson 2013; Higginbottom and Symeonakis 2014). Importantly, various studies have sought to use passive remote sensing systems to improve upon rangeland ESD and STM datasets. Hernandez and Ramsey (2013) employed PCA and the soil adjusted vegetation index (SAVI) to determine a similarity index that could describe nearby states of negative

transition for known ecological sites in the big sagebrush rangeland of northwestern Utah. Maynard et al. (2007) used Landsat 7 ETM+ imagery with tasseled cap analysis of known ESD locations to relate brightness, greenness, and wetness values to changes in field measured vegetation biomass and soil conditions of Montana rangeland. Similarly, Maynard et al. (2006) utilized Landsat 7 ETM+ imagery of Montana rangeland with non-transformed bands in a band-wise regression to account for changes in vegetation biomass. Therefore, a key aspect of many rangeland ecological analyses that use remote sensing to track biophysical changes within ESDs is the ability to associate site-scale plant measurements, such as leaf area index (LAI), plant height, or above ground biomass (AGB), to remote sensing imagery-based or range-based variables. Such relationships can in turn be used to not only estimate plant productivity and ecological transition, but to also examine other rangeland health factors such as biodiversity, habitat health, fuel-bed loads, and invasive or noxious species distribution, among many others.

While multispectral and hyperspectral imagery have been used to indirectly estimate rangeland biophysical vegetation properties, they can be limited for certain rangeland study objectives because most widely available multispectral and hyperspectral datasets have coarser resolutions such as the MODerate Resolution Imaging Spectroradiometer (MODIS), Landsat series, and even the higher resolution Satellite Pour l'Observation de la Terre (SPOT) series sensors. Specifically, coarser resolutions can make it difficult to quantify vegetation presence at the individual or species-level spatial scales, or the spatial scales related to ESD analyses (Booth and Cox 2008; Mansour, Mutanga, and Everson 2012). Conversely, higher resolution datasets, particularly those with spatial resolutions under 1 meter or very high resolution (VHR) datasets allow the

minute details of small vegetation communities or single plant physiognomies to become more distinguishable. This helps to separate and distinguish individual species, which can reveal more precise observations of ground cover, foliar cover, ecological succession, and the presence or absence of noxious or invasive species (Rango et al. 2009; Sant et al. 2014).

Higher resolution datasets also help to alleviate common arid rangeland vegetation classification challenges that are associated with spectral mixing, or the overlapping of soil and vegetation spectral signatures within a single pixel (Mansour, Mutanga, and Everson 2012). While federal and state funded aerial photography programs such as NAIP and NAPP exist in the U.S as potential options for multispectral VHR data collection of rangelands, they too can be limited by temporal resolution and availability for remote areas. Despite the utility afforded to rangeland analyses by multispectral and hyperspectral imagery, they are nonetheless limited to information recorded in two spatial dimensions, X and Y. In remote sensing of the environment, the addition of a third spatial dimension, Z or height, is extremely useful for more direct estimates of vegetation structure and biomass. Naturally 3-D datasets produced by active remote sensing systems offer a more realistic characterization of the horizontal and vertical distributions of plant architectures.

Traditionally, the measurement and modeling of rangeland vegetation structure at high spatial resolutions can be attributed to data derived from aerial or TLS systems. Aerial-Lidar or aerial laser scanner (ALS) remote sensing systems have been demonstrated to be particularly valuable for the quantification of certain vegetated land covers where vegetation species are dominated by tree-cover such as conifer, deciduous,

and tropical forests. Rangelands on the other hand, have proven to be more difficult data collection environments. Early studies such as Streutker and Glenn (2006) and Mitchel et al. (2011) were among the first to evaluate the capability of ALS to model rangeland vegetation structure where estimates of sagebrush height by a small footprint Lidar system demonstrated consistent underestimation that was attributed to the sensors sub-meter dimensional (horizontal and vertical) accuracy limitations. Similarly, Su and Bork (2006) and Spaete et al. (2011) found that small-footprint Lidar estimates for low lying vegetation and bare-earth digital elevation models (DEM) can be difficult due to minute slope and vegetation inconsistencies that are also below the horizontal and vertical thresholds of the sensor. Estornell, Ruiz, and Velázquez-Martí (2011) also found a considerable underestimation of vegetation height by ALS in Mediterranean shrub-land where shrubs below the average shrub height were difficult to quantify.

Although these studies have provided valuable evaluations of Lidar systems in varying rangeland environments, there are mutual limitations found throughout the literature that are indicative of the need for alternative solutions to rangeland remote sensing and the remote sensing of low-statured vegetation overall. For one, ALS by its very nature as a fast moving high altitude aircraft based system, tends to have a lower point density and post spacing that can lead to systematic height and plant detection and prediction inaccuracies. This is especially true for natural environments with variable vegetation canopy structures, wide dispersion of plant communities, and complex micro and macro topographies where point densities and post spacing that are too sporadic will inconsistently capture and effect accurate calculations of vegetation presence or structure.

Likewise, when the sub-meter dimensional accuracies are taken into account, the

combined sources of error can lead to difficulties in distinguishing vegetated cover from bare-earth returns, leaves from stems, and photosynthetically active vegetation from ground litter. For example, many arid rangeland ecosystems that are found in desert and mountain areas like parts of the Sonoran and Chihuahuan deserts possess complex micro-topographies with thin rocky soils where low lying vegetation cover can be exceptionally hard to distinguish from bare-earth surfaces. While more appropriate point densities or post spacing may be achievable using an increase in the pulse rate, scan line overlap, or the addition of a secondary flight plan, these actions can be overall inefficient and cost prohibitive for a given data acquisition or research objective. Overall, these technological and environmental challenges have demonstrably resulted in an underrepresentation of rangeland vegetation structure studies in existing literature.

As a solution, more reliable measurements of vegetation structure for rangeland vegetation are typically reserved for allometric on-the-ground measurements by hand or through the use of TLS or terrestrial laser scanners (TLS). TLS has the ability to produce extremely dense point clouds of hundreds to thousands of points/m<sup>2</sup> for individual vegetation species especially when acquired at close ranges with systematic overlapping scanning geometries. Studies that have utilized TLS systems with discrete return or wavelet analyses, have met with positive results. Olsoy, Glenn, and Clark (2014) and Olsoy et al. (2014) used TLS in order to estimate shrub biomass in an arid sagebrush-steppe ecosystem. Similarly, Vierling et al. (2013) used TLS with wavelet analysis in sagebrush steppe to examine sagebrush shrub height and canopy cover. In contrast, Sankey et al. (2013) used TLS to quantify the detailed vegetation canopy architectures of mesquite shrubland in the Sonoran desert in order to analyze shrub effects on minute

differences in aeolian sediment mounds and transportation.

However, much like ALS systems, TLS can be expensive and practically limited to non-destructive sampling at plot or stand scales as interpolation is generally needed for applications at larger scales. Alternative solutions have been to mount a compact TLS system to a small unmanned aerial system (sUAS) in order to mimic the benefits of aerial acquisition while retaining the benefits of increased point density and dimensional accuracy. While this option has shown future benefits, it is relatively impractical in its current technological state due to the weight of the payload, short flight durations, and the high cost of a sUAS malfunction (Wallace et al. 2012; Wallace 2013).

### **1.3 sUAS-SfM Remote Sensing and Prickly Pear Cacti**

Recently, a small-statured revolution in remote sensing has occurred in large part due to contemporary advances in the fields of robotics, computer processing, computer vision, and photogrammetry. Specifically, the novel development and employment of small unmanned aerial systems (sUAS) with digital aerial photographic techniques and structure-from-motion (SfM) photogrammetric processing has given rise to a technical and methodological fusion of “sUAS-SfM-based” or sUAS-SfM remote sensing. sUAS-SfM remote sensing has been demonstrated to be a possible solution to rangeland and low-statured vegetation remote sensing limitations primarily because it has the ability to produce dense and spatially accurate 3-D datasets similar to the point densities and dimensional accuracies produced from TLS, yet captured from the valuable aerial perspectives provided by low-altitude flight. This is practically accomplished by mounting consumer-grade digital point-and-shoot or DSLR cameras to low-cost multi-

rotor or fixed-wing sUAS airframes. When flown at low-altitudes manually or autonomously automated interval (time-lapse) stills or video photography can be used to produce a high number of overlapping images.

These images then serve as input data into open-sourced or proprietary SfM “pipelines”, a term that refers to an integrated workflow with distinct phases or steps which utilize multiple algorithms designed to generate 3-D positions (XYZ points) from 2-D data (XY/RGB pixel) through the calculation of keypoint positions or *structure* derived from camera pose data or *motion* (Oliensis 2000; Trucco and Verri 1998). The unique outputs of SfM pipelines used for remote sensing can consist of orthorectified or georeferenced high density point clouds, sub-decimeter digital surface models (DSMs), and orthophotomosaics. Recent studies in the fields of computer vision, geomorphology, forestry, and agriculture have already successfully demonstrated the viability of sUAS-SfM as a useful remote sensing tool through the evaluation of sUAS-SfM-derived digital terrain models (DTM) and canopy height models (CHM) for various land covers along with quantifiable comparisons to traditional datasets produced from TLS, ALS, GPS, and total station measurements. Still, sUAS-SfM remote sensing has yet to be fully assessed for the quantification and modeling of rangelands or rangeland vegetation species.

One of the most underrepresented rangeland plant family indicative of such rangeland remote sensing data gaps is the *Cactaceae* or cacti plant family, a family that contains 174 genera and 12,000 known species (The Plant List 2013). In the arid rangelands of North and South America, numerous *Cactaceae* species serve multifunctional roles that are pivotal to the life cycles of other plant and animal species. For instance, protected *Cactaceae* species like *Carnegiea gigantea* (saguaro cactus) or

*Lophophora williamsii* (peyote cactus) are rare, geographically isolated, sensitive to environmental change, and culturally significant (Godinez-Álvarez, Valverde, and Baes 2003). In particular, there are few more well-known and widely distributed *Cactaceae* species than those of the *Opuntia* genus, one of the largest *Cactaceae* genera with several species and sub-varieties that commonly share the name “prickly pear” or “wheel cactus”. While *Opuntia spp.* are originally native to North and South America, they have been introduced across the world for a variety of reasons both aesthetic and agricultural. In many countries such species have maintained a double-edged notoriety as either an indicator, keystone, or a noxious plant species for several reasons.

For one, many *Opuntia spp.* like *Opuntia engelmanni var. lindheimeri* (Engelmann’s prickly pear, Texas prickly pear), *Opuntia edwardsii* (Edward’s prickly pear), and *Opuntia polyacantha* (Plains prickly pear) possess an array of sharp spines surrounded by smaller spiny “hairs” that cover the plants cladodes (photosynthetic stem joints) and tunas (fleshy fruits). Though native wildlife has adapted strategies and physical traits to consume the plant’s cladodes, tunas, and flowers, non-native livestock are not adapted to or familiar with dealing with the plant’s natural defenses and can be severely harmed when they attempt to consume the plant; sometimes developing a fatal condition known as “pearmouth” (Hanselka and Paschal 1991; Ueckert 2015). Secondly, due to its growth cycle, *Opuntia spp.* can also occupy large areas of rangeland as they can reproduce and root successfully through cloning and pollination in a range of soil conditions, topography, and extreme temperatures thereby competing successfully for space with more palatable agronomic vegetation species (Hanselka and Paschal 1991; Agüero, Aguirre, Valiente-Banuet 2006; Hart and Lyons 2010; Ueckert 2015). Similarly,

when healthy rangeland soil profiles are progressively degraded, they may exhibit a high density of *Opuntia spp.* plants that have taken advantage of marginal soil conditions and a lack of competition from more agronomical herbaceous vegetation species (Hanselka and Paschal 1991). Over time, once grazable areas can feature such a dense distribution of *Opuntia spp.* plants that any movement by livestock into these areas is severely limited (Hart and Lyons 2010).

Efforts to remove *Opuntia spp.* and open up claimed areas to palatable grasses for grazing through mechanical, fire management, biological, or chemical means can be expensive, time consuming, and yield little long term results in certain areas where cuttings and seeds of the plant can root easily, lay dormant for long periods of time, and eventually reclaim lands left unmonitored (Hart and Lyons 2010; USDA 2012). In its native habitats, it has been observed that the natural distribution of *Opuntia spp.* was most probably controlled primarily by intense wildfires and successive factors that exploited the injured and defenseless cacti flesh like herbivory and insect action. However, as large scale fire management is rare or no longer prevalent on many rangelands where proper grazing does not necessitate a viable fuel load for burning *Opuntia spp.*, intense distribution can be troublesome (Vermeire and Roth 2011; Ueckert 2015).

In Texas, *Opuntia spp.* such as *O. engelmanni var. lindheimeri* along with similar variants maintain a dubious yet well respected reputation by local ranchers and rangeland conservationists, indicative of its symbolic representation as the state's official plant. During extended periods of drought, livestock and native wildlife come to depend on *Opuntia spp.* as emergency sustenance due to its high moisture, mineral, and energy

content (Guevara, Suassuna, and Felker 2009). Historically, ranchers throughout the southwestern U.S. have used it as emergency and supplementary fodder by simply burning away the harmful spines. In its native rangelands, the ecological value of *Opuntia spp.* is widely recognized and well documented as the plant provides food, water, shelter, and protective cover for numerous wildlife species.

The majority of the diets of the protected Texas tortoise (Scalise 2011) and the collared peccary (Everitt et al. 1981) are composed primarily of *Opuntia spp.*, especially during periods of the year when the fleshy tunas are abundant. The diets of economically important game animals like white tailed deer (Quinton, Horejsi, and Flinders 1979; Dillard et al. 2005), mule deer (Short 1977), sage grouse (Klebenow and Gray 1968) and Rio Grande turkey (Quinton and Montei 1977) as well as non-game species like black-tailed jackrabbits (Sparks 1968), coyotes (Meinzer, Ueckert, and Flinders 1975), and feral hogs (Taylor and Hellgren 1997) equally derive a significant portion of their diet from *Opuntia spp.* Aside from providing sustenance, *Opuntia spp.* provide shelter and nesting places for bird species like the roadrunner (Folse and Arnold 1978), cactus wren (Short 1985), and bobwhite quail (Hernandez et al. 2003) among various others. Due to its unique physiology, *Opuntia spp.* have been observed to foster the reseeding of overgrazed rangelands where they act as natural exclosures that protect palatable grass species from being consumed as they grow, mature, and seed within the confines of the plant's spiny foliar area (Ueckert 2015).

Altogether, the detection, mapping, and monitoring of *Opuntia spp.* characteristics at various spatial scales can yield a moderate assessment of rangeland health at multiple levels for rangeland managers based on the positive and negative

ecological functions of the plant itself.

#### **1.4 SfM Processing and VHR Datasets**

Specifically, sUAS-SfM remote sensing of prickly pear (PP) cacti is predicted to be effective based on the unique ability of modern SfM processing pipelines to:

- (1) Incorporate a high number of unordered, uncalibrated, and non-metric VHR images acquired from various altitudes and camera angles.
- (2) Reproduce minute spectral, textural, and spatial differences between individual PP cacti and surrounding vegetated/non-vegetated land cover.
- (3) Produce dense orthorectified point clouds that capture detailed structural characteristics useful for predictive modeling and analyses.

Though various SfM pipelines exist, each share a common workflow that can be divided into four basic phases: camera/sensor/lens coefficient or parameter estimation, feature detection and matching, keypoint estimation, and sparse point cloud densification. Depending on workflow design, different phases can also be executed in either a linear, hierarchal, or global framework which can utilize progressive feedback loops to continually refine and improve the geometric or dimensional accuracy of a reconstructed scene based on the continual introduction of more image data (Bemis et al. 2014; Crandall et al. 2013; Fonstad et al. 2013; Harwin and Lucieer 2012; Pintus and Gobbetti 2014; Previtali, Barazzetti, and Scaioni 2011; Tomasi and Zhang 1995; Wang 2011; Westoby et al. 2012).

In the first phase, intrinsic and extrinsic camera/sensor/lens parameters are estimated if unknown (uncalibrated) and include coefficients like focal length, principal,

point, and radial/tangential distortion. These parameters are then used to initially estimate relative 3-D camera pose, or the position and orientation of the camera in an exterior 3-D coordinate system. In the second phase, a Scale Invariant Feature Transform (SIFT), Speeded-Up Robust Features (SURF), or similar feature detection and matching algorithm is then used to distinguish and compare image features, or similar pixel(s) found in two or more overlapping images. Extracted feature matches can then be iteratively refined using the RANdom SAmple Consensus (RANSAC) algorithm or similar robust fitting algorithms designed to filter outlier matches and select best matches throughout single or multiple image pairs. In the third phase, the initial camera pose estimates are used alongside matched features to both refine camera pose estimates and calculate multiple external XYZ positions or keypoints, sometimes referred to as a sparse point cloud. In the fourth phase, a sparse point cloud can be densified by using Multi View Stereovision (MVS) algorithms which are designed to more efficiently interpolate a large number of points using image and camera pose data. As mentioned previously, the results from one phase can be used in another to refine final model accuracy and detail. For example, the initial estimates of camera pose, including camera/sensor/lens coefficients, can be refined by using the 3-D positions of keypoint estimates (Harwin and Lucieer 2012; Hödlmoser, Micusik, and Kampel 2013; Previtali, Barazzetti, and Scaioni 2011; Wendel, Irschara, and Bischof 2011).

While SfM pipelines can be computationally intensive depending upon the total number of input images and their image resolution (radiometric, spectral, and spatial), they can also be relatively automatic and require few input parameters that need to be specified by the user. In addition, most SfM pipelines do not require pre-calibrated

camera systems with known camera/sensor/lens coefficients in order to produce reliable (sub-decimeter) dimensional accuracies where heavier metric camera systems can overall hinder total flight time and can be costly to repair (Fonstad et al. 2013). Most SfM pipelines also allow the user a degree of control over output point cloud density which can allow for data processing flexibility that can be tailored to specific objectives.

Importantly, SfM processing of sUAS-based aerial imagery allows the production of several VHR datasets that are predicted to be suitable for the quantification of PP cacti at the species-scale based on the potential of these datasets to capture and represent the minutia of low-statured plant architectures and spectral characteristics in a virtual environment. Such datasets are projected to help delineate, classify, model, and predict vegetation structure more effectively and thus require further exploration and evaluation.

### **1.5 Problem Statement**

To date no direct studies have been published concerning the quantification of *Opuntia spp.*, or *Cactaceae spp.* structure using ALS, TLS, or sUAS-SfM remote sensing methods. In fact, no direct study is known regarding the quantification of rangeland vegetation structure using sUAS-SfM remote sensing. Of the few related studies that have used sUAS-acquired digital photography to study rangeland vegetation Laliberte, Rango, and Herrick (2006); Laliberte and Rango (2008); Rango et al. (2009); and Laliberte, Winters, and Rango (2011) mapped rangeland vegetation distribution while Laliberte and Rango (2009); Laliberte et al. (2010); and Laliberte and Rango (2011) utilized OBIA segmentation/classification to delineate rangeland vegetation at the species-scale.

Bryson and Sukkarieh (2011) is the only known study to use sUAS-acquired digital photography to specifically examine *Opuntia spp.* distribution at the species-scale where OBIA segmentation/classification was used to detect individual cacti in the Australian Outback. While these studies are among the first and most recent to demonstrate the value of sUAS and VHR datasets for the study of rangeland vegetation, they do not use sUAS-SfM methods to explicitly quantify rangeland vegetation structure. This is indicative of an overall lack of adequate literature on the subject in comparison to similar studies that have used ALS, TLS, and sUAS-SfM for analysis of vegetated land cover defined by high-statured tree dominant vegetation such as those of tropical, deciduous, or conifer forests.

## **1.6 Objectives**

The objective of this study is to detect and model the structure of PP cacti at the species-scale in an open-canopy rangeland ecosystem by utilizing several orthorectified VHR datasets derived from sUAS digital aerial imagery, SfM processing, OBIA segmentation, supervised machine learning classification, and predictive regression modeling. This study will also compare established point height-based (PH) modeling techniques refined in Lidar-based research with newer techniques that incorporate a fusion of PH-based data with object-based image analysis (OBIA) attributes that can exploit several sUAS-SfM derived datasets. Specifically, this study will concentrate on three primary objectives:

- (1) Generate sUAS-SfM-derived 3-D datasets and visually assess the representation of PP cacti and surrounding land covers.

- (2) Generate a sUAS-SfM-derived orthophoto for OBIA segmentation, classify segments using a machine learning algorithm, and assess accuracy.
- (3) Generate PH and OBIA segment-derived statistical predictors extracted from plot-ellipse and post-classified OBIA-segment dimensions in order to predict field metrics using multiple linear regression (MLR) models.

### **1.7 Justifications**

The proposed study ultimately seeks to find a practical and economic solution for the 3-D mapping of rangeland vegetation at site and species-scales through the use of sUAS-SfM remote sensing. The use of a more affordable and flexible remote sensing method that can acquire spatially accurate species-scale vegetation data on demand can be a vital tool for efficient rangeland monitoring, management, and conservation. Rangelands not only support dynamic ecological and agronomic functions, but they are rapidly changing in ways not fully understood where comparable monitoring efforts at such fine spatial scales using traditional remote sensing methods can be costly and prohibitive.

This study therefore seeks to first examine past methodologies and outline common limitations found in the literature and then elaborate on these established methods, present findings, and finally discuss key sources of error and practical limitations. This study also attempts to provide a reasonable proof of concept for future quantification of rangeland vegetation structure using sUAS-SfM.

## 2.0 LITERATURE REVIEW

### 2.1 sUAS-SfM Remote Sensing of Vegetation Structure

#### 2.11 Non-forestry Related Research

An early study by Turner, Lucieer, and Watson (2011) demonstrated the utility of sUAS-SfM methods for practical applications in the viticulture industry where the authors utilized a multi-rotor sUAS mounted with RGB, near-infrared (NIR), and thermal infrared (TIR) arrays fitted separately between three different flights. It was shown that sUAS-SfM could easily be used with manual georeferencing techniques to create DSMs and valuable vegetation index orthophotomosaics for on-demand VHR monitoring of soil and plant health. Similarly, Mathews and Jensen (2013) investigated the use of sUAS-SfM methods to quantify the leaf area index (LAI) for a near full veraison trellis-trained grapevine species, *Vitis vinifera*. Instead of more expensive multi-rotor or fixed wing sUAS, an inexpensive kite-wing sUAS was mounted with a point-and-shoot camera that was pointed at both nadir and low-oblique angles. The images were used to generate a manually georeferenced dense point cloud and multiple linear regression was used to estimate LAI, where moderate agreement was reported between SfM PH-derived statistical metrics and LAI field observations.

More recently, Zarco-Tejada et al. (2014) investigated the accuracy of sUAS-SfM-derived DSMs for the estimation of individual olive tree heights in an olive orchard. A fixed-wing sUAS was mounted with a converted RGB-to-color infrared (CIR) camera that was flown at an above ground height (AGH) of 200 meters using a high frequency overlapping flight plan. Estimates of maximum heights of individual olive trees were compared to heights derived from directly georeferenced DSMs that utilized different

raster resolutions designed to represent DSMs and subsequent height data from higher altitudes. The study reported that height estimates derived from DSMs with pixel resolutions between 5-35 cm yielded more accurate tree height predictions versus DSMs with coarser pixel sizes.

In contrast to agriculture-based investigations, early studies such as Lucieer et al. (2012) and Lucieer et al. (2014) instead examined the ecological applications for sUAS-SfM in a remote biome of the Antarctic coastline where both studies comprehensively evaluated both the accuracy and modeling capability of open-source SfM pipelines in combination with ecological growth models of Antarctic moss beds. In particular, Lucieer et al. (2012) used a multi-copter sUAS that was mounted with a digital single-lens reflex (DSLR) camera and a Tetracam multispectral (RGB/NIR) sensor that was flown at low AGHs in order to capture the spectral details and micro-topographies of moss beds. Lucieer et al. (2014) elaborated on the previous study by loosely coupling a similarly produced 2 cm resolution DSM with Monte Carlo simulations of hydrological algorithms in order to correlate water and nutrient availability with health and growth attributes of Antarctic moss samples. Importantly, both studies demonstrated the flexibility of sUAS-SfM to create valuable research products for remote environments where traditional remote sensing has exhibited limitations.

## 2.12 Forestry Related Research

An in-depth study by Dandois and Ellis (2010) used various datasets produced from a particular sUAS-SfM pipeline, Ecosynth, and compared them to similar datasets produced from ALS for mixed-deciduous New England forest study sites that represented a leaf-on or leaf-off phenology. The study used a multi-rotor sUAS that was equipped with a point-and-shoot camera that was flown over the study areas at approximately 40 m above the forest canopy using an overlapping parallel flight plan. The study compared sUAS-SfM and ALS produced bare-earth digital terrain model (DTM) and canopy height model (CHM) variables along with point-height derived statistical predictions of biomass and carbon-stock measurements. Additionally, SfM-derived vertical spectral profiles, or the spectral profiles of a study site's "ground-to-canopy" cross-section, was compared to MODIS NDVI time series green-up data. It was found that while sUAS-SfM DTM dimensional accuracies were comparable to ALS DTM accuracies for leaf-off phases, they were less accurate during leaf-on conditions. Similarly, sUAS-SfM CHMs that used ALS DTMs to derive height predictions of field observations were more accurate than sUAS-SfM CHMs derived from sUAS-SfM DTMs. Interestingly, sUAS-SfM vertical spectral profiles were reported to significantly correspond to MODIS NDVI data green-up data which demonstrated the utility of the RGB encoded sUAS-SfM dataset.

Lisein et al. (2013) compared sUAS-SfM and ALS produced CHMs at individual tree species, plot, and stand-scales for a leaf-on deciduous forest in Belgium using the European open-sourced MICMAC SfM pipeline. Instead of a multi-rotor sUAS, a commercial fixed-wing sUAS was mounted with a converted NIR camera and flown at an AGL of 225 m. Similar to Dandois and Ellis (2010), it was found that sUAS-SfM

CHMs and ALS CHMs were highly correlated overall, but at the plot and stand scales sUAS-SfM CHM heights slightly underestimated ALS CHM heights. However, at the individual tree or species-scale sUAS-SfM CHM-derived predictions of tree heights were more reliable than ALS CHM-derived predictions. Importantly, it was found that sUAS-SfM CHM prediction accuracies were largely affected by inconsistent point densities which caused sparse point clustering that resulted in the capture and misrepresentation of undergrowth heights rather than actual trees which systematically affected bare-earth DTM interpolation accuracies.

Instead of comparing ALS, Fritz, Kattenborn, and Koch (2013) compared sUAS-SfM with TLS by delineating individual tree stems from both dataset's point clouds for a leaf-off open canopy deciduous forest in southwest Germany. The study used established methodologies that incorporated horizontal slicing, point cluster extraction, and a RANSAC cylinder fit algorithm to generate tree stem geometries and subsequent variables such as stem radius. To best generate the dense point cloud that was needed, a multi-rotor sUAS was mounted with a compact systems digital camera that was angled 45° and flown at a AGH of 55 m using a bi-directional parallel flight plan with opposing image overlaps. Of the 102 trees present, the authors reported that 71% were successfully reconstructed using sUAS-SfM-derived tree stem estimates although estimates of tree radii were slightly lower than TLS estimates. Similar to point density irregularities experienced by Lisein et al. (2013), the study reported that sUAS-SfM tree stem estimates decreased when tree height increased which was explained by the presence of thinner stems that were not fully represented by sparse point clusters.

More recently, Sperlich et al. (2014) used an alternate tree delineation algorithm

designed for Lidar and forestry applications known as TreeVis in order to compare sUAS-SfM and TLS predictions of tree stem geometries for a leaf-on deciduous and conifer forest in Germany. A multi-copter sUAS mounted with a compact systems digital camera was flown at a AGH of 100 m using a nadir camera angle. They found that within the deciduous forest site there were strong relationships between sUAS-SfM-derived and TLS-derived maximum tree heights, highest tree density, and tree stem density estimates. However, individual tree detection rates were generally lower and were attributed to the greater variation in tree heights typical of deciduous forests. In contrast, the conifer stand exhibited stronger relationships between sUAS-SfM-derived and TLS-derived maximum tree height, height difference, and DTM difference where the bare-earth was easier to model between either dataset as explained by wider spacing between individual trees. Like previous studies, it was reported that sUAS-SfM product accuracies and detection probabilities increase for open-canopy leaf-off conditions as opposed to dense close-canopy conditions with greater undergrowth and limited line-of-sight (LoS) to bare-earth. Additionally, accuracies increase when forest types possess lower individual tree density, low horizontal tree crown distribution, and low tree height or crown cover heterogeneity.

Despite the inherent morphological differences of each forest type that was investigated, sUAS-SfM remote sensing methods have demonstrated useful predictions of commercial and ecological forest structural metrics at several analysis scales, each comparable or near comparable with aerial or terrestrial Lidar-derived structural metrics. Importantly, estimate accuracies have repeatedly demonstrated to be higher for leaf-on forests with sparse individual tree distribution and non-overlapping crown coverage.

Regarding the inherent differences between open-canopy rangeland ecosystems and forests, an important relationship exists between a study's objective and flight planning that must be considered for proper study design. For example, when the objective is to reconstruct individual tree structure, stem geometry, or a bare-earth surface for accurate CHM calculation it can be surmised from the above literature that sUAS flight plans executed during leaf-off conditions that employ low AGH altitudes and low-oblique or near-nadir camera angles are more preferable in order to capture unobstructed views of detailed vegetation architectures. On the other hand, when the study's objective is to predict metrics for larger scale study areas that are typical of ALS forestry-based research then perhaps the use of Lidar-derived DTMs with sUAS flight plans that use greater AGHs, digital compact-systems or DSLR cameras, and nadir camera angles is more viable.

Consequently, LoS challenges and irregular point-densities have shown to pose a key systematic limitation for the derivation of accurate vegetation structure metrics. In contrast, prediction metrics based on regularly distributed PHs have demonstrated to be more significant, especially for species-scale study objectives that require minute spatial detail. This is where TLS still exhibits a strong advantage due to the ability of high density laser pulses to penetrate foliage gaps and define hidden architectures.

## **2.2 sUAS-SfM Topographic Studies and Error Identification**

sUAS-SfM data collection strategies vary throughout the recent literature, as early evaluations of any technique or technology possesses little established doctrine that determine the most appropriate methods for a particular study's objective. Regardless, sUAS-SfM remote sensing strategies are based on several decades of research designs established in Lidar-related or MVS-related studies of vegetation and topography. This has resulted in common factors that have been applied in several disciplines, especially geomorphology, that sought to compare and improve sUAS-SfM product dimensional accuracies by identifying potential sources of error and curbing systematic error before and within the SfM workflow. This was accomplished primarily through trial-and-error examinations between separate studies that investigated different topographies (usually sparsely vegetated) utilizing methodical evaluations of sUAS-SfM-derived topographic datasets to well-established topographic datasets derived from Lidar, GPS, and total station measurements. The recognition and adaption of these factors is thus important for streamlining and optimizing sUAS-SfM remote sensing of rangeland vegetation and vegetation in general.

An early study by Harwin and Lucieer (2012) provided a comprehensive demonstration of important systematic errors that can be produced from the user-defined variations typical of sUAS-SfM methods. A multi-rotor sUAS mounted with a DSLR camera was repeatedly flown at an AGH of 30-50 meters using two nadir flight plans and one oblique flight plan over a sandy stretch of the Tasmanian coastline. The dimensional accuracies of three sUAS-SfM-derived point clouds were compared to real time kinematic differential GPS (RTK DGPS) and total station measurements. Point cloud

measurements were generated from several ground control point (GCP) centerpoint or GCP point cluster georeferencing (assignment of real world XYZ coordinates to arbitrary positions) variations based on: centroid vs. mean; semi-automatic georeferencing vs. manual georeferencing; total station vs. RTK DGPS ground truthing; and GCP design (size, shape, and distribution). Overall, it was reported that sUAS-SfM dimensional accuracies were higher for denser point clouds which allowed more accurate GCP centerpoint georeferencing and geotransformation (transformation of arbitrary positions to real world XYZ coordinate system) where the use of semi-automatic georeferencing with centroid-based GCP centerpoint calculations made it easier to recognize individual GCP point clusters. The study also found that a GCP distribution, which employed a high number of larger sized GCPs evenly distributed across the study area, ultimately helped to compensate for SfM modeling scene distortion that may occur in certain areas of the study site such as the outer edges.

Turner, Lucieer, and Watson (2012) also examined the effects of different sUAS-SfM-derived point cloud GCP centerpoint georeferencing techniques for the complex topography of a rocky Antarctic coastline. A multi-rotor sUAS mounted with a DSLR camera pointed at nadir was flown at an AGH of 50 m using an overlapping flight plan. The resulting dense point cloud's and their dimensional accuracies were compared between the point cloud produced from direct georeferencing (use of flight log-based sUAS GPS positions) and the point cloud produced from GCP-based georeferencing (use of flight log-based sUAS GPS and external GCP ground truth positions). It was reported that the range of dimensional accuracies for the GCP-based georeferenced point cloud resulted in 10-15 cm of difference versus 65-120 cm of difference from the direct

georeferenced point cloud.

In contrast, Fonstad et al. (2013) sought to compare sUAS-SfM-derived elevations with ALS-derived and GPS elevations for a section of limestone river bedrock in Texas. Instead of a multi-copter or fixed wing sUAS, a manually guided heli-kite platform mounted with a point-and-shoot digital camera was flown at variable AGHs of 10-70 meters. Instead of man-made GCPs, identifiable natural features in the limestone bedrock were used for post-flight georeferencing and geotransformation of the sUAS-SfM-point cloud. Using independent GPS positions that were not used for georeferencing, the study reported a mean elevation difference of 60 cm between sUAS-SfM and ALS versus a mean elevation difference of 44 cm between sUAS-SfM and differential GPS measurements. It was also surmised that the variable AGHs and near-random positioning of the windblown heli-kite platform contributed to the overall dimensional accuracy of the sUAS-SfM-derived point cloud. This was attributed to the ability of SfM processing to capitalize on a high number of images that share a high degree of image overlap relative to camera pose variability, or the number of different camera poses that are successfully modeled for a given target area.

Mancini et al. (2013) used an analogous study where sUAS-SfM-derived DSM elevations were compared to TLS-derived DSM elevations and RTK DGPS measurements for a sandy coastline in Italy. A multi-rotor sUAS mounted with a DSLR camera was flown at an AGH of 40 m where instead of traditional flat disc shaped GCPs, checkered 3-D cubes were distributed. The study reported a mean difference in dimensional accuracies of only 19 cm between the sUAS-SfM-derived DSM and the TLS-derived DSM while a mean difference of only 1 cm was reported between the

sUAS-SfM-derived DSM and the RTK DGPS measurements. In order to further test systematic errors caused by specific surface features, Mancini et al. (2013) also compared dimensional accuracies within four distinct zones: vegetated, non-vegetated, sand flats, and dynamic sand dunes. Overall, the study demonstrated that point densities and dimensional accuracy differences between sUAS-SfM and TLS were lower for flat sandy and non-vegetated zones. In contrast, the more topographically dynamic sand dune and vegetated zones yielded greater point densities but more disagreement between sUAS-SfM and TLS dimensional accuracies.

Tonkin et al. (2014) compared sUAS-SfM-derived DSM dimensional accuracies with total station measurements in the detailed micro-topography of a moraine-mound complex in North Wales. A multi-rotor sUAS mounted with a DSLR camera pointed at nadir was flown at an AGH of 100 m where a dense point cloud and detailed DSM were produced and compared to over 7,000 total station positions. The study reported a mean difference of 45.4 cm between sUAS-SfM-derived DSM and total station dimensional accuracies. Similar to Mancini et al. (2013), the study also compared dimensional accuracies between either dataset within two distinct topographic zones, grass and bedrock versus heather and shrubs. Importantly, it was demonstrated that denser vegetated zones yielded lower sUAS-SfM-derived DSM dimensional accuracies versus zones with little to no vegetation where the authors attributed the lower agreement to the sUAS mounted camera's LoS.

### **2.3 sUAS-SfM Optimization**

Aside from comparison evaluations of different topographic and vegetation structure datasets, past studies have collectively presented key limitations to sUAS-SfM remote sensing. Like previous remote sensing methods, some of these limitations are based on external and internal sources of error that systematically affect the ability of the technology to reproduce the complex geometries of real world features. While many sources of error are difficult to account for and are more an aspect of the technology itself, there are sources of error that have been reasonably identified and can be practically controlled by the user to improve overall SfM product accuracy. Specifically, there are three primary user-defined factors that have been observed to systematically influence accuracy: GCP design, point cloud density, and flight planning.

First, proper GCP design and georeferencing techniques have demonstrated to be a straightforward solution to preserving original scene or site geometries by curbing data collection sources of error (i.e. uneven illumination, image artifacts, noise, movement, etc.) that may cause inaccurate models of camera distortion or keypoint positions within the SfM pipeline itself. Adequately distributed and recognizable GCPs have repeatedly shown to be particularly vital during the geotransformation process where real world coordinates correct the arbitrary geometric models produced from the estimated camera pose data or any other SfM model derived from less accurate XYZ measurements of a camera's position during image acquisition, as exemplified in the flight-log GPS data evaluated in Turner, Lucieer, and Watson (2012). Additionally, the use of 3-D shapes like cubes, pyramids, cones, or identifiable natural features has shown to improve the identification of GCP centerpoints within the virtual environment so that they can be

georeferenced with less error. However, the accuracy of the ground truth data used for georeferencing an SfM model should always be considered with regards to the study objective.

Second, as discussed by Harwin and Lucieer (2012), Turner, Lucieer, and Watson (2012), and Fonstad et al. (2013), the choice to generate very dense point clouds or point clouds comparable to TLS outputs with mean point densities reaching between 50-100 points/m<sup>2</sup> has shown to alleviate several sources of error at the cost of computational efficiency. While “correction by densification” occurs at the cost of computational efficiency, denser point clouds generally allow the user to more easily identify GCP centerpoint clusters. Denser sUAS-SfM-derived point clouds also add more potential estimates of a target objects true shape which may alleviate LoS issues. For example, sUAS-SfM vegetation structure studies have shown that while penetration of foliage is limited or non-existent in many cases, extremely detailed representation of the external surface is significant where analysis techniques that capitalize on the “outer shell” of a plant may be more appropriate to predict structural metrics.

Moreover, the maximum point cloud density obtainable by a given sUAS image acquisition has shown to be proportional to general user-controlled factors within the data collection phase that include the percent of overlap between successive images, image acquisition interval, and the pixel-to-ground resolution or ground sample distance (GSD). Likewise, these parameters are controlled by other parameters set by the user during proper flight planning which include the sUAS airframe type, flight AGH, flight speed, camera angle, and camera lens/sensor type. Camera lens/sensor type in particular have been well recognized to be important in reducing dimensional errors post MVS

photogrammetric processing caused by radial or tangential distortion.

An insightful investigation by James and Robson (2014) employed simulations of different sUAS image acquisition geometries and radial lens distortions to help quantify these effects on resulting DSM dimensional accuracies. The study found that proper flight planning could effectively reduce many common DSM errors, especially for the automatic SfM pipelines that did not utilize known camera calibration parameters typical of expensive metric camera systems. Importantly, it was suggested that the utilization of converging oblique and nadir camera angles from different AGHs in combination with GCP-based georeferencing to be adequate user-controllable parameters for decreasing less controllable sources of error that stem from distortion.

#### **2.4 OBIA Segmentation and Classification for Vegetation Analysis**

Of the few studies that have used sUAS-based aerial photography to study low-statured vegetation, several have repeatedly demonstrated the value of incorporating OBIA segmentation-based techniques into their research analyses. Various studies have comprehensively evaluated intensity, hue, and saturation (IHS) values in combination with feature selection or attribute selection measures (Laliberte and Rango 2008; Browning, Laliberte, and Rango 2011), assessed the effects of appropriate segmentation scales on texture-based OBIA segment classification accuracies (Laliberte and Rango 2009), and investigated effects of OBIA segment classification strategies for different rangeland species compositions and structures at plot and species-scales (Laliberte et al. 2010).

Specifically, studies that have utilized OBIA segmentation of VHR sUAS-

acquired imagery in combination with machine learning classification algorithms that classify based on OBIA-segment-derived spatial, textural, or spectral attributes have shown it to be especially effective for the classification of arid rangeland vegetation using rule-based classification and Classification and Regression Tree (CART) based strategies (Laliberte, Winters, and Rango 2011; Laliberte and Rango 2011), the classification of weeds in maize fields using an auto-adaptive rule-based approach (Peña et al. 2013), and the classification and estimation of percent vegetation cover in a sagebrush-steppe rangeland also using a rule-based approach (Hulet et al. 2014).

Importantly, OBIA-based or OBIA segmentation/classification (unsupervised, semi-supervised, supervised, etc.) of vegetated land cover using VHR RGB imagery has proven to be a viable alternative to traditional unsupervised (ISODATA, K-means) or supervised (maximum likelihood, minimum-distance, parallelepiped) pixel-based classification methods that typically use coarse spatial resolution imagery with a high spectral resolution. Since low-altitude sUAS-acquired RGB imagery has spatial resolution but low spectral resolution, typically only three bands (RGB), OBIA segmentation/classification strategies instead seek to exploit the fine spatial details present through the calculation of multidimensional (spatial, textural, and spectral) attributes for individual OBIA segments. Multiple segment attributes can thus serve as a collection of unique descriptors for real-world land cover or land cover objects that can be classified distinctly or continuously (Volotão, Dutra, and Santos 2012; Volotão 2013).

Overall, OBIA segmentation/classification schemes become practical tools for sUAS-based studies that seek to minimize heavy payloads without sacrificing the ability to reliably classify vegetated land cover from inexpensive digital imagery (Laliberte and

Rango 2008). Regrettably few rangeland studies have investigated the advantages and disadvantages of certain segmentation/classification strategies for different land cover, how rangeland vegetation structure may effect classification accuracy, or whether OBIA segment geometries can be used to quantify rangeland vegetation structure.

### 3.0 STUDY SITE

#### 3.1 Prickly Pear Cacti Morphology and Site Selection

Prickly pear is a common name for several different species and varieties of *Opuntia platyopuntoids*, or *Opuntia spp.* that possess flat paddle-like cladodes. Throughout the southwestern U.S., PP cacti is a common name associated with several different species that grow 2-4 cm long spines and distinct red or purple oval-shaped fruits, or tunas. While exact species and sub-species genetic classification efforts for different *Opuntia spp.* are variable and ongoing, in the U.S. at least 31 species of *Opuntia sensu stricto* are estimated to exist (Grant and Grant 1979; Majure et al. 2012; Rebman and Pinkava 2001; Wang et al. 1998). In Texas, common species include *O. engelmannii* var. *lindheimeri* (Engelmann's prickly pear or Texas prickly pear), *O. edwardsii* (Edward's prickly pear), and *O. polycantha* (Plains prickly pear). With regards to the study's objective for a robust evaluation of sUAS-SfM remote sensing and modeling of PP cacti structure, a single study site was needed that could represent a heterogeneous sampling of PP cacti morphology based on the following reasons.

First, individual PP cacti found in a single site can possess significant physiological differences or very few physiological differences, regardless of age. This is because different varieties and hybrids of a particular *Opuntia spp.* can possess phenotypes that are exceedingly diverse from one another due to genetic factors like polyploidy, free hybridization, and backcrossing. Additionally, PP cacti can reproduce easily through cloning and seeding where a variety of heterogeneous or homogeneous hybrid swarms can occur between common Texas species such as *O. engelmannii*, *O. polycantha*, *O. macrorhiza*, and *O. lindheimeri* among others (Hart and Lyons 2010;

Grant and Grant 1979; Grant and Grant 1982; Powell and Weedin 2001; Wang et al. 1996). PP cacti can also respond rapidly to favorable or unfavorable environmental conditions by shedding old cladodes or growing new cladodes; changing the shape and structure of plants within a relatively short time period. Therefore, a study site that possessed an adequate number of heterogeneous plants to sample was favored.

Secondly, PP cacti is rather hardy and can be found in a wide variety of healthy or poor range conditions, growing in close proximity to other vegetation species that are in different stages of ecological succession or phenology. For example, various short to tallgrass species have been observed to have a close life cycle relationship with PP cacti. Sometimes these other vegetation species exceed the maximum heights of nearby PP cacti obstructing clear views of them from certain ground and aerial perspectives. As such, results derived from photogrammetric-based methods that rely on a relatively clear LoS to reliably capture and model structure, may be different for vegetation heights typical of early seral, or grazed rangelands versus taller vegetation heights found in fallow or climax rangelands. To account for a worst case rangeland data collection scenario and meet the study's need for robust modeling potentially applicable to other study sites, a study site was selected that represented rangeland with tall vegetation heights in near-climax relatively ungrazed conditions.

### **3.2 Balcones Canyonlands Rangeland Site**

The Balcones Canyonlands (BC) study site (29° 55' 23.72" N/97° 58' 39.29" W) is located within the Freeman Center, a 1,701 ha enclosed research area operated by Texas State University located in the southeastern portion of Hays County approximately

5 kilometers west of the city of San Marcos in south central Texas (Fig. 1). The BC study site lies within the Balcones Canyonlands, an approximately 4,300 km<sup>2</sup> sub-ecoregion within the eastern portion of the larger Edwards Plateau ecoregion, an area that encompasses approximately 95,000 km<sup>2</sup> from north central to south central Texas (Amos and Gehlbach 1988; Griffith et al 2007; Ricketts et al. 1999). The Balcones Canyonlands is characterized by its dynamic karst topography that features rolling flat-topped mesa-like hills with stair step-like terraces that can be starkly interposed by the steep eroded slopes of narrow perennial stream valleys, draws, and limestone cliffs typical of this flash flood prone region. Hillsides and higher sloped areas within the Balcones Canyonlands exhibit thin, rocky, calcerous soils that can support dense closed-canopy Ashe juniper (*Juniperus ashei*) dominated stands as well as more open-canopy conditions with a mix of common woody shrubs: Agarita (*Berberis trifoliolata*), Texas persimmon (*Diospyros texana*), and Yaupon holly (*Ilex vomitoria*); Cacti and succulents: Texas prickly pear varieties (*O. engelmannii*, *O. linheimeri*), Tasajillo (*Cylindropuntia leptocaulis*), Spanish Dagger Yucca (*Yucca constricta*); forbs: Texas broomweed (*Gutierrezia texana*), Wolfweed (*Leucosyris spinosa*), Common goldenweed (*Iscoma coronopifolia*), Texas croton (*Croton texensis*), and short to midgrasses: Texas grama (*Bouteloua rigidiseta*), Buffalo grass (*Buchloe dactyloides*), Little bluestem (*Schizachyrium scoparium*), Texas wintergrass (*Nasella leucotricha*).

In contrast, the deeper loamier soils of the savannah-like upland pastures and lowland valleys typically support older growth Live Oak (*Quercus fusiformis*) and Texas Cedar Elm (*Ulmus crassifolia*) dominated mixed tree stands with an abundance of other midgrasses: Red grama (*Bouteloua trifida*), Sideoats gramma (*Bouteloua curtipendula*),

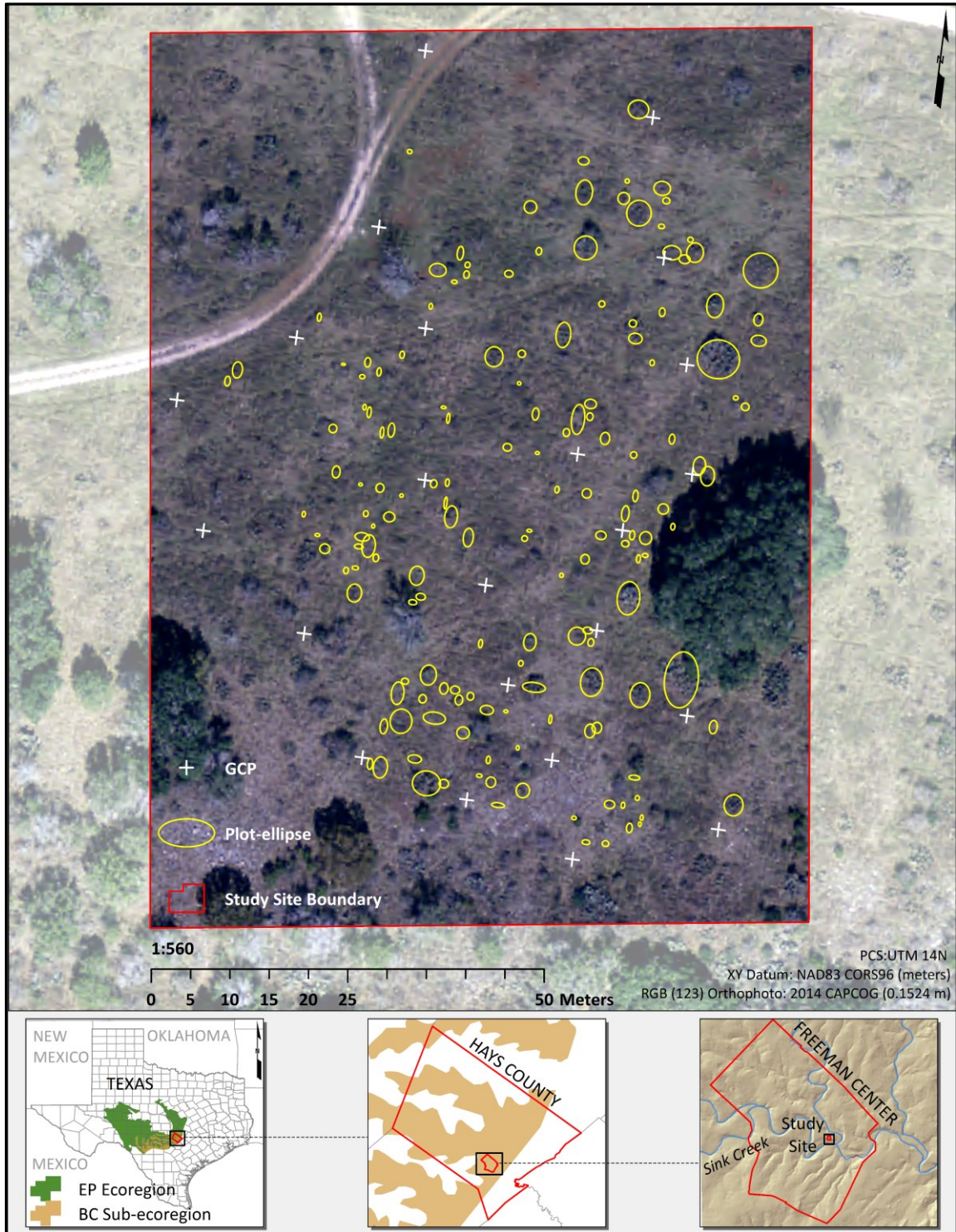


**Figure 1.** Map of Balcones Canyonlands rangeland study site. Located within the Freeman Center, TSU, Hays County, Texas, USA.

Hairy grama (*Chondrosum hirsutum*); and tallgrasses: Big bluestem (*Andropogon gerardii*), Silver bluestem (*Bothriochloa saccharoides*), Switchgrass (*Panicum virgatum*), Yellow Indiangrass (*Sorghastrum nutans*). Such areas have been historically utilized for grazing and haying activities but more recently viticulture has been introduced to the region.

The general area that encompasses the study site possesses thin Mollisol dominant, very cherty clay loam soils up to 25.4 cm in depth and typical of the local Ruple-Comfort and Comfort-Rock soil complexes that nonetheless support nearby old growth tree stands of Live Oak, Cedar elm, and Ashe juniper fragmented by 1-2 ha sized meadows (USDA 1984; SSURG0 2015). The study site itself is an open-canopy meadow that is located on the southwestern facing aspect of a hill and 30 m north of a small limestone bluff. The bluff rises between 20-30 m in elevation above the northern and southern conjoining branches of Sink Creek, a small intermittent streambed that leads into a manmade flood control drainage basin which eventually feeds into the San Marcos River 5 km downstream. The study site boundaries encompass an area of approximately 9955.85 m<sup>2</sup> (0.99 hectares) with an average slope of 0.35% from the northern to southern boundary within an elevation range of approximately 215 m - 235 m ASL.

Precipitation received prior to field data collection was recorded by the nearest NOAA weather station 2.7 km to the east and reported approximately 81.4 cm of rainfall between January 1, 2015 to June 30, 2015 with the month of May receiving a record rainfall of approximately 32 cm (Freeman Center 2015). Precipitation values altogether yielded a much wetter than average early summer that prompted an abundance of herbaceous vegetation growth for the area in comparison to previous drier than average

years. Vegetation species identified within the study site's boundaries consist of common short to tallgrass species: Texas grama, Texas wintergrass, Big bluestem, Little bluestem; Forbs: Texas broomweed, Texas croton, Texas thistle, Largeleaf lantana (*Lantana camara*), Wild carrot (*Daucus carota*); shrubs: Agarita, Texas persimmon, Yaupon holly; trees: Live Oak, Huisache (*Acacia farnesiana*), Sugar Hackberry (*Celtis laevigata*); and cacti and succulents: Texas prickly pear, Tasajillo, Lace hedhehog cactus (*Echinocereus reichenbachii*), Spanish Dagger Yucca.

Regarding the relationship between non-target vegetation heights and PP cacti heights, the tallgrass and midgrass species tend to exceed the maximum height of cladodes in the northern half of the study site; while in the southern half of the study site PP cacti, Tasajillo, Texas persimmon, and Agarita plants remain predominantly the tallest species present. This is most likely explained by the thinner rockier soil profile of the southern half of the study site which supports a sparser scattering of shortgrass and midgrass species. In addition, PP cacti dispersion in the northern half is observed to be more even and spread out between individual plants. Generally, larger PP cacti were observed to be in the eastern portion with smaller plants in the western portion where individual plant spacing steadily decreased further south and downslope.

Notably, the BC study site possessed a well-represented range of morphological differences typical of the surrounding region within a mature rangeland. This was exhibited by the early summer presence and health of an array of native forage and wildlife species in addition to the lack of any signs of overgrazing or detrimental hoof action, flooding, fire, or drought. Importantly, the dimensions and total area that comprised the study site represented a manageable area (0.99 ha) suitable for projected

sUAS flight times and data processing limitations.

## 4.0 DATA COLLECTION

### 4.1 Prickly Pear Cacti Field Measurements

Non-destructive field measurements for individual PP cacti plots occurred between June 6-7, 2015. Prior to actual measurements, the study site's boundaries were delineated by first flagging the center mass of all distinct and separate PP cacti patches, or potential plots, within the general area of the study site. GCPs were then evenly distributed throughout the study site based on the locations of flagged PP cacti patches. A provisional study site boundary was then delineated that encompassed enough individual patches to necessitate an adequate sample size for statistical analysis and proper sUAS flight planning.

Since multiple PP cacti can sometimes grow together and occupy a single patch, making it hard to discern separate plants, a single patch was counted as an individual plot. In most occurrences evidence for numerous individual cacti per patch was scarce, especially for smaller patches. Patches which possessed fewer than 7 cladodes were excluded from the study. This was done because the majority of individual PP cacti with fewer than 7 cladodes observed within the study site were either newly grown and possessed small immature buds, or were in poor health and possessed dry shed cladodes that approximated the maximum height of ground litter. In total 164 plots were flagged to be measured.

Due to the high number of plots, field measurements followed a strict methodology to improve data collection efficiency and field metric accuracy. First, the

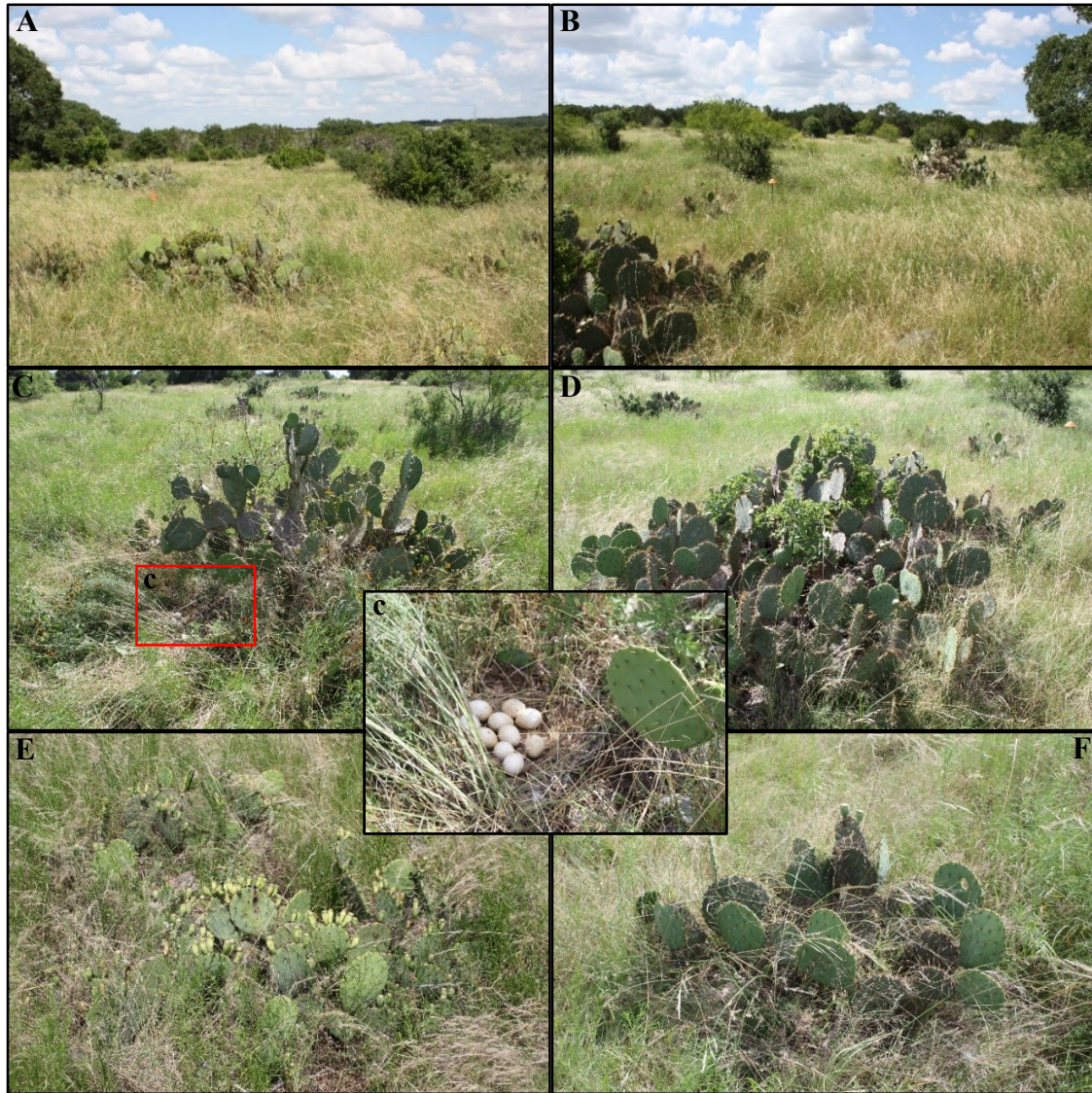


**Figure 2.** Ground perspective images of study site. (A) North-to-south view. (B) South-to-north view. (C)(D)(E)(F) Show differences between individual PP cacti and surrounding vegetation regarding size, shape, height, and color. (C)(c) Demonstrate a PP cacti serving as an early summer brooding site for Rio Grande turkeys as a clutch of eggs (c) can be seen incubating.

greatest horizontal extent of cladodes in the north-to-south (N/S) and east-to-west (E/W) directions was determined in order to establish the maximum foliar coverage of each plot. The lengths of each axis were then measured and recorded. Second, the conjunction of the N/S and E/W axes, or the centerpoint of each elliptical plot, was determined and

flagged for later GPS measurements of plot centerpoints. Third, the maximum height of foliage within each plot was measured by first determining the tallest cladode within the plot and then measuring the height from the top of that cladode to the bare-earth directly beneath the cladode. Lastly, the total number of cladodes for each plot was recorded by taking the mean of three separate counts.

While counting cladodes from smaller patches can be straightforward, a mean counting strategy was adopted in order to reduce miscounting errors when trying to identify and account for individual cladodes within larger patches that possessed multiple horizontal and vertical layers. A cladode was counted as a single cladode only when it was evident that it was separate from adjoining cladodes morphologically. This was done by examining the individual cladode shape and the location of cladode nodes which can be found at the narrow base of a cladode as it joins to another cladode's growing point, or the wider area at the top of a cladode. Small, newly developed cladode buds and dead cladodes that had been shed were excluded from the total count.

Field measurements of each plot were then used to calculate a total of 7 field metrics which included total cladode count ( $CLAD_{COUNT}$ ), maximum PP cacti height ( $PP_{HEIGHT}$ ), elliptical crown coverage (ECC), ellipsoidal crown volume (ECV), ellipsoidal crown surface area (ECSA), fresh weight biomass (FWB), and dry weight biomass (DWB). Equations and methods used to calculate each field metric are provided in Table 1. FWB and DWB were calculated utilizing equations derived from previous studies that used *O. ellisiana* samples (n=50) to calculate FWB (Han and Felker 1997) and *O. engelmannii* samples (n=26) to calculate DWB (Vogl et al. 2004). A summary of field metric descriptive and distribution statistics for final observations used in statistical

**Table 1.** Field metric labels, equations, and descriptions.

<b>Metric Label</b>	<b>Description/Equation</b>
<b>CLAD<sub>COUNT</sub></b>	<i>Cladode count</i> : the total number of cladodes per plot; determined using the mean of 3 separate counts.
<b>PP<sub>HEIGHT</sub></b>	<i>Prickly pear height</i> (m): the maximum height of the tallest cladode found per plot; measured from bare-ground to the top of cladode.
<b>ECC</b>	<i>Elliptical crown coverage</i> (m <sup>2</sup> ): the total elliptical area per plot designating a plot-ellipse; calculated using the greatest horizontal extent (N:S/E:W radii) of cladodes $ECC = \pi ab$ where: a = N:S radius (m); b = E:W radius (m)
<b>ECV</b>	<i>Ellipsoidal crown volume</i> (m <sup>3</sup> ): the hemispherical-ellipsoidal volume per plot; calculated for the above-ground portion of the plant or 1/2 the full-ellipsoidal volume. Uses the maximum plant height as the vertical radius. $ECV = \frac{\left[ \frac{4}{3} \pi (abc) \right]}{2}$ where: a = N:S radius (m); b = E:W radius (m); c = PP <sub>HEIGHT</sub> (m)
<b>ECSA</b>	<i>Ellipsoidal crown surface area</i> (m <sup>2</sup> ): the hemispherical-ellipsoidal surface area per plot; calculated for the above-ground portion of the plant or 1/2 the full-ellipsoidal surface area. Uses the maximum plant height per plot as the vertical radius. $ECSA = \frac{\left[ \left( \frac{4}{3} \pi (a^p b^p + a p c p + b p c p) \right) \frac{1}{p} \right]}{\frac{3}{2}}$ where: a = N:S radius (m); b = E:W radius (m); c = PP <sub>HEIGHT</sub> (m); p= 1.6075
<b>FWB</b>	<i>Fresh-weight biomass</i> (Kg): the above ground undried plant biomass per plot; calculated from equation by Han and Felker (1997) based on (n=50) <i>O. ellisiana</i> samples. Uses the total number of cladodes for each plot. $FWB = -1.466 + 0.407(CLAD_{COUNT})$
<b>DWB</b>	<i>Dry-weight biomass</i> (Kg): the above-ground dried plant biomass per plot; calculated from equation by Vogl et al. (2004) based on (n=26) <i>O. engelmannii</i> sample. Uses the maximum plant height and the longest horizontal diameter of each plot. $DWB = \frac{(4.189r^3)^{0.965}}{10^5}$ where: r = $\frac{\left[ \left( \frac{PP_{HEIGHT}}{2} \right) + \left( \frac{longest\ diameter}{2} \right) \right]}{2}$

**Table 2.** Field metric descriptive and distribution statistics (n=155).

Dependent (Y)	Descriptives				Distribution	
	$\bar{X}$	Min.	Max.	SD	Skew	Kurt.
CLAD <sub>COUNT</sub>	58.97	7	389	68.11	2.67	7.87
PP <sub>HEIGHT</sub> (m)	0.55	0.19	1.55	0.22	1.53	3.37
ECC (m <sup>2</sup> )	1.64	0.10	15.34	2.16	2.92	11.66
ECV (m <sup>3</sup> )	0.79	0.02	9.88	1.38	3.51	15.36
ECSA (m <sup>2</sup> )	1.62	0.18	9.81	1.57	2.39	6.99
FWB (Kg)	22.54	1.38	156.86	27.72	2.67	7.87
DWB (Kg)	6.12	0.13	71.71	9.95	3.31	14.31

analysis is provided in Table 2.

#### 4.2 GCP Design and GPS Measurements

After flagging PP cacti patches, 23 GCPs were evenly distributed near the outer edges and within the center of the rectangular area of the study site following suggested GCP quantity and distribution patterns (Harwin and Lucieer 2012; James and Robson 2014) (Fig. 1). Instead of placing GCPs along a strict grid pattern, GCPs were strategically positioned in areas with low vegetation heights and low overhead cover when compared to surrounding areas. This was done so GCPs could be more visible from low-oblique and nadir camera angles during sUAS image acquisition and within a virtual environment for georeferencing and geotransformation later.

Similarly, two different individual GCP designs were incorporated in order to potentially improve identification and compensate for visibility effects from non-target vegetation heights. The 19 GCPs that were distributed on the outer edges of the study site consisted of open-top orange track cones that measured 20 cm in diameter by 5 cm in height and were capped with a 7.62 cm in diameter white foam sphere. To overcome

tallgrasses and the slight hill present in the center of the study site, 4 taller GCPs were distributed in the center and consisted of steep sided closed top track cones that measured 6 cm in diameter by 8cm in height. All GCPs were staked to the ground with 30-60 cm tall wooden stakes to prevent any movement by strong winds and to provide increased visibility. The heights of all GCPs were recorded using a level rod that measured the distance from their base at ground level to GCP centerpoint height, or the top-center of each foam sphere or closed top cone. Recorded GCP heights were later added to GPS measured elevations taken at ground level at the direct base of each GCP centerpoint to calculate true GCP centerpoint elevations.

GPS measurements of GCP centerpoints and plot centerpoints utilized a Trimble GeoXH 2008 series GPS receiver and Zephyr antenna with manufacturer reported post-processing dimensional accuracies within the sub-decimeter range. All GPS measurements incorporated accuracy based real-time correction logging with maximum position (3-D) dilution of precision (PDOP) and dimensional accuracy settings no greater than 4 and 40.0 cm for GCPs and 5 and 50.0 cm for plot centerpoints respectively. Positional logging of individual GCP centerpoints was taken at ground level positions directly beneath the GCP centerpoints and used 300 averaged positions per GCP centerpoint. In contrast, each plot centerpoint used 50 averaged positions to increase data collection efficiency per the 164 plots. Differential post-processing corrections used Trimble Pathfinder Office software which incorporated 5 of the nearest local base stations no more than 25 km from the study site. The resulting differential post-processing output of GPS positions reported acceptable mean horizontal and vertical precisions for GCPs at 8.1 cm (XY) and 8.2 c (Z) respectively. Mean horizontal and

**Table 3.** GPS signal quality and dimensional precision for GCP/plot centerpoints.

Descriptives		Max. PDOP	Max. HDOP	XY-Prec. (m)	Z-Prec. (m)	SD (m)
<b>GCP (n=24)</b>	$\bar{X}$	2.7917	1.2833	0.0811	0.0822	0.0309
	Max.	3.9000	1.6000	0.0818	0.0924	0.0659
	Min.	2.2000	1.0000	0.0807	0.0808	0.0145
	SD	0.4499	0.1748	0.0003	0.0025	0.0139
<b>Plot (n=155)</b>	$\bar{X}$	2.5159	1.1809	0.0778	0.0758	0.0213
	Max.	4.2000	2.3000	0.1558	0.0840	0.0881
	Min.	1.8000	0.9000	0.0494	0.0444	0.0041
	SD	0.4215	0.2300	0.0129	0.0130	0.0123

vertical precisions for plot centerpoints were reported at 7.8 cm (XY) and 8.4 cm (Z) respectively (Table 3).

#### 4.3 sUAS Digital Image Acquisition

Aerial imagery was acquired within a two-hour period on June 10, 2015 from 1:00-3:00 PM during maximum solar zenith angles (18 °-10 °) with less than 10% rolling cloud cover and average wind speeds of 1.6 kph-2.3 kph (0.80 kn-0.70 kn) out of the southeast to southwest (Freeman Center 2015). With regards to the environmental conditions, this optimal period was chosen in order to stabilize the spatial and spectral values of pixels from image to image and flight plan to flight plan by seeking to minimize major variances in solar illumination and the wind’s movement of vegetation foliage.

Digital still images (3:4 format, 3/3,000 x 4,000 pixels) were acquired by utilizing a customized 12 MP 1/2.3” CMOS sensor GoPro4 Black action camera whose original fisheye lens was removed and interchanged with a commercially available M12 3.6 mm low distortion lens (manufacturer reported optical distortion<0.35 %). This particular lens was selected because it produced more rectilinear digital stills and possessed



**Figure 3.** 3DR IRIS+ quadcopter sUAS. (A) 3DR IRIS+ prior to takeoff in a test area. (B) 3DR IRIS+ in flight with 3-axis gimbal on bottom mounted with GoPro4 Black camera/3.6mm low distortion lens.

distortion coefficients that were easier to model during camera pose estimation in SfM processing. In order to optimize image quality, the lens was also manually focused using a computer monitor and then locked to a distance relative to each flight plan's AGH (25 m-35 m AGH). The camera system was then mounted to a Tarot 2D 3-axis self-leveling gimbal attached to the bottom of a 3DRobotics IRIS+, an autonomous electric quadcopter sUAS platform (Fig. 3).

Prior to flight, the camera system was programmed to record one digital still every 0.5 seconds using the camera system software's time lapse feature. All other camera settings such as white balance, f-stop, and ISO speed were left to the camera system software's automatic adjustments to capitalize on the action camera's image stabilization and point-and-shoot capabilities. Detailed flight planning relied primarily on the autonomous design of the 3DR IRIS+ quadcopter which was equipped with an

**Table 4.** Flight plan collection parameters and digital image counts. Items in bold are final flight plans selected for SfM modeling.

Collection Parameters	Flight Plan				
	1	2	3	5	7
Flight Plan Design	<b>E/W Parallel</b>	N/S Parallel	N/S Parallel	<b>E/W Parallel</b>	Orbital
Flight Time (min.)	<b>15</b>	10	7	<b>6</b>	5
*AGH (m)	<b>25</b>	35	35	<b>25</b>	25-50
Flight Speed (m/s)	<b>2</b>	2	4	<b>4</b>	4
Camera Angle (°)	<b>0</b>	0	0	<b>45</b>	45
*GSD (cm <sup>2</sup> /pix)	<b>1.87</b>	3.66	3.66	<b>1.87</b>	1.87-7.46
Unfiltered Images	<b>1,330</b>	923	473	<b>577</b>	664
Filtered Images	<b>1,105</b>	758	303	<b>411</b>	384

\*AGH=Above Ground Height

\*GSD=Ground Sample Distance or the estimated pixel to ground resolution

onboard Ublox NEO-7 series GPS receiver (manufacturer reported dimensional accuracy of 2.5 m) and a Pixhawk autopilot system. The Pixhawk autopilot and Ublox GPS incorporate 3-axis measurements from an onboard gyroscope, accelerometer, and magnetometer that systematically provide external and internal positioning data. This data in turn helps to stabilize the IRIS+ platform through minute adjustments in the four electric propeller-motors and the electric motors of the self-leveling 3-axis gimbal during continuous flight or while stationary against abrupt user-controlled movements or against wind.

3DR Tower3 open-sourced flight planning software was also used prior to flight in order to specify important flight survey parameters such as end/side image overlap, flight speed, and flight line angle or hatch angle. All flight plans either incorporated a 90° (E/W) or 0° (N/S) flight line angle. The software was also used to automatically calculate pixel-to-ground resolutions relative to the GoPro4 Black camera’s image format and the specified AGH. A summary of flight plan collection parameters is provided in

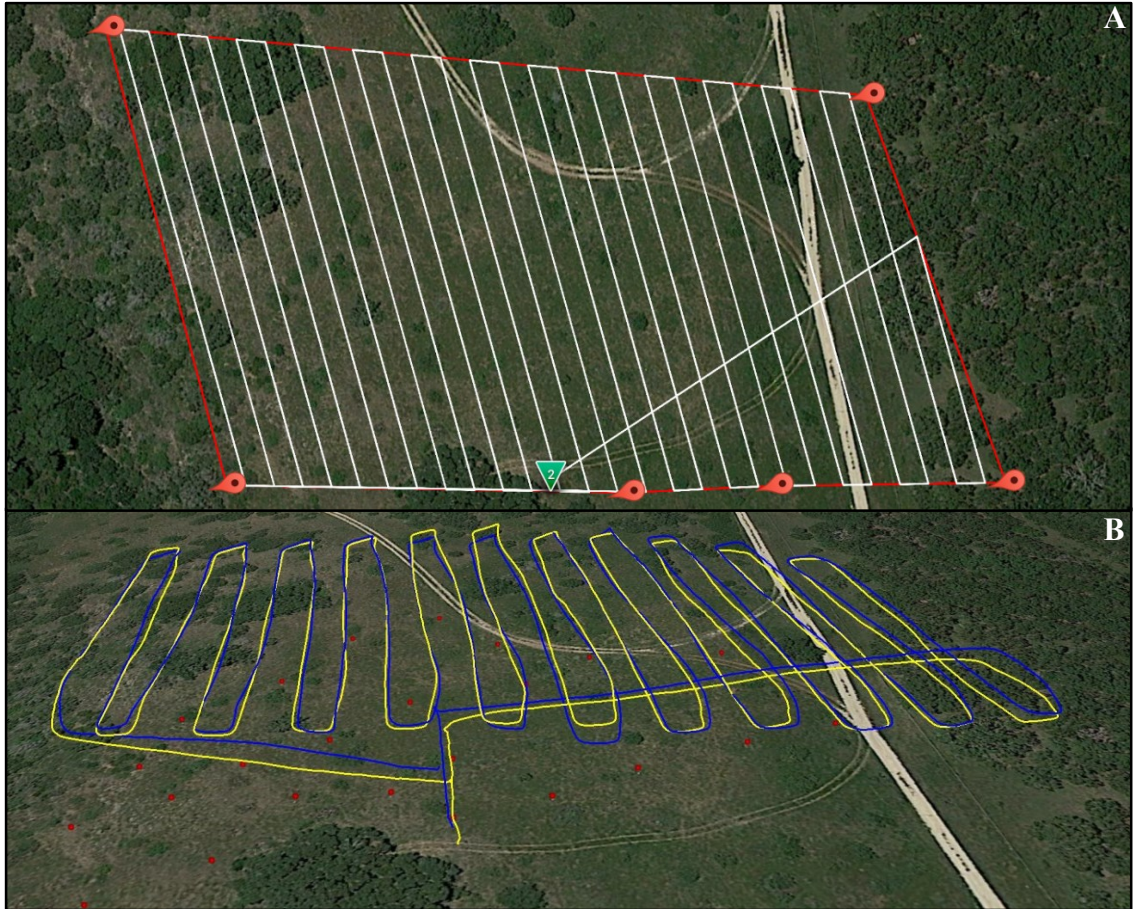


**Figure 4.** Flight plans 1 and 5 screenshots. (A) Screenshot from Tower3 flight planning software showing pre-flight survey lines. (B) Screenshot from Google Earth showing actual autopilot flight log vectors from flight plan 1 (blue line) and flight plan 5 (yellow line) with GCPs (red dots).

Table 4. Pixel-to-ground resolutions below  $4.0 \text{ cm}^2/\text{pixel}$  were specifically targeted based on minimum cladode areas of similar *Opuntia spp.* reported in the literature with minimum cladode areas of approximately  $36.0 \text{ cm}^2$  (Hernández et al. 2010). Using pixel-to-ground-resolutions below a minimum cladode area was predicted to increase the generation of points and during SfM modeling that would represent the minutia of PP cacti structure.

Accordingly, 7 different flight plans were originally used that ranged in flight times from 5-15 minutes with flight speeds of 2 m/s or 4 m/s. Each flight plan was

defined by a manual take-off, an autonomous pre-programmed survey, and an autonomous landing at the take-off location while a ground station tablet that was connected to the sUAS progressively monitored battery life, flight time, GPS signals, and AGH. The primary flight plan design that was incorporated used either a 0° nadir or a 45° low-oblique camera angle that was combined with traditional parallel or survey-style flight lines where the sUAS automatically swept back and forth across the study site either in a north-to-south or east-to-west orientation. An example of east-to-west orientated survey-based flight plans is provided in Fig. 4. In contrast, flight plan 7 incorporated a more complex orbital flight plan with an ascending AGH that spiraled away from the center of the study site and sought to capture a wider variety of camera angles at different heights.

Of the 7 original flight plans, only digital stills from 5 preliminary flight plans (flight plans 1, 2, 3, 5, 7) were further scrutinized as flight plans 4 and 6 were diagnostic test flights. During the image acquisition process, the sUAS platform that was utilized coupled with the specified flight parameters overall allowed multiple surveys of the entire study site within a brief time period. This was anticipated to increase data processing flexibility later based on choices between flight plans which produced the highest quality imagery that best captured target features. Likewise, survey-style flight parameters, autonomy, and sUAS/camera system stability were altogether expected to systematically reduce easily controllable sources of error that pertain to general image quality and image overlap.

## 5.0 DATA PROCESSING

### 5.1 SfM Workflow

Of the 5 flight plans that were used, only images from two final flight plans, flight plan 1 and flight plan 5, were chosen for further processing and analysis. Images from flight plans 1 and 5 were selected because both provided comprehensive coverage of the study site from nadir and low-oblique camera angles, both possessed a manageable number of images to model with respect to data processing efficiency, and both possessed adequate image quality based on even illumination conditions, lack of noise, and the clarity of vegetation features. Flight plan 1 produced 1,330 total images where 225 images were filtered out leaving a final 1,105 images for SfM processing; while flight plan 5 produced 577 total images where 166 were filtered out leaving a final 411 images for SfM processing (Table 4). Most of the images that were filtered consisted of stills acquired near take-off and landing positions where the sUAS was either ascending or descending from survey flight lines. In all, very few of the images taken in any flight plan were of poor image quality or possessed significant image noise associated with blurriness, lens flare, or improper focus. Only slight blurs were found on image edges and were attributed to the movement of the sUAS and the inability to remove all camera lens/sensor distortion. An example of digital stills produced from either flight plan are provided in Fig. 5.

Final images were then input into Agisoft Photoscan v1.2.4, a proprietary SfM software known for its ease of use, relative cost efficiency, and robust modeling procedures. Instead of combining images from both flight plans into a single cache to model from, images from each flight plan were kept separate and imported into different

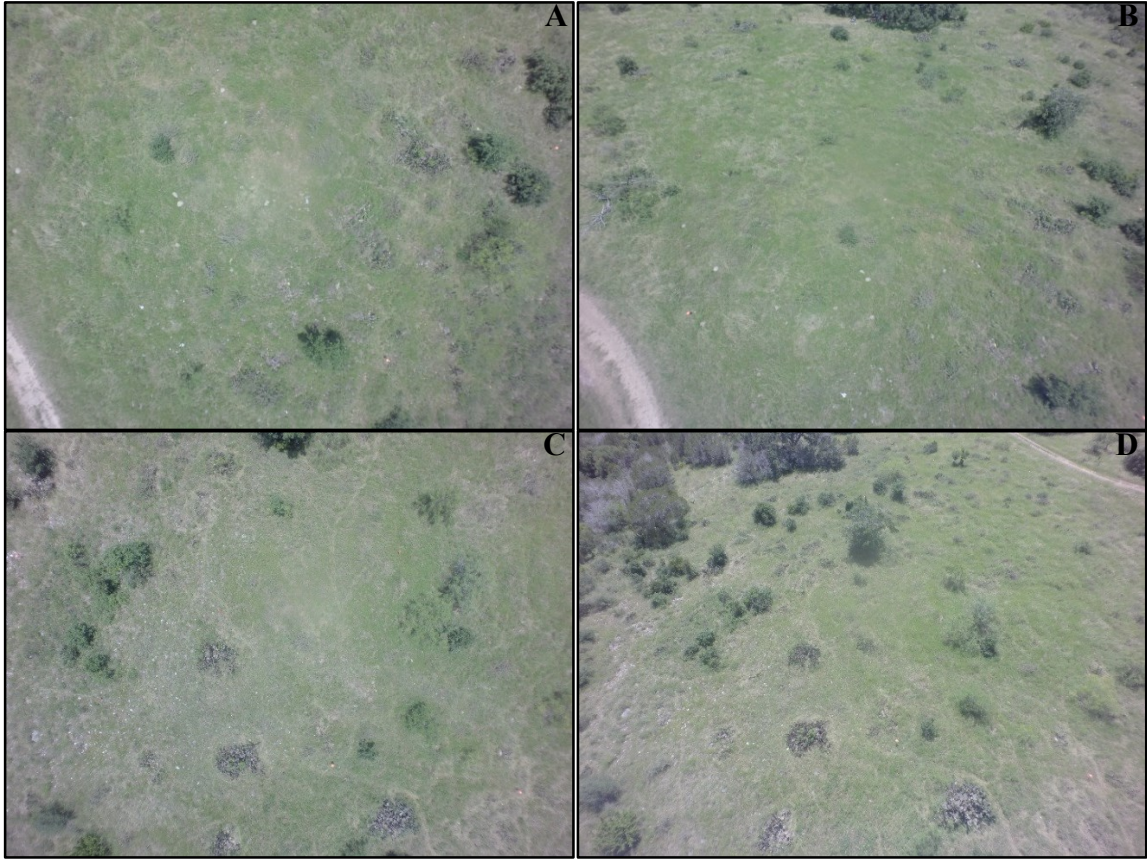


**Figure 5.** Examples of sUAS digital stills. (A)(B) Corresponding stills from flight plan 1 (nadir) and flight plan 5 (low-oblique) of the northwestern section of the study site. (C)(D) Corresponding stills from flight plan 1 (nadir) and flight plan 5 (low-oblique) of the southeastern section of the study site. GCPs can be seen as small orange cones.

SfM modeling pipelines with the goal of merging corrected and geotransformed models later. This strategy was implemented for several reasons. For one, while distortion coefficients from the camera system are the same for each flight plan, camera poses between flight plans and their subsequent keypoint calculations are different. As such, SfM modeling is more efficient when successive images from the same flight plan design follow one another in a steady vector void of major changes in the angle or direction of the camera. In actuality, each image's camera pose estimation should closely follow the actual flight vector of the camera/sUAS position as it surveys back and forth throughout the study site. A single cache with a mix of images from flight plans with  $0^\circ$  and a  $45^\circ$

**Table 5.** Agisoft Photoscan report of GCP GPS positions vs. re-projection errors (n=10).

GCP ID	Projections	$\bar{X}$ of X (m)	$\bar{X}$ of Y (m)	$\bar{X}$ of Z (m)	RSSE XYZ (m)	RMSE (pixel)
1	272	0.024	-0.028	0.024	0.044	3.087
2	308	-0.065	-0.008	-0.033	0.073	2.651
4	114	-0.014	-0.037	0.036	0.053	2.565
14	164	-0.008	-0.008	0.020	0.023	3.246
15	164	-0.088	-0.023	-0.036	0.097	2.074
16	257	0.063	0.037	0.020	0.076	2.077
21	250	0.045	0.016	0.065	0.081	1.862
22	260	-0.016	0.084	0.028	0.090	1.875
23	257	0.024	-0.014	-0.067	0.073	2.365
24	282	-0.012	0.008	-0.024	0.028	1.874
<b>Total RMSE</b>		<b>0.044</b>	<b>0.034</b>	<b>0.039</b>	<b>0.068</b>	<b>2.386</b>

camera angles would thus be initially difficult to model.

Each flight plan’s SfM pipeline used the following common steps: preliminary camera pose estimation (“Align Photos” in Agisoft Photoscan), GCP-based geotransformation, and secondary camera pose estimation (“Optimize Camera Alignment” in Agisoft Photoscan). It should be noted that the preliminary and secondary camera pose estimation steps model and refine previous camera and lens distortion coefficient estimates in order to consistently determine more accurate camera poses, the presence and location of matched image features, and keypoint positions. The secondary camera pose estimation is especially important for correcting errors from the preliminary estimation through the use of GCP-based georeferencing and geotransformation. A preliminary camera pose estimation was thus executed for either flight plan using focal length ( $F_x$ ,  $F_y$ ), principal point ( $C_x$ ,  $C_y$ ), skew, radial distortion ( $K_1$ ,  $K_2$ ,  $K_3$ ,  $K_4$ ), and tangential distortion ( $P_1$ ,  $P_2$ ) coefficients which resulted in a sparse point cloud model that represented keypoints.

After the preliminary camera pose estimation was complete for either flight plan, geotransformation of the sparse point cloud was accomplished within Agisoft Photoscan by digitally marking or flagging individual pixels in each image that corresponded with the 23 GCP centerpoints captured during sUAS image acquisition. This was done in all images that possessed an identifiable GCP centerpoint where most images contained numerous GCP centerpoints. Once each GCP centerpoint was marked, actual GCP coordinates taken from previous GPS measurements were georeferenced to their respective centerpoint ID. The sparse point cloud model for each flight plan was then geotransformed to a real world horizontal coordinate system (Universal Transverse Mercator Zone 14N, XY Datum: NAD83 CORS 96 meters) and vertical datum (NAVD88 meters). Lastly, the secondary camera pose estimation was executed using the same above specified camera and distortion coefficients. The resulting sparse point cloud for flight plan 1 totaled 7,447,116 keypoints (1,105 images) and the sparse point cloud for flight plan 5 totaled 1,135,042 keypoints (411 images). After restricting both flight plan models to a common spatial boundary or bounding box, the models were then aligned with one another using their shared GCP coordinates and then merged.

While the merged model initially used all 23 GCP centerpoints, it was found that dimensional accuracies could be improved by filtering GCP centerpoints that possessed higher re-projection errors and removing images where GCP centerpoints were less clearly identifiable. The use of numerous GCPs for the approximately 1 ha study site combined with a high degree (90%) of image overlap allowed flexibility in refining and optimizing the dimensional accuracy of the merges model without detriment to the quality of the model or loss of point density. Of the 23 original GCPs, 14 were removed

which left 10 final GCPs still evenly distributed throughout the study site. A final camera pose estimation was then executed on the merged sparse point cloud using the same specified camera and lens coefficients. Finally, the model was spatially clipped to remove keypoints outside of the general study area and extraneous keypoints that represented minor noise where very few keypoints were exceedingly above or below the study site's elevations. A workflow diagram of SfM processing steps is provided in Appendix A. The final sparse point cloud model consisted of 7,602,076 total keypoints. The dimensional accuracy report generated by Agisoft Photoscan for all models reported a total RMSE of 0.068 m or 2.386 pixels between actual vs. re-projected GPS positions. A summary of the dimensional accuracy reported by Agisoft for GCP GPS vs. estimated re-projection errors is provided Table 5.

## **5.2 Generation of Dense Point Cloud**

In order to output a point cloud that possessed adequate point density and was predicted to capture the detailed vegetation structures of each PP cacti plot, three different point clouds were generated within Agisoft Photoscan and later combined. A combination strategy was adopted because like most SfM software, Agisoft Photoscan utilizes a MVS-based densification process with user-defined settings that can alter depth filtering rate or aggression and can be tailored to reconstruct different aspects of a target's features, i.e. regions or features with more detail than others. In general, the densification process utilizes algorithms that combine the 3-D positions of the predetermined keypoints with depth mapping or Z-buffering algorithms designed to fill in or interpolate additional points in areas that surround or are between known keypoints using camera pose data (i.e.

**Table 6.** Summary of dense point cloud properties. Items in bold correspond to the combined dense point cloud that was used for analysis.

Properties		Point Cloud Type			
		mild	moderate	aggressive	<b>combined</b>
<b>Spatial</b>	Elevation Min. (m)	219.49	219.74	224.64	<b>219.43</b>
	Elevation Max. (m)	239.15	239.08	239.22	<b>239.05</b>
	Total Point-Count	2,431,355	2,210,735	2,351,728	<b>8,261,367</b>
	$\bar{X}$ Point-Density (pts/m <sup>2</sup> )	256.91	233.69	248.70	<b>505.34</b>
	$\bar{X}$ Point-Spacing (m)	0.061	0.064	0.062	<b>0.043</b>
<b>Spectral*</b>	R Min.	514	1,285	1,285	<b>514</b>
	R Max.	65,535	65,278	65,535	<b>65,535</b>
	G Min.	1,542	2,056	3,084	<b>1,542</b>
	G Max.	64,250	65,278	64,250	<b>65,278</b>
	B Min.	1,542	1,028	257	<b>257</b>
	B Max.	65,535	65,535	65,535	<b>65,535</b>

\*Unsigned 16-bit

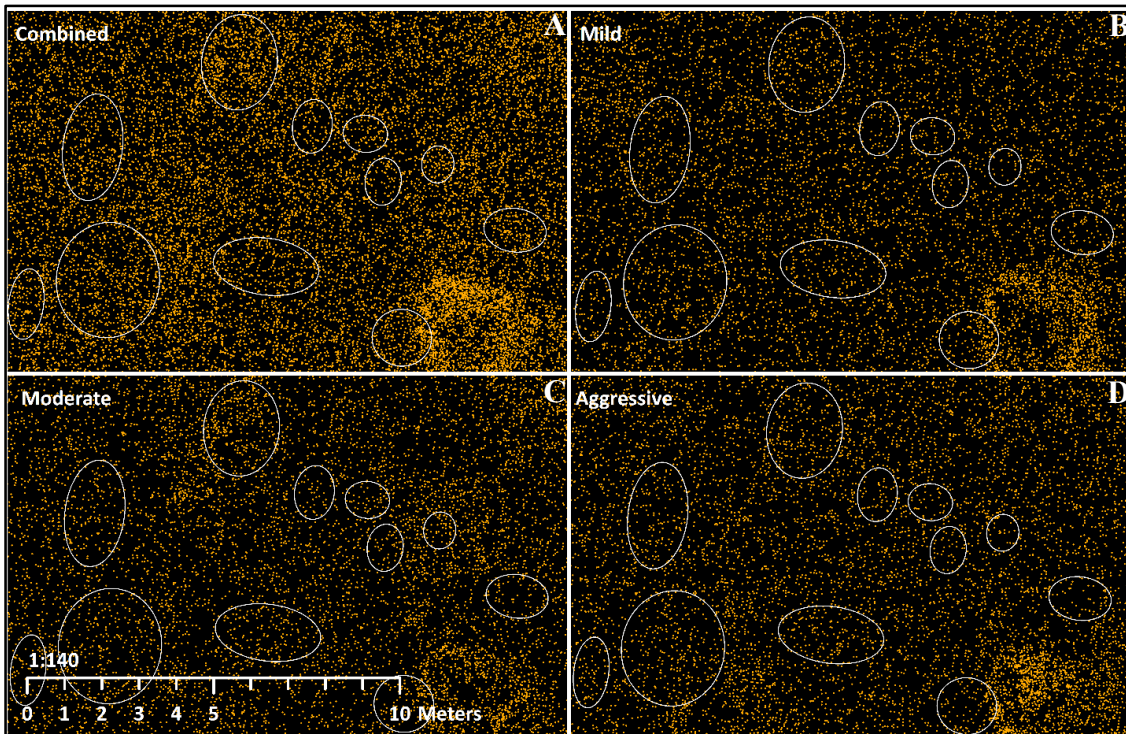


**Figure 6.** Examples of generated dense point cloud types. (A)(B)(C)(D) show combined, mild, moderate, and aggressive depth filter densification settings, respectively. PP cacti plot-ellipses can be seen as white ellipses.

focal plane, Z-axis, orientation, etc.) and pixel bit-depth. With regards to the literature, it is unknown which settings are optimal for complex natural environments; though it is understood that each depth filtering setting can capture varying degrees of foreground and background details depending on scene and image characteristics.

Therefore, in order to increase data processing efficiency for a rather computationally demanding step while preserving scene quality, three different dense point cloud “types” were generated in Agisoft Photoscan based on the “mild”, “moderate”, and “aggressive” depth filtering settings for the “low” quality. Fig. 6 demonstrates the differences that can be seen between each dense point cloud type with respect to known PP cacti plots. The three different point cloud types were then merged into a final dense point cloud within Agisoft Photoscan that possessed combined spatial (point count, point density, point spacing) and spectral properties predicted to satisfy the study’s objectives (Table 6). Using the combined dense point cloud, a point sum (total point count/0.20 m<sup>2</sup>) raster (Fig. 9), a point Z-range (maximum point elevation-minimum point elevation/0.20 m<sup>2</sup>) raster (Fig. 10), and a detailed maximum point-Z TIN (Fig. 11) of the study site were generated (see Results, section 7.1).

### **5.3 Generation of RGB Orthophoto**

A VHR RGB orthophoto of the study site was also constructed in Agisoft Photoscan where a 3-D mesh (4,775,161 faces/ 2,388,896 vertices) or TIN was first calculated from maximum point-Z values derived from the dense point cloud. Though a relatively straightforward step, the construction of a dimensionally accurate 3-D mesh was important because it helped correct any irregular projection geometries that may have been produced from sUAS-acquired aerial photo projection. An accurate mesh was

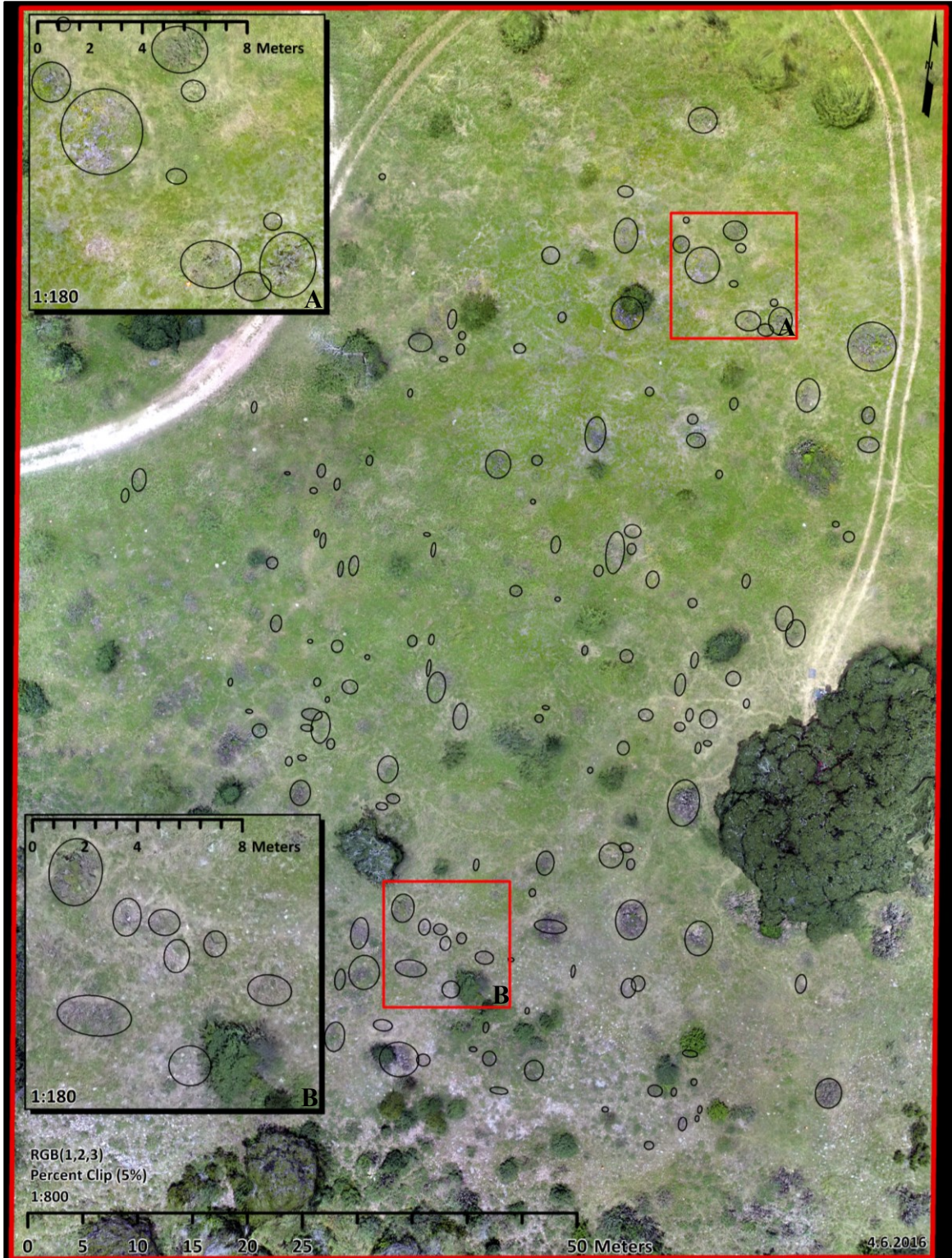


**Figure 7.** RGB orthophoto of BC study site. (A) top (northeast) inset and (B) bottom (southwest) inset. Plot-ellipses are shown as black ellipses.

also needed for correct dimensional placement of spectral values from the sUAS-acquired aerial photos onto surfaces or structures that corresponded to PP cacti and surrounding vegetation/non-vegetation land cover classes. Reliable spectral values for either class would then be used to generate accurate OBIA segments which represent real-world vegetation boundaries.

RGB values for the orthophoto were calculated using a mosaic blending algorithm that determined a particular orthophoto's pixel value by calculating which specific 2D image possessed a pixel that was closest to the center of the camera ( $P_x$ ,  $P_y$ ). Specifically, the RGB values of the pixel that was most directly beneath the camera during image acquisition was assigned as the RGB value of the orthophoto's pixel. While this study does not provide a detailed comparison of orthophoto blending algorithms (averaging, maximum, minimum, etc.), this setting was predicted to provide a more realistic determination of spectral values as they are derived from pixel's whose locations are near perpendicular to the principal point of the camera where major variations in spectral values or distortion is less likely. The resulting 16-bit RGB orthophoto was exported to a minimum resolution of 2.25 cm<sup>2</sup>/pixel (6497 x 8,288/ 410.82 MB) based on the minimum pixel-to-ground resolution of digital stills (0.0187 cm<sup>2</sup>/pixel). The RGB orthophoto of the study site is provided in Fig. 7 along with plot-ellipse polygons.

#### **5.4 OBIA Segmentation and Random Forest Classification**

Using the RGB orthophoto, a Principle Components raster ( $PCA_1$ ,  $PCA_2$ ,  $PCA_3$ ) and an IHS raster were generated in ENVI v5.2 where they were input into the ENVI V5.2 FX feature extraction module, an OBIA-based workflow that calculates OBIA segments and segment attributes based on user-defined parent and ancillary datasets. By first using only the RGB orthophoto, numerous individual segments were calculated using a combination of FLS (Full Lambda Schedule) and Edge segmentation algorithms. Specific FLS and Edge settings were optimized for the detection of subtle vegetation cover boundaries between PP cacti and non-PP cacti vegetated or non-vegetated land cover (e.g. rocks, bare-earth, ground litter, etc.) while considering the maximum number of segments achievable defined by the total number of RGB orthophoto pixels (53,847,136), its spatial resolution (2.25 m<sup>2</sup>/pixel), and its extremely high spatial frequency.

In order to refine segmentation boundaries, plot-ellipse polygons (known PP cacti ECC) and expert knowledge of study site vegetated/non-vegetated land cover was used to reference segment boundaries with actual boundaries. Overall, optimal representation of PP cacti and non-PP cacti land covers was achieved using a balance of segment scale/geometry, individual segment area, total number of segments per land cover class, and general segment representation of foliar cover boundaries. Optimum OBIA segmentation then resulted in a total of 389,007 individual segments. An overlay of final OBIA segments atop the RGB orthophoto can be seen in Fig. 8.

Within each segment, 86 total attributes were then calculated using the three RGB bands of the orthophoto, three ancillary PC bands ( $PC_1$ ,  $PC_2$ ,  $PC_3$ ), and three ancillary



**Figure 8.** OBIA segments and RGB orthophoto. (A) top (northeast) inset and (B) bottom (southwest) inset. Differences in segment shape and size per land cover feature can be seen. Plot-ellipses are shown as white ellipses.

IHS bands. The 86 total attributes consisted of 14 different spatial attributes (area, length, compactness, convexity, solidity, roundness, form factor, elongation, rectangular fit, main direction, major length, minor length, number of holes, hole area: solid area) 4 statistical attributes calculated per band (mean, minimum, maximum, SD) and 4 textural attributes calculated per band (range, mean, variance, entropy). The unclassified OBIA segments were then exported as a tabular dataset.

Prior to OBIA segment classification, unclassified segments had to be divided into training and testing datasets that adequately represented both PP cacti (PP=2) and non-PP cacti (non-PP=1) land cover classes. Using a plot-ellipse dataset that consisted of 160 observations, where 4 observations were removed due to close proximity to the outer edges of the study site, a PP-class training and testing dataset was generated using a stratified random sample selection based on cladode count (CLAD<sub>COUNT</sub>) where one-half of the plot-ellipses were subset for training (n = 80) and the other-half were subset for testing (n = 80). The CLAD<sub>COUNT</sub> field metric was used because it possessed the highest coefficient-of-determination ( $R^2$ ) values when compared to PP<sub>HEIGHT</sub>, ECC, ECV, and ECSA field metrics. This made it a logical field metric to use for randomized sampling designed to divide the dataset based on the best representative of the general structure and size of each PP cacti plot. PP-class training and PP-class testing plot-ellipses were then used to manually select segments within each plot-ellipse which resulted in 918 PP-class training segments and 1,137 PP-class testing segments.

In contrast, the non-PP-class training and testing datasets were generated by first selecting all segments outside of the plot-ellipses, and then randomly sub-setting 5% to a testing dataset and 5% to a training dataset. These segment subsets were then manually

filtered to remove any possible segments that might correspond to PP cacti vegetated cover using expert knowledge of the study site and visual references to known PP cacti locations (plot-ellipses). It should be noted that for a reliable classification methodology that utilizes only two thematic classes (PP and non-PP), segments had to be carefully selected to represent a variety of non-PP land cover which included vegetated (trees, shrubs, grasses, etc.) and non-vegetated (gravel roads, rocks, bare-earth, etc.). The final non-PP-class segment dataset consisted of 16,773 training segments and 16,921 testing segments. The final training dataset consisted of 17,691 total segments (PP-class=918 segments/non-PP-class=16,773 segments) while the final testing dataset consisted of 18,058 total segments (PP-class=1,137 segments, non-PP-class=16,921)

Following similar studies like Laliberte and Rango (2008) and Browning, Laliberte, and Rango (2011) that have demonstrated the need for feature/attribute selection methods, the 86 original segment attributes calculated in ENVI FX were filtered using an attribute selector or a weighted attribute filtering algorithm. While attribute selection isn't always necessary prior to machine learning-based classification, it is a best use practice for large datasets and was predicted to improve final Random Forest (RF) classification accuracy through the removal of redundant or collinear attributes that did not contribute to overall classification accuracy.

Attribute selection was accomplished using RapidMiner Studio v6.5 where the previously generated training dataset was used to train a preliminary 100 tree RF model using a "Weight by Tree Importance" attribute selection module. This module then weighted attributes by calculating the sum contribution of each attribute in the 100 decision trees towards the overall accuracy of the trained RF model (RapidMiner 2016).

This resulted in a rated list of all 86 attributes where the bottom 20 attributes were filtered and the top 66 attributes which best contributed to the overall accuracy of the preliminary trained RF model were selected for primary RF classification. A table of the 66 segment attributes and mean values is provided in Appendix B.

Classification of OBIA segments was accomplished using Weka v3.7.13, an open-sourced and free statistical analysis and data mining software known for its relative computational efficiency for large datasets. Altogether, classification underwent a three-phase process that involved RF model training, testing, and pixel-based validation. While an K-fold cross validation strategy was implemented for RF model training, a separate testing and map-based validation was deemed necessary based on the large number of total segments available and the division of a complex dataset into a binary classification.

In the first phase, the training dataset was used to train a 300 tree RF model using a K-fold (k=8) cross-validation strategy. After each training phase, the model was then tested using the separate testing dataset where both training and testing classification accuracy measures were compared and evaluated. The specific accuracy measures used to evaluate and compare each potential model included the percent of correct/incorrect classification instances, Kappa statistic, true-positive (TP) rate, false-positive(FP) rate, F-measure, and Receiver Operating Curve (ROC) area. Various iterations of the training and testing phases were implemented to refine final RF classification model accuracy measures based on optimal settings of cross validation folds and the number of trees to model. The most optimal RF classification model was then used to predict PP or non-PP classes for the unclassified segments tabular dataset

The predicted class of each segment was then joined to an unclassified OBIA segments shapefile that was generated in ENVI FX. The resulting classified segments shapefile was then converted into a raster format, or a thematic land cover map of the study site with PP and non-PP thematic classes (see Results, section 7.2, Fig. 15). The final map-based validation phase then assessed the accuracy of the classification map in ENVI v5.2 by using the already randomized locations of PP-class and non-PP-class segments derived from the testing dataset. It should be noted that an overall classification accuracy of at least 85% and a PP cacti plot detection rate of 50% was necessary to satisfy statistical analysis objectives. A workflow diagram of OBIA segmentation and classification steps is provided in Appendix A.

## **5.5 Calculation of Predictor Variables**

Prior to data analysis, PP-class segments from the classified segments shapefile were separated from non-PP-class segments. Individual PP-class segments were then dissolved into a single PP-class polygon that was spatially intersected with individual plot-ellipses in order to create distinct plot-segment polygons with adjoining field metric variables. Each plot-segment polygon thus represented the sum total area of all OBIA segments within a plot-ellipse polygon that were classified as PP cacti vegetated land cover. The calculation of OBIA plot-segment dimensions in comparison to field measured plot-ellipse dimensions therefore allowed the direct comparison of predictive regression models of PP cacti structure generated from either polygon geometry's PH-derived predictor variables. More specifically, this allowed a relative evaluation of traditional rangeland Lidar research-based techniques that have used field measured

elliptical plot dimensions (plot-ellipses) to extract PHs and subsequent predictor variables (statistical, TIN-derived, etc.) in comparison to VHR OBIA techniques (post segmentation + classification) that use non-field measured OBIA segment-derived plot dimensions (plot-segments) to extract PHs and subsequent predictor variables.

### **5.51 TIN-derived Volume and Surface Area Predictors**

Instead of Agisoft Photoscan, ArcMap v10.2 was used to generate a more detailed DSM that was used for the calculation of volume and surface area predictor variables for each PP cacti plot-ellipse and plot-segment polygon. Similar to the creation of the 3-D mesh in Agisoft Photoscan, the DSM surface was generated using a TIN interpolation of the maximum Z-values of each point without thinning. This resulted in TIN model of the study site that consisted of 8,862,455 faces and 4,431,240 vertices.

Using the detailed TIN surface, TIN-derived volume for each plot-ellipse (PLOT-TIN<sub>VOL</sub>) and plot-segment polygon (SEG-TIN<sub>VOL</sub>) was first determined by assigning plot centerpoint elevations, acquired during field GPS measurements, as base elevations and then calculating polygon volume (m<sup>3</sup>) as the space above the base elevation and below TIN surface elevations. The TIN-derived 3-D surface area for each plot-ellipse (PLOT-TIN<sub>SA</sub>) and plot-segment (SEG-TIN<sub>SA</sub>) polygon was simply calculated as the sum total 2-D area of all TIN faces within each polygon.

### 5.52 Point Height-derived Statistical Predictors

In order to calculate sUAS-SfM PH-derived predictors for plot-ellipse and plot-segment predictive regression models, individual points from the combined dense point cloud were extracted using plot-ellipse and plot-segment polygon area dimensions. Extracted points were then spatially-joined to the parent plot-ellipse or plot-segment polygon that completely contained their XY coordinates resulting in a total of 257,630 individual points extracted from plot-ellipse polygons and a total of 66,920 individual points extracted from plot-segment polygons. The actual *point height*, or the orthographic height of each point, was then calculated by subtracting the plot centerpoint GPS-measured elevation (bare-earth Z) from the point elevation (point-Z).

All plot-ellipse and plot-segment PHs were then sorted by the unique field plot ID of the containing polygon and then exported to a tabular dataset in order to calculate a total of 52 total statistical predictors. Specifically, this included 7 descriptive variables (e.g. total point count, mean, minimum, maximum, variance, coefficient of variance), 11 percent of PHs variables in ranges of 0.10 m ( $x < 0.05$  m,  $0.05 \leq x < 0.15$ ,  $0.15 \leq x < 0.25$  m...,  $x \geq 0.95$  m), 19 percentile variables (10<sup>th</sup>, 15<sup>th</sup>, 20<sup>th</sup>, ..., 100<sup>th</sup>), and 15 difference of percentiles variables (90<sup>th</sup> – 80<sup>th</sup>, 90<sup>th</sup> – 70<sup>th</sup>, 90<sup>th</sup> – 60<sup>th</sup>, ..., 90<sup>th</sup> – 20<sup>th</sup> and 100<sup>th</sup> – 90<sup>th</sup>, 100<sup>th</sup> – 80<sup>th</sup>, 100<sup>th</sup> – 70<sup>th</sup>, ... 100 - 20<sup>th</sup>). Two additional predictor variables were calculated from the plot-segment generation process which included the total number of original undissolved segments used to form plot-segment polygon (SEG<sub>COUNT</sub>) and the total 2D area of the dissolved plot-segment polygon (SEG<sub>AREA</sub>).

A total of 44 predictors were calculated for 157 plot-ellipse observations. Only two plot-segment observations were filtered due to negative PHs resulting in 106 plot-

segment observations. Predictors and their corresponding field metrics for plot-ellipse and plot-segment observations were then exported as two separate tabular datasets for further statistical analysis.

## **6.0 DATA ANALYSIS**

Plot-ellipse and plot-segment datasets were then imported into SAS JMP Pro v12 statistical analysis and data mining software in order to generate and evaluate robust predictive regression models of each field metric using a three-phase analysis process. In the first phase, a preliminary statistical analysis was performed that examined field metric distribution characteristics and significant predictor variable relationships. Following assumptions of normality, predictor independence, and homoscedasticity, a primary statistical analysis phase then incorporated K-fold CV training of multiple linear regression models. In this phase individual predictors and potential models were generally evaluated based on relative statistical measures of goodness of fit and goodness of prediction in comparison to competing models which resulted in a pool of candidate models. Final model selection then also evaluated the remaining candidate models based on statistical measures of model goodness of fit, goodness of prediction, and error in addition to measures of individual predictor explanation of variance and predictor multicollinearity.

### **6.1 Preliminary Statistical Analysis**

The preliminary analysis first implemented an examination of each field metric's distribution characteristics that was designed to identify potential outlier observations between field metrics and to determine relative distribution design. While an assumption of normality was inherently adopted for this study's analysis, based on the geographic and biological nature of the study's sample as a representative of a larger population of plant species; a visual examination of field metric distributions nonetheless allowed for a

reliable interpretation of predictive linear regression model errors later as many field metrics in fact possessed near logistic or log-linear distributions.

Once potential outliers were identified within distribution plots, 1:1 linear regression fits between dependent and predictor variables were used to further test outlier model fitness and test-error effects. In all only two outlier observations were removed for both plot-ellipse and plot-segment datasets. These outliers represented the two largest PP cacti plots encountered within the study site with cladode counts greater than 450. Final observations for plot-ellipse (n=155) and plot-segment (n=104) datasets were then again examined using 1:1 linear regression fits between dependent and predictor variables.

Individual predictor correlation strength ( $r$ ) and goodness of fit ( $R^2$ , RMSE) values were used to determine weak predictors or predictors that would not significantly contribute to predictive explanation of variance for all field metrics. Of the original 52 predictors, only 8 variables were removed which included 6 percent of PHs (POH) variables ( $x < 0.05$  m,  $0.05 \leq x < 0.15$ ,  $0.15 \leq x < 0.25$  m...,  $0.45 \leq x < 0.55$  m), PH covariance ( $PPHEIGHT_{CV}$ ), and the 10<sup>th</sup> percentile ( $PH10_{PCTL}$ ) which left a final 44 predictors. A summary of plot-ellipse and plot-segment  $R^2$  values for several descriptive and TIN-derived variables are provided in Table 7-9.

**Table 7.** 1:1 plot-ellipse  $R^2$  values: field metrics vs. descriptive predictors. Items in bold represent  $R^2$  values  $\geq 0.40$ .

Dependent (Y)		Predictor (X)				
		PH <sub>MEAN</sub>	PH <sub>MAX</sub>	PH <sub>SD</sub>	PH <sub>VAR</sub>	PH <sub>COUNT</sub>
Plot-ellipse (n=155)	CLAD <sub>COUNT</sub>	0.290	0.382	0.336	0.093	<b>0.738</b>
	PP <sub>HEIGHT</sub> (m)	<b>0.405</b>	<b>0.438</b>	0.396	0.121	0.361
	ECC (m <sup>2</sup> )	0.207	0.284	0.275	0.079	<b>0.717</b>
	ECV (m <sup>3</sup> )	0.278	<b>0.402</b>	0.359	0.117	<b>0.781</b>
	ECSA (m <sup>2</sup> )	0.360	<b>0.508</b>	<b>0.473</b>	0.166	<b>0.634</b>
	FWB (Kg)	0.290	0.382	0.336	0.093	<b>0.738</b>
	DWB (Kg)	0.246	0.322	0.326	0.094	<b>0.798</b>
Plot-segment (n=104)	CLAD <sub>COUNT</sub>	0.259	0.291	0.294	0.166	<b>0.818</b>
	PP <sub>HEIGHT</sub> (m)	0.359	0.320	0.270	0.130	<b>0.448</b>
	ECC (m <sup>2</sup> )	0.175	0.225	0.227	0.105	<b>0.886</b>
	ECV (m <sup>3</sup> )	0.255	0.318	0.328	0.189	<b>0.894</b>
	ECSA (m <sup>2</sup> )	0.343	0.397	0.387	0.213	<b>0.776</b>
	FWB (Kg)	0.259	0.291	0.294	0.166	<b>0.818</b>
	DWB (Kg)	0.192	0.234	0.234	0.103	<b>0.841</b>

**Table 8.** 1:1 plot-ellipse  $R^2$  values: field metrics vs. TIN-derived predictors. Items in bold represent  $R^2$  values  $\geq 0.40$ .

Dependent (Y)	Predictor (X)	
	PLOT-TIN <sub>VOL</sub> (m <sup>3</sup> )	PLOT-TIN <sub>SA</sub> (m <sup>2</sup> )
CLAD <sub>COUNT</sub>	<b>0.646</b>	<b>0.635</b>
PP <sub>HEIGHT</sub> (m)	0.327	0.377
ECC (m <sup>2</sup> )	<b>0.664</b>	<b>0.635</b>
ECV (m <sup>3</sup> )	<b>0.685</b>	<b>0.726</b>
ECSA (m <sup>2</sup> )	<b>0.583</b>	<b>0.673</b>
FWB (Kg)	<b>0.646</b>	<b>0.635</b>
DWB (Kg)	<b>0.592</b>	<b>0.636</b>

**Table 9.** 1:1 plot-segment  $R^2$  values: field metrics vs. segment/TIN-derived predictors. Items in bold represent  $R^2$  values  $\geq 0.40$ .

Dependent (Y)	Predictor (X)			
	SEG <sub>COUNT</sub>	SEG <sub>AREA</sub> (m <sup>2</sup> )	SEG-TIN <sub>VOL</sub> (m <sup>3</sup> )	SEG-TIN <sub>SA</sub> (m <sup>2</sup> )
CLAD <sub>COUNT</sub>	<b>0.634</b>	<b>0.735</b>	<b>0.695</b>	<b>0.671</b>
PP <sub>HEIGHT</sub> (m)	0.221	0.290	0.289	0.388
ECC (m <sup>2</sup> )	<b>0.698</b>	<b>0.795</b>	<b>0.729</b>	<b>0.556</b>
ECV (m <sup>3</sup> )	<b>0.666</b>	<b>0.745</b>	<b>0.719</b>	<b>0.697</b>
ECSA (m <sup>2</sup> )	<b>0.460</b>	<b>0.576</b>	<b>0.542</b>	<b>0.643</b>
FWB (Kg)	<b>0.634</b>	<b>0.735</b>	<b>0.695</b>	<b>0.671</b>
DWB (Kg)	<b>0.659</b>	<b>0.777</b>	<b>0.732</b>	<b>0.712</b>

## 6.2 MLR Model Training and General Evaluation

While a 2/3 test-set method was initially implemented for regression model training based on a stratified random selection derived from CLAD<sub>COUNT</sub>, many 2 and 3 term training and validation models were found to possess inconsistent or poor model fitness and predictive capability statistical measures. In addition, relatively high bias and low variance or model “underfitting” was seen in residual plots with respect to the low number of terms used. This was found to reoccur with additional randomized test sets based on ECC or ECV field metrics which share high  $R^2$  values with CLAD<sub>COUNT</sub>. Based on the preliminary analysis of field metric distributions, this was best explained by the inability of an insufficiently trained linear regression model to fully capture the near-logistic (sigmoidal) growth patterns of the study site’s heterogeneous PP cacti population which possessed three basic ranges of plot “size”, as evidenced by several field metrics (e.g. CLAD<sub>COUNT</sub>, PP<sub>HEIGHT</sub>, and ECV) where most plots were possessed field metric values below mean values (see Results, section 7.2, Fig. 16; see Discussion, section 8.2, Fig. 18).

In order to help reduce any sampling bias, improve model generalization, and maintain the study's need for interpretable multiple linear regression models with few predictors, a K-fold CV strategy was adopted. Specifically, a conservative 3-fold ( $k = 3$ ) sampling approach was adopted over higher folds ( $k=5$ ,  $k=10$ ) based on the total sample size available, the need to represent a three-part logistic growth of PP cacti plots, and the need to lower estimation variance for both plot-ellipse ( $n=155$ ) and plot-segment ( $n=104$ ) datasets.

MLR modeling in SAS JMP v12 employed the stepwise regression module which was first used to train K-fold CV models for each field metric using the forward-step option. Individual models generated from this option were automatically rated, regardless of the number of terms, by the maximum K-fold CV  $R^2$  stopping rule or the average validation  $R^2$  for all 3-folds. Stepwise K-fold CV models were then compared to additional models produced from the "all possible models" option which automatically rated models by maximum  $R^2$  values (actual vs. predicted) ordered by the number of terms. Using these dialogs options, only 2 and 3 term regression models were generated and evaluated based on the need to balance interpretability of individual predictors with overall model goodness of fit and predictive power, all while reducing potential multicollinearity.

General model evaluation for each dependent variable underwent a progressive refinement that first explored stepwise predictor interactions using the forward-step history. Poor or statistically insignificant predictors were generally removed altogether which left a progressively smaller number of meaningful predictor combinations and potential models. These models were then re-evaluated and rated using the K-fold CV

maximum  $R^2$  value as the primary estimate for a model's predictive power and the  $R^2$  (actual vs. predicted) value as the primary estimate for goodness of fit. In addition, low RMSE, Mallow's  $C_p$ , and AICc values were compared between competing models (2-term and 3-term) as the primary means of assessing model test-error, low bias ( $C_p$  close to  $p$ ), and a high probability of predictive precision. It should be noted that 2-term models were always preferred over 3-term models when statistical measures between-models were compared and found to be close, generally within 1-4 percent of difference of variance explanation. Once general model evaluation was accomplished, the best 10 models for each 2-term and 3-term model, or the top 20 models per field metric, were chosen as candidate models.

### **6.3 Final MLR Model Selection**

Similar to general model evaluation, candidate models were first compared based on statistical measures of model fitness, predictive power, and test error. While low AICc and  $C_p$  values between models with the same number of terms were compared, models that showed little difference between K-fold CV maximum  $R^2$  values and actual vs. predicted  $R^2$  values were preferred. K-fold CV maximum  $R^2$  and PRESS (Predicted Residual Sum of Squares) values were also compared between competing models where generally models with lower values and thus better predictive capability were preferred. Similarly,  $PRESS_{RMSE}$  values were compared to actual vs. predicted RMSE values within-models and between-models to address any issues of over-fitting or under-fitting. Following this initial step, approximately 3-5 candidate models for each dependent variable were left for further scrutiny.

Final candidate models were then assessed based on statistical measures of predictor multicollinearity in addition to visual examinations of homoscedasticity. To address multicollinearity, a correlation coefficient (R) matrix for each model's predictors was first calculated, favoring models whose predictors shared extremely weak correlations ( $-0.20 > R < 0.20$ ) thereby possibly reducing any data redundancy or overlap of explained variance. Similarly, individual predictor tolerance ( $1 - R_j^2$ ) and VIF (Variance Inflation Factor;  $1/\text{tolerance}$ ) values were also calculated to determine the degree of explained shared variance and the magnitude of inflation not seen in the correlation matrix. Considering the low number of terms in each model, models with predictors that possessed relatively high VIF values ( $\text{VIF} > 5.0$ ) and low tolerance values ( $\text{tolerance} < 0.10$ ) were interpreted as models with a high degree of unexplained variance between predictors and thus possessing significant multicollinearity.

Therefore, models with predictors that possessed high tolerance values closer to 1.0 and low VIF values closer to 1.0 were considered to lack any significant multicollinearity and were chosen over models with evidence of multicollinearity. Notably, tolerance and VIF values were not always absolute indicators of predictor or model insignificance and values were interpreted holistically with regards to the nature of PH-derived statistical variables as products of a single dataset. The final step then assessed any major violations in a final model's assumption of homoscedasticity by visually examining residual plots for equal variance. Models that demonstrated strong homoscedasticity and lack of bias were favored. All final multiple linear regression models and model predictors are reported to be statistically significant ( $\alpha = 0.05$ ,  $p < 0.0001$ ). A workflow diagram of statistical analysis steps is provided in Appendix A.

Overall, the final MLR models selected for each field metric were based on various measures of goodness of fit and predictive capability that used a hierarchical evaluation strategy with between-model and within-model statistical assessments. This was done in order to produce a well-rounded low-term prediction model with a reduction in any test-error, bias-error, variance-error, and data redundancy. Regarding software capabilities and limitations, it should be noted that during model selection the “stepwise” option was utilized as a functional guide to exploring successive predictor combinations and calculating optimal K-fold CV models while the “all possible models” option was used to further compare possible models and then further scrutinize within-model statistical measures. Moreover, it is only possible in SAS JMP 12 to calculate K-fold CV maximum  $R^2$  values using stepwise regression first, which introduces each predictor step-by-step and then calculates its contribution to model fit as K-fold CV maximum  $R^2$  values are not automatically calculated in the “all possible models” option alone.

## **7.0 RESULTS AND DISCUSSION**

### **7.1 Visual Characteristics of sUAS-SfM 3-D Datasets**

In addition to the dense point cloud, dense point cloud-derived visualizations were generated in order to examine important point characteristics. A visual analysis was also predicted to help elucidate results from RF-classification, PP cacti plot detection, and predictive MLR modeling. Specifically, visual analysis results sought to report point distribution and point elevation patterns that visually differentiated or were shared among PP cacti plots in comparison to their respective field metrics and the point distribution and elevation patterns of surrounding land covers. Examples of generated visualizations can be seen in the combined dense point cloud or dense point cloud (Fig. 9), point sum raster (Fig. 10), maximum point-Z TIN (Fig. 11), and point Z-range raster (Fig. 12).

#### **7.11 Point Distribution and Elevation Results**

Fig. 9 and Fig. 10 show overhead 2-D perspectives of the study site's dense point cloud and point sum raster (total point count/0.01 m<sup>2</sup>) where either visualization demonstrate several distinct point distribution patterns readily observable for different small to large plot-ellipses or PP cacti plots with varying ECC values, vegetated/non-vegetated land covers, and features that correspond to individual or clustered trees and shrubs. Although flight plan settings (Table 3) were designed to yield relatively equal side/end overlap, the dense point cloud is non-uniform and exhibits the characteristic non-uniformity reported by other studies that have produced VHR sUAS-SfM-derived point clouds. The dense point cloud nonetheless demonstrates few discernable visual data gaps caused by major LoS issues for the primary analysis area, or the area that

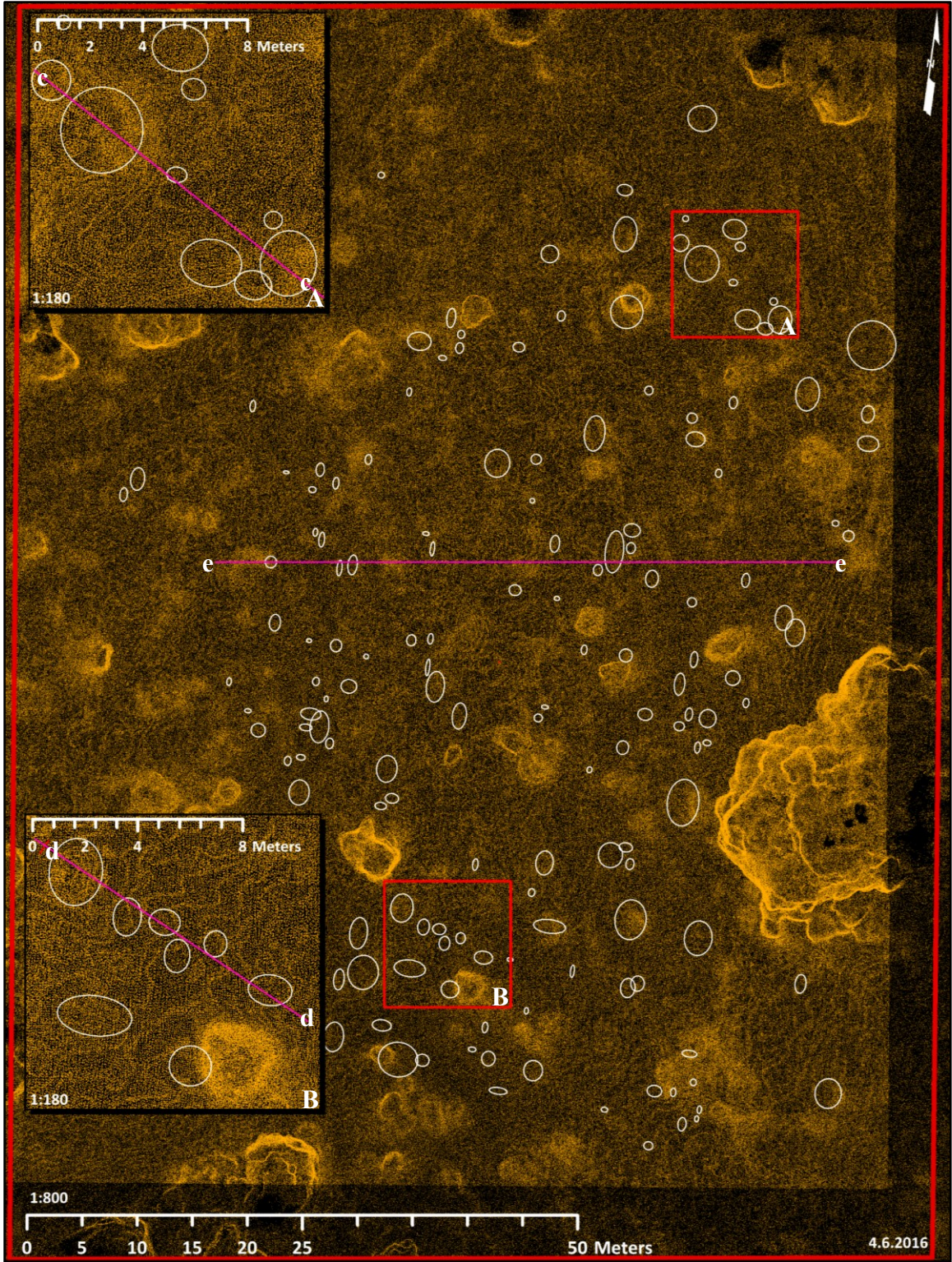


**Figure 9.** Combined dense point cloud. (A) Northeast inset and (B) southwest inset. Transects (c)(d)(e) shown as pink lines (see Fig. 10). Plot-ellipses shown as white ellipses.

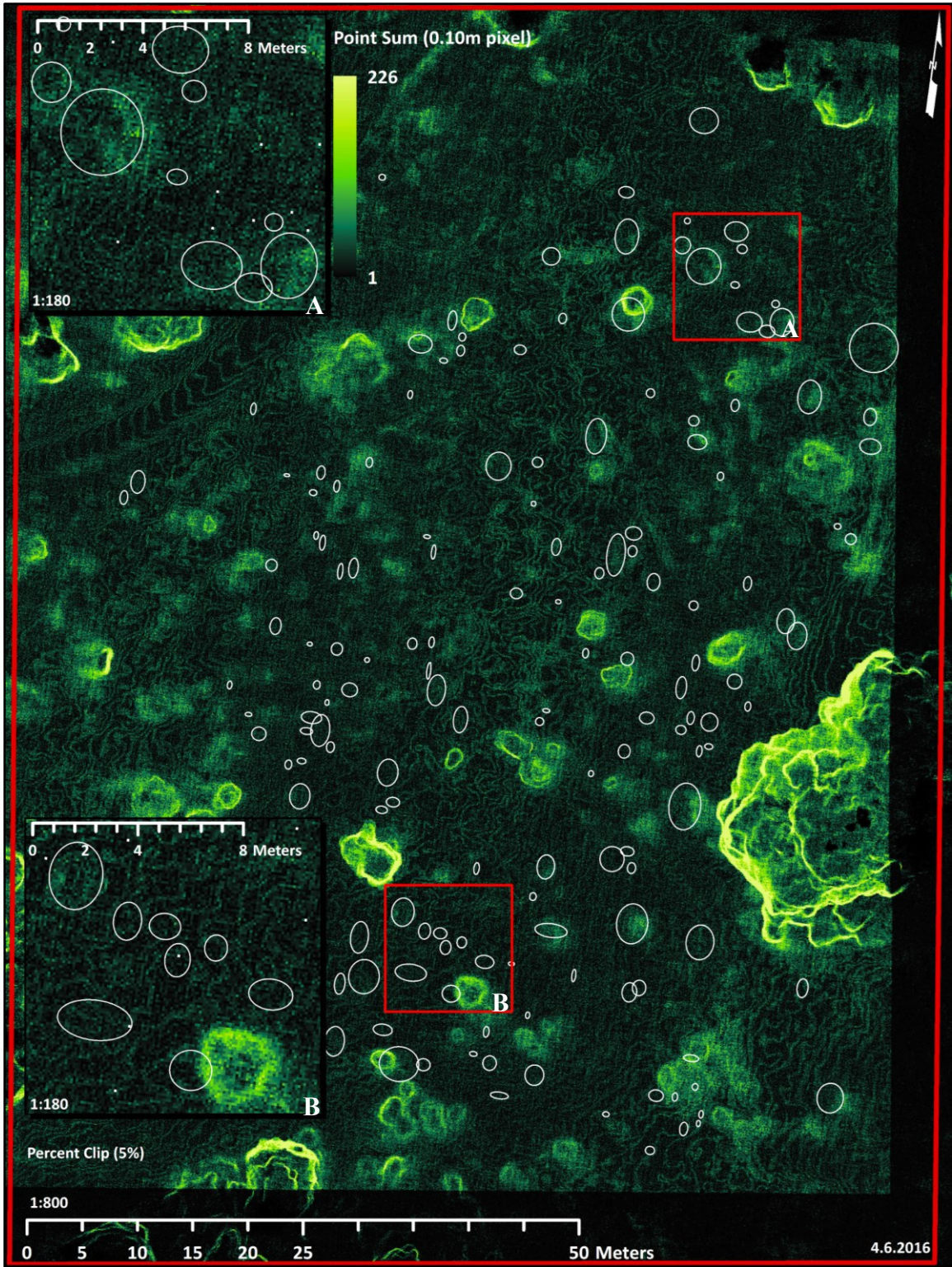


**Figure 10.** Point sum raster. (A) Northeast inset and (B) southwest inset. Plot-ellipses shown as white ellipses.

encompasses plot-ellipses. Minor visual data gaps can however be seen in the northern outer section of the study site where “point shadows”, or areas with little to no points, are found on the northern halves of several shrubs (Fig. 9-10).

Individual tree and shrub species are the most prominent features that possess the highest mean point densities within the study site. This can be seen in the live-oak mott located on the eastern edge of the study site and in various shrubs represented as brighter orange (Fig. 9) or brighter green (Fig. 10) objects. The outer-canopies of these trees and shrubs also demonstrate a higher point density and lower point spacing, or decreased distance between individual points, when compared to the lower point density and higher point spacing of the inner-canopy. This produces a donut-like visual effect for small to medium volume shrubs and a contour-like effect for the large volume trees where the outer-canopy of these trees clearly exhibit highlighted edges of foliage.

Regarding the within-canopy (both inner and outer-canopy) point distribution variances of trees and shrubs, PP cacti plots overall demonstrate a lower point density and thus a higher point spacing within-canopy. Point distribution patterns for PP cacti plots can generally be described as clustered and asymmetrical (Fig. 9-10; inset A). While individual cladodes, or the leaves of any vegetation species within the study site, are indistinguishable based on the dense point cloud and point sum visualizations; various minute point clusters or areas of a relatively higher within-canopy point density may reasonably correspond to cladode groups. This asymmetrical “point density cluster” characteristic is indeed most prevalent for PP cacti plots with a high CLAD<sub>COUNT</sub>, ECV, and ECSA values, where PP cacti plots with high ECV values defined by high PP<sub>HEIGHT</sub> values overall demonstrate greater within-canopy point density and point spacing

variations. This asymmetrical point density cluster characteristic can best be seen in several larger plot-ellipse polygons shown in inset A of Fig. 9 and 10. PP cacti plots with low ECV values or low  $PP_{\text{HEIGHT}}$  values demonstrate only minor within-canopy point density and point spacing variations and generally show less point density cluster characteristics. PP cacti plots with high  $CLAD_{\text{COUNT}}$  and ECC values but low  $PP_{\text{HEIGHT}}$  values also show far less within-canopy variances (Fig. 10; inset B).

When examining areas of transition between PP cacti plots and surrounding grassy land cover, PP cacti plots generally demonstrate a more gradual change in point density and point spacing in contrast to the “harder” boundaries exhibited by trees and shrubs. Moreover, grassy land cover or land cover within the study site dominated by short to tall grass species demonstrate point distribution patterns different from those of PP cacti plots with high  $CLAD_{\text{COUNT}}$  and ECV values or those of large volume shrubs and trees. Specifically, grassy land cover exhibits a unique contour-like point distribution pattern represented by wide curvilinear banded areas of low point density and high point spacing, separated by thin banded areas of high point density and low point spacing. This contour-like point distribution pattern is most evident in the point sum raster (Fig. 10), though it is also observed in the dense point cloud (Fig. 9), and in the 3-D low oblique perspective of the dense point cloud (Fig. 13A).

Differences in this contour-like pattern relative to the height and distribution of grassy land cover, or the relative ground coverage, can also be seen in the point sum raster (Fig. 10) where several central sections of the study site that possess taller and more dense grass coverage are represented by “blurry” less pronounced contour-like patterns with a relatively even point density. In contrast, the southeastern corner, eastern

edge, and western edge of the study site show more distinct and well-defined contour-like patterns which represent areas of short grass height and sparse ground coverage. The most prominent contour-like point distribution pattern is nonetheless exhibited by barren land cover which corresponds to the gravel road located in the northern half of the study site (Fig. 10).

Similar to within-canopy point distribution patterns, PP cacti plots with a high  $CLAD_{COUNT}$  and high ECV values defined by higher  $PP_{HEIGHT}$  values instead of higher ECC values, demonstrate a higher point density and lower point spacing which more visibly separates them from the point distribution patterns of surrounding grassy land cover. These high volume PP cacti plots conversely become more distinguishable when surrounding grassy land cover is short and sparse. PP cacti plots with low  $PP_{HEIGHT}$ , ECC, and ECV values that are located in tall and dense grassy land cover are thus generally indistinguishable from the point distribution patterns of surrounding grassy land cover (Fig. 9-10; inset B). This characteristic is especially prevalent in the central western half of the study site where most PP cacti plots demonstrate low  $PP_{HEIGHT}$ ,  $CLAD_{COUNT}$ , ECC, and ECV values and are surrounded by tall, dense grass coverage.

Examples of point elevation-derived visualizations for the study site can be seen in Fig. 11-14, where Fig. 11 shows the maximum point-Z TIN and Fig. 12 shows the point-Z range or difference raster (maximum point-Z – minimum point-Z/0.01 m<sup>2</sup>). Much like point distribution patterns, distinct maximum point-Z and point-Z range patterns can be seen for within-canopy areas of trees and shrubs which distinguish them from PP cacti plots. Overall, trees and shrubs possess a greater variation in maximum point-Z and point-Z range and are thus represented as features with multiple elevation

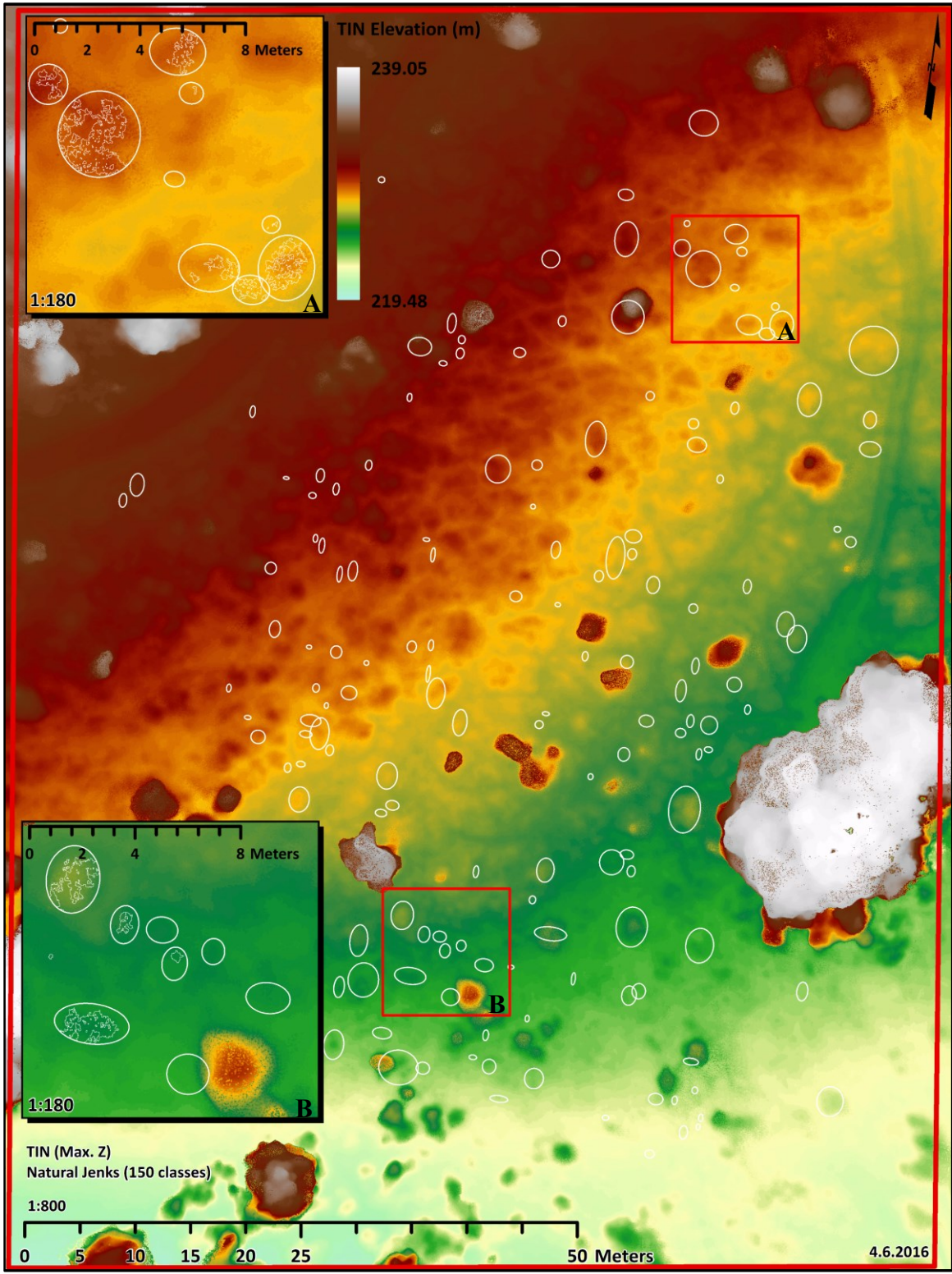


**Figure 11.** Maximum point-Z TIN. (A) northeast inset with PP-class segment overlay (faded white). (B) southwest inset showing PP-class segment overlay (faded white). Plot-ellipses shown as white ellipses.

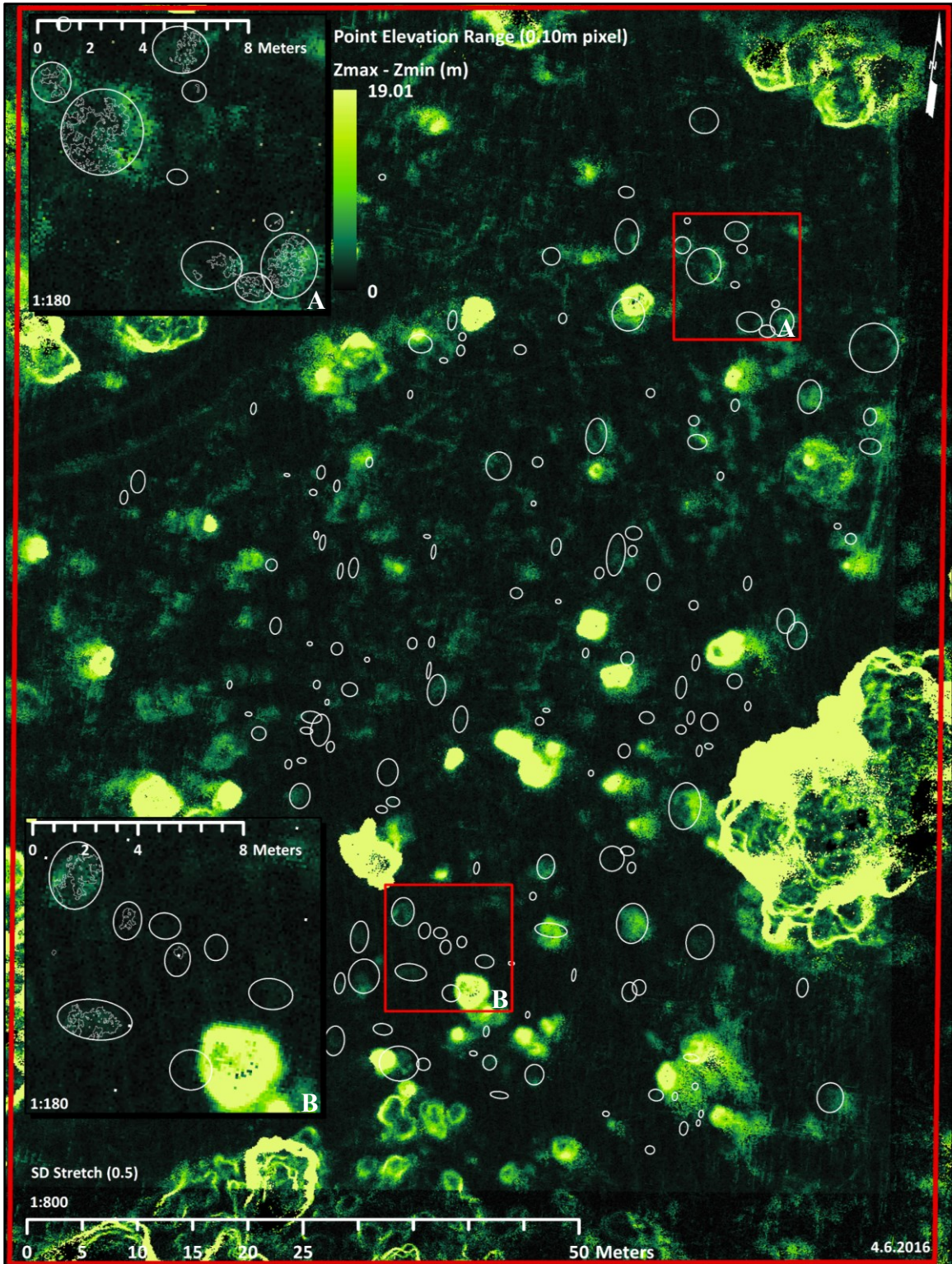


**Figure 12.** Point Z-range raster. (A) Northeast inset showing PP-class segment overlay (faded white). (B) Southwest inset showing PP-class segment overlay (faded white). The greatest variation in elevation ranges between land cover features is apparent in the northern half of study site. Plot-ellipses shown as white ellipses.

classes evident in the maximum point-Z TIN (Fig. 11). This greater elevation change is also evident in the point-Z range raster where trees and shrubs are generally represented as nearly solid bright green objects in comparison to PP cacti plots. While trees and shrubs represented in the maximum point-Z TIN lack the multiple inner-canopy holes found in the dense point cloud and point sum raster, corresponding inner-canopy hole features and highlighted foliage edges of the outer-canopy edge, represented by a high point-Z range, are evident in the point-Z range raster. This characteristic is especially prevalent in the live-oak mott located on the western edge of the study site and within various shrubs located on the southern edge of the study site (Fig. 12). Overall, PP cacti plots demonstrate less within-canopy maximum point-Z or point-Z range variances.

Regarding within-canopy point-Z range patterns that may correspond to similar patterns reported for the point density cluster characteristic, PP cacti plots with high  $CLAD_{COUNT}$  and  $ECV$  values indeed demonstrate unique asymmetrical changes in point-Z range patterns. This characteristic can be seen alongside plot-ellipse and plot-segment polygons in insets A and B of Fig. 12. In comparison to the point-Z range patterns of the surrounding grassy land cover, larger PP cacti plots with high  $CLAD_{COUNT}$  and  $ECV$  values generally demonstrate a greater visible contrast or a drastic increase in maximum point-Z elevations and point-Z ranges. In contrast, PP cacti plots with low  $CLAD_{COUNT}$ ,  $ECC$ , and  $ECV$ , values defined by low  $PP_{HEIGHT}$  values remain difficult to visibly distinguish and possess maximum point-Z and point-Z ranges too similar to discern from those of grassy land cover. This characteristic can be seen in insets A and B of Fig. 11 and Fig. 12, which show several nearly indistinguishable small PP cacti plots (low  $ECC$  values) in relation to more visible larger PP cacti plots (high  $ECC$  values).

Unlike the contour-like point distribution patterns evident for grassy land cover, in the maximum point-Z TIN and point-Z range visualizations, grassy land cover is instead represented as distinct grass bunches or “tussocks” which exhibits more homogeneity across the study site compared to the contour-like point distribution pattern. Since many of these tussocks show maximum point-Z and point-Z range patterns similar to PP cacti plots with high ECC values but low  $PP_{HEIGHT}$  values, many of these PP cacti plots, even those with high  $CLAD_{COUNT}$  and ECSA values, remain indistinguishable from tussocks. This characteristic is particularly evident in the central and northern sections of the study site, which possess prominent tallgrass tussocks in contrast to the shorter sparser grass coverage in the southern section with few tussocks (Fig. 11-12).

Similar to patterns found in the dense point cloud, point sum raster, and maximum point-Z TIN, the point-Z range raster demonstrates that PP cacti plots with high  $CLAD_{COUNT}$  values and ECV values defined by high  $PP_{HEIGHT}$  values generally demonstrate greater point-Z ranges that better distinguish them from surrounding grassy land cover, which has lower maximum point-Z and point-Z range values. PP cacti plots with high ECC,  $CLAD_{COUNT}$ , and ECSA values, but low  $PP_{HEIGHT}$  values and thus low ECV values, are less distinguishable. This effect can best be seen in Fig. 12 in the northeastern corner of the study site where several PP cacti plots with high ECC and  $CLAD_{COUNT}$  values are hard to visually discern from surrounding grassy land cover. Overall, PP cacti plots with high  $CLAD_{COUNT}$ ,  $PP_{HEIGHT}$ , and ECV values are the most distinguishable when surrounding grassy land cover is short and sparse or at least when their point-Z ranges are greater than those of surrounding land cover.

Examples of minor and major undulations in point elevations that correspond to

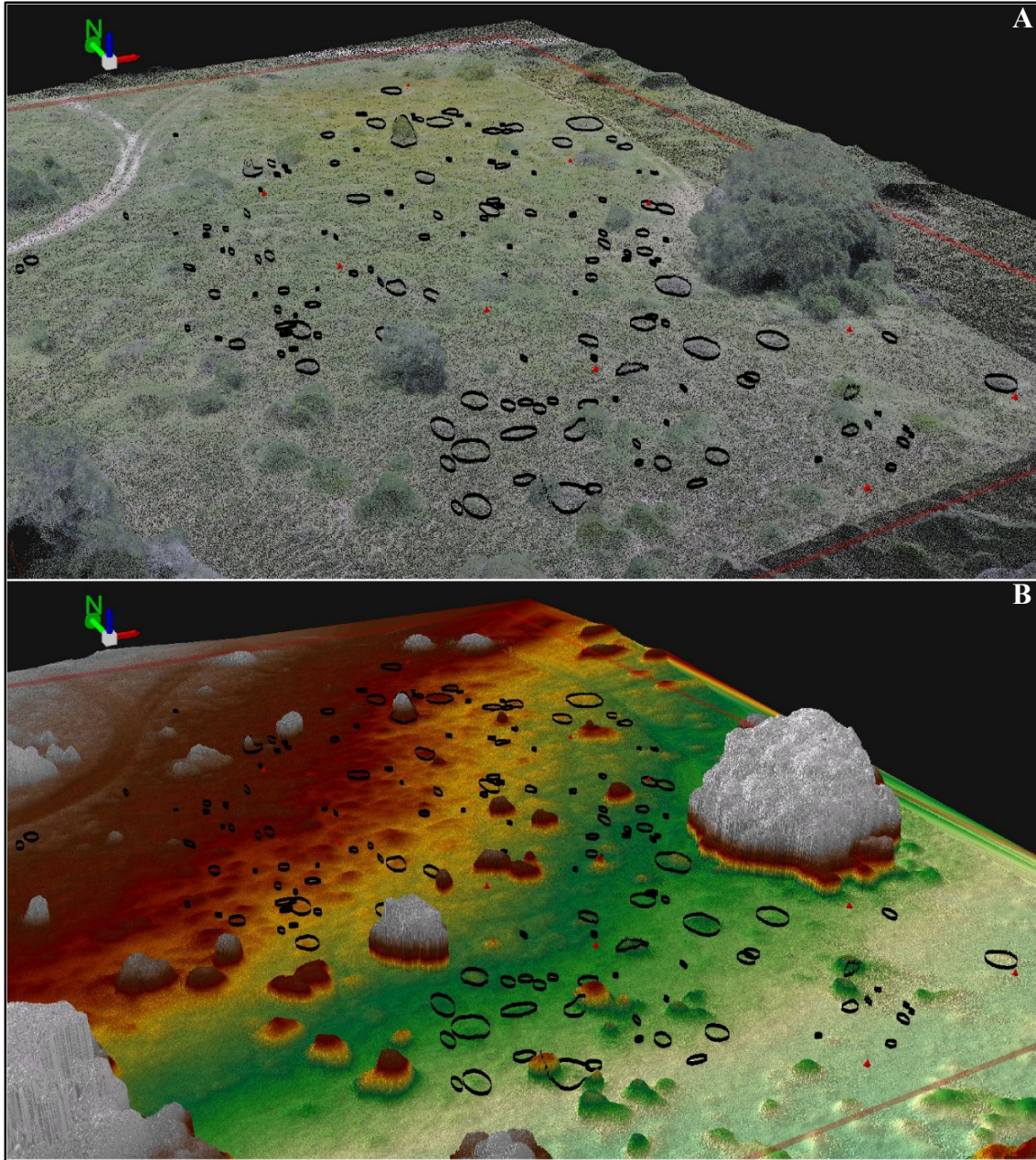


**Figure 13.** 3-D low-oblique perspectives of dense point cloud and TIN. (A) View of combined dense point cloud showing point RGB (123) values. (B) View of maximum point-Z TIN. Plot-ellipses are shown as black 3-D ellipses and GCPs are shown as small red cones.

PP cacti plots and surrounding land covers can be seen in Fig. 13 which shows a southeastern oriented 3-D low oblique perspectives of the maximum point-Z TIN and a RGB encoded dense point cloud. Differences in point elevations can also be seen in Fig.

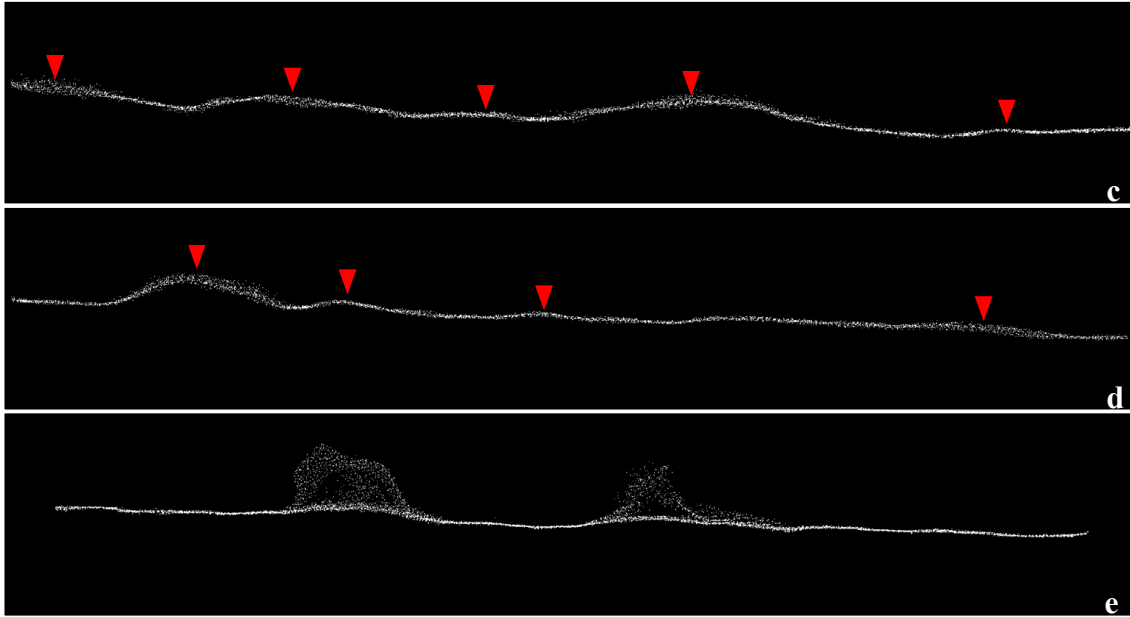


**Figure 14.** 2-D transects of dense point cloud (see Fig. 9). (c) Northeast transect. (d) Southwest transect. (e) Central transect. Transects represent a swath width of approximately 0.50 m; transect lengths are distorted for visualization purposes.

14 which show several 2-D transects of the dense point cloud referenced in Fig. 9. The 2-D transects demonstrate how individual points are vertically distributed. Points that correspond to grassy land cover are largely distributed along a thin line or their collective point-Z range is low. Points located within PP cacti plots are largely distributed along a coarse line or their collective point-Z range are noticeably higher than surrounding land cover point-Z ranges.

## **7.2 Classification of Prickly Pear Cacti**

FLS and Edge-based OBIA segmentation of the study site's RGB orthophoto (2.25 cm<sup>2</sup>/pixel) resulted in a total of 389,005 individual segments with minimum, maximum, and mean segment areas of 0.000225 m<sup>2</sup> or 2.25 cm<sup>2</sup> (1 pixel), 27.75 m<sup>2</sup> (123,347 pixels), and 0.025 m<sup>2</sup> (110 pixels) respectively. Out of the 86 original attributes calculated from the spatial, spectral, and textural properties of RGB, PCA, and IHS bands, 66 final attributes per segment were selected using a RF-based weighted attribute selection algorithm. Attributes for separate training and testing datasets that represented a random selection of segments for known PP cacti (PP) and non-PP cacti (non-PP) land cover classes were then used for supervised classification of the 389,005 segments utilizing an RF classification model. A total processing time of 9 minutes and 49 seconds was reported by Weka v3.7.13 for training, testing, and classification phases within a Windows 7 64-bit operating system that used a 2.5GHz Intel Core i7-4710MQ CPU, 32 GB of RAM, and an allotted heap size (maximum memory) of 1024MB for Weka v3.7.13. A summary and detailed accuracy report for training and testing phases can be seen in Table 10 and Table 11. A thematic map showing the results of RF-classified OBIA segments into PP and non-PP land cover classes is provided in Fig. 15.

### **7.21 RF-Classification and Detection Results**

During the training phase, 17,691 training segments (PP-class=918 segments/non-PP-class=16,773 segments) were used to train a 300 tree RF classification model using an 8-fold cross-validation strategy in a processing time of 3 minutes and 11 seconds. Machine learning accuracy measures reported for the optimally-trained RF model

**Table 10.** Summary accuracy report: training/testing phases of RF model.

Accuracy	Training	Test
# Correctly Classified Segments	17,280	17,428
% Correctly Classified	97.68%	96.51%
# Incorrectly Classified Segments	411	630
% Incorrectly Classified	2.32%	3.49%
Total # of Segments	17,691	18,058
Kappa Statistic	0.7354	0.6439

**Table 11.** Confusion matrix and accuracy measures: training/testing phases of RF model.

Phase	Class	Confusion Matrix		Accuracy Measure			
		PP	non-PP	TP Rate <sup>1</sup>	FP Rate <sup>2</sup>	F-Measure	ROC Area
Train	PP	608	310	0.662	0.006	0.747	0.984
	non-PP	101	16,672	0.994	0.338	0.988	0.984
	Weighted $\bar{X}$	-	-	0.977	0.32	0.975	0.984
Test	PP	615	522	0.541	0.006	0.661	0.958
	non-PP	108	16,813	0.994	0.459	0.982	0.958
	Weighted $\bar{X}$	-	-	0.965	0.431	0.961	0.958

<sup>1</sup>True Positive Rate<sup>2</sup>False Positive Rate

resulted in an overall accuracy of 97.68% (Table 10) with a ROC Area value of 0.984 and F-measure values of 0.747 and 0.988 for PP and non-PP classes, respectively (Table 11). During the testing phase 18,058 separate test segments (PP-class=1,137 segments, non-PP-class=16,921) were used to test the trained RF classification model within a processing time of 3 minutes and 8 seconds.

Machine learning accuracy measures reported for the tested RF model resulted in an overall accuracy of 96.51% (Table 10) with a ROC Area value of 0.958 and F-measure values of 0.661 and 0.982 for PP and non-PP classes, respectively (Table 11).

The tested RF classification model was then used to classify the 389,005 segments within

**Table 12.** Confusion matrix for pixel-based accuracy assessment.

Class		Class		
		PP	non-PP	Total
%	PP	<b>54.17</b>	1.31	5.96
	non-PP	45.83	<b>98.69</b>	94.04
	Total	100	100	100
Pixel	PP	<b>98,783</b>	24,726	123,509
	non-PP	83,561	<b>1,865,297</b>	1,948,858
	Total	182,344	1,890,023	2,072,367

**Table 13.** Classification accuracies and errors for pixel-based accuracy assessment.

Error		Class	
		PP	non-PP
%	Commission	20.02	4.29
	Omission	45.83	1.31
	Producer	54.17	98.69
	User	79.98	95.71
Pixel	Commission	24,726/123,509	83,561/1,948,858
	Omission	83561/182344	24,726/1,890,023
	Producer	98,783/182,344	1865297/1890023
	User	98,783/123,509	1,865,297/1,948,858

a processing time of 3 minutes and 30 seconds which resulted in a total of 9,268 PP-class and 379,737 non-PP class segments. PP class segments possessed minimum, maximum, and mean segment areas of 0.00045 m<sup>2</sup> or 4.5 cm<sup>2</sup> (2 pixels), 2.51 m<sup>2</sup> (11,160 pixels), and 0.027 m<sup>2</sup> (121 pixels) while non-PP class segments possessed, minimum maximum, and mean segment areas of 0.000225 m<sup>2</sup> or 2.5 cm<sup>2</sup> (1 pixel), 27.53 m<sup>2</sup> (122,358 pixels), and 0.025 m<sup>2</sup> (110 pixels).

Classified segments were then used to create a binary PP and non-PP class thematic raster of the study site (Fig. 15) where a pixel-based accuracy assessment based

on the separate testing dataset (18,058 segments) resulted in an overall classification accuracy of 94.77 % and a Kappa value of 0.62, which satisfied study objective classification requirements for statistical analysis. Pixel-based accuracy reports and classification errors can be seen in Tables 12-13. Individual classification accuracies resulted in 54.17% and 98.69% for PP and non-PP classes (Table 12). Producer's and user's classification accuracies resulted in 54.17% and 79.98% for the PP class and 98.69% and 95.71% for the non-PP class, respectively (Table 13). Omission (1 - producer accuracy) and commission (1 - user's accuracy) errors resulted in 45.83% and 20.02% for the PP class and 1.31% and 4.29% for the non-PP class, respectively (Table 13).

Detection accuracy was calculated by determining the total number of individual plot-ellipses which contained (detected) or didn't contain (undetected) a PP-class segment. The total number of detected (n=108) and undetected (n=50) plot-ellipses were then divided by the total number of plot-ellipses (n=159) prior to the four plot-ellipses removed for statistical analysis. This resulted in a positive detection rate of 67.92% and a negative detection rate of 31.45%; otherwise approximately 2/3 of all PP cacti plots within the study site were detected.

Visualization of detected and undetected plot-ellipses in relation to PP and non-PP classes and their geographic distribution across the study site is provided in the PP and non-PP thematic land cover map (Fig. 15), which shows detected plot-ellipses as those which contain at least one PP class pixel. Graphs of detected and undetected plot-ellipses in relation to their respective CLAD<sub>COUNT</sub>, PP<sub>HEIGHT</sub>, and ECC field metrics can be seen in Fig. 16. A quantile classification of CLAD<sub>COUNT</sub> values used in statistical

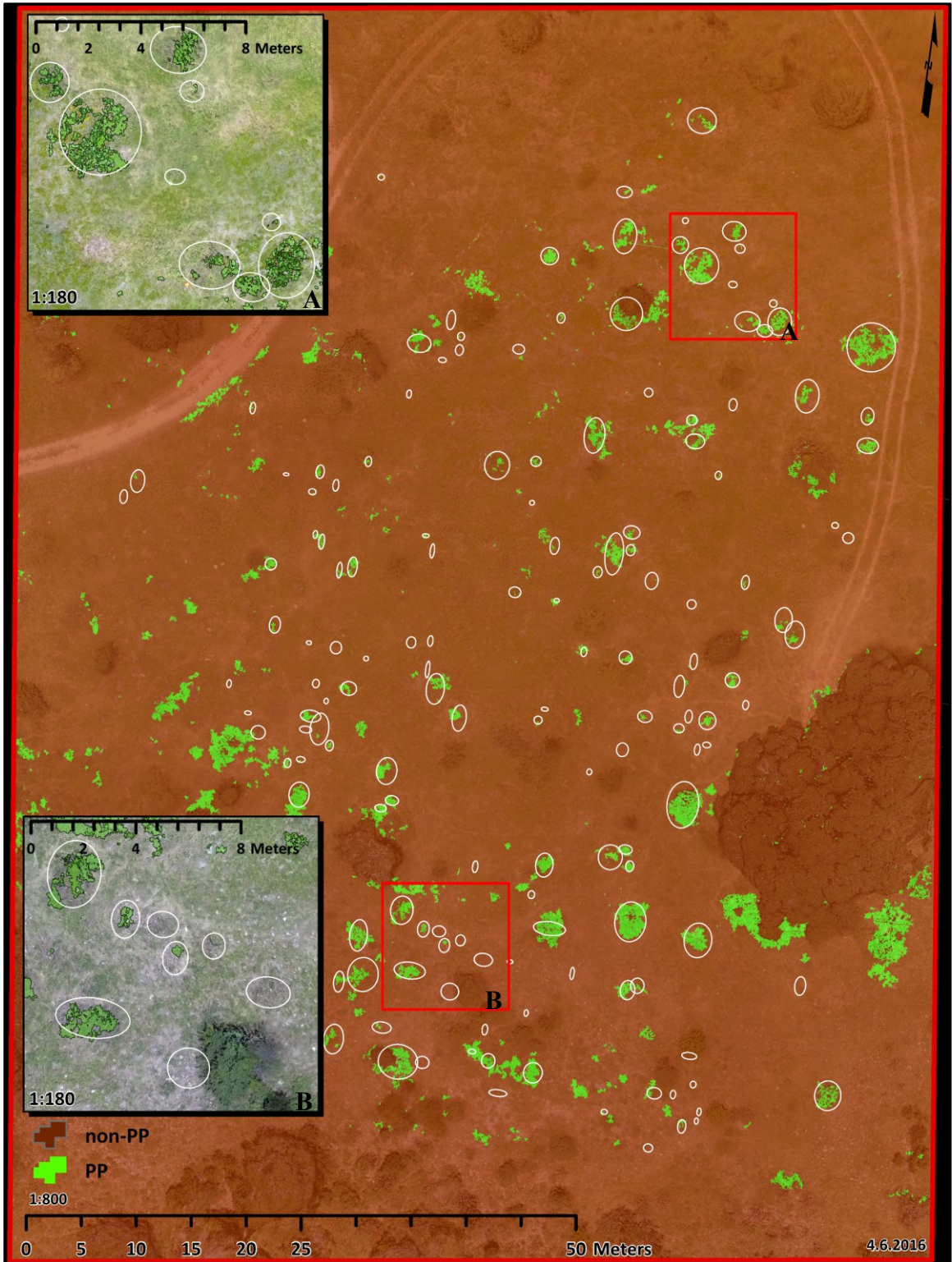


**Figure 15.** PP and non-PP thematic land cover map. (A) Northeast (A) and (B) southwest insets show PP class segments overlaid on RGB orthophoto. Plot-ellipses shown as white ellipses.

analysis (n=155) into 3 qualitative size classes of 53 “small” ( $7 < \text{CLAD}_{\text{COUNT}} \leq 23$ ), 51 “medium” ( $27 < \text{CLAD}_{\text{COUNT}} \leq 52$ ), and 51 “large” ( $52 < \text{CLAD}_{\text{COUNT}} \leq 389$ ) PP cacti plots can also be seen in Fig. 16A. Qualitative size class positive detection rates are reported at 32.07% (17 detected) for small plot-ellipses, 76.47% (39 detected) for medium plot-ellipses, and 96.08% (49 detected) for large plot-ellipses. Conversely, negative detection rates are reported at 67.93% (35 undetected), 21.57% (12 undetected), and 3.92% (2 undetected) for small, medium, and large size classes, respectively.

### **7.22 Classification Accuracy, Segment Geometry, and Structure**

The overall classification accuracy of 94.77% and a positive detection rate of 67.92% ultimately allowed an adequate sample size (n=104) for generating 2-3 term predictive MLR models; though results also indicate that PP classification/detection accuracy is closely associated with both OBIA segment geometries and individual PP cacti structure.

For one, a low PP class producer’s accuracy of 54.17% means that 45.83% of PP ground-truth (testing dataset) pixels were classified incorrectly as non-PP while a non-PP class producer’s accuracy of 98.69% means that almost all non-PP ground truth pixels were classified correctly. These pixel-based class accuracy measures in combination with low PP class training and testing TP rates of 0.662 and 0.541 altogether suggest uncertainty during the RF-classification training/testing phases as the RF model tried to classify known PP segments using the mode of segment attributes (300 trees) that best contributed to overall classification accuracy.

While sample bias may explain some PP class uncertainty, the majority of

classification error is likely a product of how certain segment scale/geometry represented differences in PP cacti land cover within the RGB orthophoto. For instance, pixel areas comprised by medium to large plot-ellipses generally consisted of numerous small segments with high edge pixel ratios (pixels that border other segments) generated by a high spatial frequency of these pixel areas and the specific Edge/FLS algorithm settings. This characteristic was typically found in plot-ellipses with high CLAD<sub>COUNT</sub> and ECC values, decreased non-PP vegetated canopy coverage, and more cladode shadows. Small plot-ellipses with low CLAD<sub>COUNT</sub> and ECV values, mixed vegetation canopy coverage, and fewer cladode shadows were comparatively generated from pixel-areas of lower spatial frequency and consisted of few small segments with low edge pixel ratios (Fig. 8; inset A and B). Since edge pixels are known to largely determine textural and spectral segment attribute values which effects RF-classification, a skewed representation of the study site's various PP cacti land cover likely occurred. This means that the *high frequency* of segment attribute values derived from large PP cacti land cover had a higher probability of being selected by the RF model over the *low frequency* of segment attribute values from small PP cacti which generated "mixed segment" values closer to the segment values of non-PP land cover (trees, shrubs, grass, rocks, etc.).

A study by Laliberte and Rango (2009) concluded that a coarser segment scale range increased individual class accuracies compared to finer segment scales. Specifically, the authors found that larger segment scales reduced the number of edge pixels which then decreased within-class segment attribute value variances thereby increasing between-class separation. This suggests that there needs to be a balance between OBIA segment scale and PP class heterogeneity where optimal segment scales

should at least equalize within-class segment variances prior to RF-classification. Admittedly, comparisons and suggestions for universal segment scales of sUAS-SfM-derived imagery is difficult because spatial resolutions change from study to study. As suggested by Laliberte and Rango (2009), a practical solution involves several output classifications using different segment scales in order to determine which scale yields the highest class separation. An alternate solution may be to use sub-land cover classes designed to represent differences between small PP cacti and large PP cacti land covers.

Relationships between the detection rates of individual PP cacti and their respective field metrics may also provide reasons for PP misclassification errors. Small plot-ellipse (32.07%), medium plot-ellipse (76.47%), and large plot-ellipse (96.08%) positive detection rates directly indicate that detection probability is higher for larger PP cacti defined by higher CLAD<sub>COUNT</sub> values, a field metric significantly correlated with ECC ( $r=0.89$ ), ECV ( $r=0.93$ ), and ECSA ( $r=0.92$ ) values. In Fig. 16, plot-ellipse detection graphs sorted by CLAD<sub>COUNT</sub> (Fig. 16A) and ECC (Fig. 16C) show a progressive decay in individual detection as PP cacti field metric values decrease. While this relationship may partially be explained by physical relationships between CLAD<sub>COUNT</sub>, ECC, and OBIA segment scale/geometry as discussed previously, Fig. 16B alternately shows that detection may be related to PP<sub>HEIGHT</sub> values, which are less correlated to CLAD<sub>COUNT</sub> ( $r=0.74$ ) values but more correlated to ECV ( $r=0.75$ ) and ECSA ( $r=0.89$ ) values.

This may indicate that a significant percentage of PP cacti, despite having high CLAD<sub>COUNT</sub> and ECC values, may have gone undetected because they fell under a certain height range. This overall suggests errors caused by LoS during sUAS-image

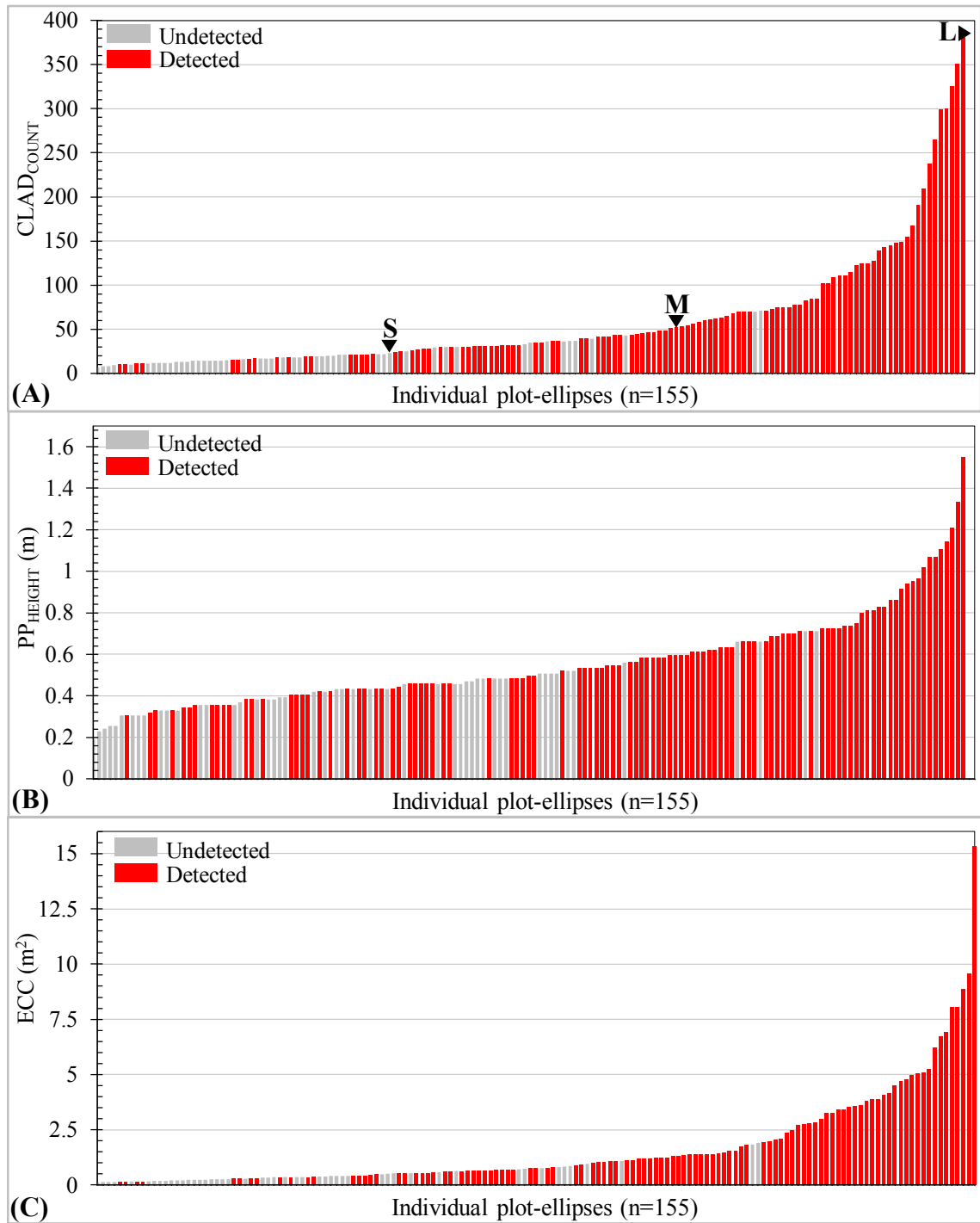


**Figure 16.** Plot-ellipse detection graphs sorted by CLAD<sub>COUNT</sub> (A), PP<sub>HEIGHT</sub> (B), and ECC (C). (A) CLAD<sub>COUNT</sub> graph shows a 3 class quantile classification for small (S), medium (M), and large (L). Graphs show 155 plot-ellipses used for statistical analysis; 159 plot-ellipses were used to calculate % detection.

acquisition. Regrettably, there are few studies that have substantiated the effects of vegetation structure on OBIA-segmentation/classification accuracy using sUAS-SfM-derived imagery. However, studies such as Fritz, Kattenborn, and Koch (2013); Lisein et al. (2013); Mathews and Jensen (2013); and Tonkin et al. (2014) have found that fine spatial scale features or low-volume vegetation architectures (tree stems, leaf-off undergrowth, grapevines, heather) can produce irregular clustering with low point densities that can skew or decrease sUAS-SfM dataset accuracies.

Possible solutions to these VHR rangeland vegetated land cover classification challenges may be to use data fusion techniques that incorporate Z-derived datasets and VHR imagery (CHM, DSM, TIN) into schemes using two basic strategies: (1) enhance segment scale/geometry for land cover by integrating rasterized sUAS-SfM-derived PH or elevation-derived datasets (slope, point density, roughness, etc.) into the OBIA segmentation process *prior to* classification (Blanchard, Jakubowski, and Kelly 2011); or (2) integrate post segmentation PH-derived or elevation-derived statistical attributes (PH mean, PH SD, PH variance, etc.) *within* classification models (Zhang, Xie, Selch 2013).

## 7.3 Prediction of Prickly Pear Cacti Structure

### 7.31 Predictive MLR Model Results

A summary of results for final plot-ellipse (n=155) and plot-segment (n=104) predictive MLR models of the 7 field metrics are provided in Table 14 which reports goodness of fit (K-Fold CV,  $R^2$ , and predicted vs. actual  $R^2$ ) and absolute error (RMSE,  $PRESS_{RMSE}$ ) values. Comparative plot graphs (predicted vs. actual) for plot-ellipse and plot-segment predictive MLR models of each field metric are also provided in Fig. 18a-d along with each model's multivariate regression equation. A summary of 1:1 plot-ellipse and plot-segment  $R^2$  values between selected descriptive predictors and field metrics can be referenced in Tables 7-9 (see Data Analysis; section 6.1).

Plot-ellipse MLR models utilized 8 different predictors for five 3-term models ( $CLAD_{COUNT}$ ,  $PP_{HEIGHT}$ , ECC, ECSA, and FWB) and two 2-term models (ECV and DWB). The  $PH_{COUNT}$  predictor was the dominant predictor and resulted in the prediction of four different field metrics ( $PP_{HEIGHT}$ , ECC, ECV, and DWB) followed by the  $PLOT-TIN_{SA}$  predictor which resulted in the prediction of three different field metrics ( $CLAD_{COUNT}$ , ECSA, and FWB). All other predictors ( $PH_{MAX}$ ,  $DIFF_{PCTL90-80}$ ,  $PLOT-TIN_{VOL}$ ,  $PH_{60PCTL}$ ,  $PH_{VAR}$ ) except  $DIFF_{PCTL90-20}$  were used in two predictive regression models. All field metrics predicted by plot-ellipse models, except  $PP_{HEIGHT}$ , demonstrated explained variation in field-measured values greater than 79% and unexplained variation no less than 21% based on predicted vs. actual  $R^2$  values.

**Table 14.** Results for plot-ellipse and plot-segment predictive MLR models.

Dependent (Y)		K-Fold R <sup>2</sup>	R <sup>2</sup>	RMSE	PRESS <sub>RMSE</sub>
Plot-ellipses (n=155)	CLAD <sub>COUNT</sub>	0.74	0.83	28.16	35.18
	PP <sub>HEIGHT</sub> (m)	0.48	0.60	0.14	0.15
	ECC (m <sup>2</sup> )	0.93	0.94	0.54	0.54
	ECV (m <sup>3</sup> )	0.89	0.91	0.42	0.46
	ECSA (m <sup>2</sup> )	0.77	0.83	0.66	0.77
	FWB (Kg)	0.76	0.84	11.24	14.09
	DWB (Kg)	0.81	0.88	3.48	3.84
Plot-segs. (n=104)	CLAD <sub>COUNT</sub>	0.75	0.80	34.33	36.17
	PP <sub>HEIGHT</sub> (m)	0.55	0.57	0.15	0.16
	ECC (m <sup>2</sup> )	0.70	0.85	0.97	1.09
	ECV (m <sup>3</sup> )	0.76	0.84	0.65	0.69
	ECSA (m <sup>2</sup> )	0.71	0.82	0.76	0.97
	FWB (Kg)	0.79	0.80	13.97	14.72
	DWB (Kg)	0.77	0.81	4.99	5.40

Similarly, K-fold CV R<sup>2</sup> values demonstrated explained variation greater than 73% and unexplained variation no less than 27%.

The prediction of ECC using a 3 term model based on PH<sub>COUNT</sub>, PH<sub>VAR</sub>, and PH60<sub>PCTL</sub> predictors resulted in the highest goodness of fit values with a K-fold CV R<sup>2</sup>=0.94, a predicted vs. actual R<sup>2</sup>=0.93, and a RMSE=0.54 m<sup>2</sup>. Prediction of ECV using only 2-terms based on PLOT-TIN<sub>VOL</sub> and PH<sub>COUNT</sub> predictors resulted in the second highest goodness of fit values with a K-fold CV R<sup>2</sup> =0.89, a predicted vs. actual R<sup>2</sup>= 0.91, and a RMSE=0.42 m<sup>3</sup>. The lowest goodness of fit values resulted from the prediction PP<sub>HEIGHT</sub> using a 3 term model based on PLOT-TIN<sub>VOL</sub>, PH<sub>COUNT</sub>, and PH60<sub>PCTL</sub> predictors with a K-fold CV R<sup>2</sup>=0.48, a predicted vs. actual R<sup>2</sup>=0.60, and an RMSE=0.14 m. Regarding statistical measures of error for plot-ellipse models, the predicted vs. actual RMSE and the RMSE of predicted errors (PRESS<sub>RMSE</sub>) are also reported in Table 13.

The greatest percent differences between RMSE and  $PRESS_{RMSE}$  values resulted in a difference of 22.50% (2.85 Kg) for FWB and 22.17% (7 cladodes) for  $CLAD_{COUNT}$ , while the lowest percent difference of 0.29% (0.00 m<sup>2</sup>) resulted for the prediction of ECC.

Plot-segment MLR models instead utilized only 7 different predictors for two 3-term models (ECC and ECSA) and five 2-term models ( $CLAD_{COUNT}$ ,  $PP_{HEIGHT}$ , ECV, FWB, and DWB). The  $SEG_{AREA}$  predictor was the dominant covariate and was included in the models of five different field metrics ( $CLAD_{COUNT}$ , ECC, ECV, FWB, and DWB) followed by the % PH,  $0.65 \leq x < 0.75m$  predictor which was included in the models for four different field metrics ( $CLAD_{COUNT}$ , ECV, FWB, and DWB). The  $SEG-TIN_{SA}$  predictor was included in models for three different field metrics ( $PP_{HEIGHT}$ , ECC, ECSA). All other predictors ( $PH65_{PCTL}$ , % PH,  $0.75 \leq x < 0.85m$ ,  $PH_{SD}$ ,  $DIFF_{PCTL90-80}$ ) were used in only one predictive regression model. All field metrics predicted by plot-segment models, except  $PP_{HEIGHT}$ , demonstrated explained variation greater than 79% with unexplained variation no less than 21% based on predicted vs. actual  $R^2$  values. Instead, K-fold CV  $R^2$  values demonstrated explained variation greater than 69% and unexplained variation no less than 31%.

Similar to plot-ellipse models, the highest goodness of fit values for plot-segment models resulted from the prediction of ECC using 3-terms based on  $SEG-TIN_{SA}$ ,  $SEG_{AREA}$ , and %PH,  $0.75 \leq x < 0.85m$  predictors with a K-fold CV  $R^2=0.70$ , a predicted vs. actual  $R^2=0.85$ , and a RMSE=0.97 m<sup>2</sup>. Similar to plot-ellipse model results, prediction of ECV using only 2-terms based on  $SEG_{AREA}$  and %PH,  $0.65 \leq x < 0.75m$  predictors resulted in the second highest goodness of fit values with a K-fold CV  $R^2$

=0.76, a predicted vs. actual  $R^2=0.84$ , and a  $RMSE=0.65\text{ m}^3$ . The lowest goodness of fit values also resulted from the prediction of  $PP_{\text{HEIGHT}}$  using a 3 term model based on  $PLOT-TIN_{\text{VOL}}$ ,  $PH_{\text{COUNT}}$ , and  $PH60_{\text{PCTL}}$  predictors with a K-fold CV  $R^2=0.55$ , a predicted vs. actual  $R^2=0.57$ , and an  $RMSE=0.15\text{ m}$ . The greatest percent differences between  $RMSE$  and  $PRESS_{RMSE}$  for plot-segment models were 23.78% ( $0.21\text{ m}^2$ ) for ECSA and 11.75% ( $0.12\text{ m}^2$ ) for ECC while the lowest percent difference of 3.73% ( $0.01\text{ m}$ ) resulted for prediction of  $PP_{\text{HEIGHT}}$ .

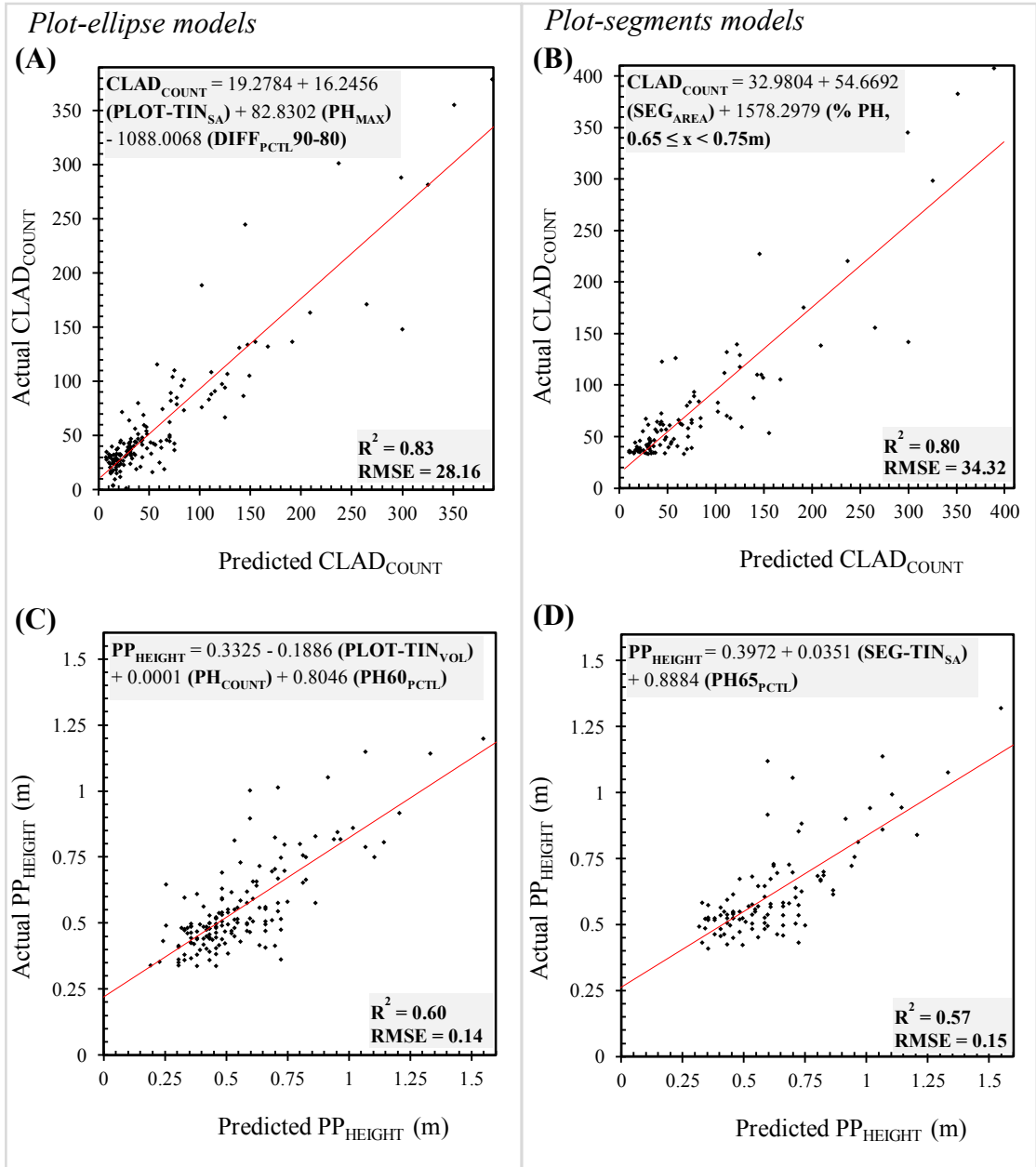


**Figure 17a.** Predictive MLR models:  $CLAD_{COUNT}$  (A)(B) and  $PP_{HEIGHT}$  (C)(D). Actual vs. predicted. Left graphs correspond to plot-ellipse models. Right graphs correspond to plot-segment models.

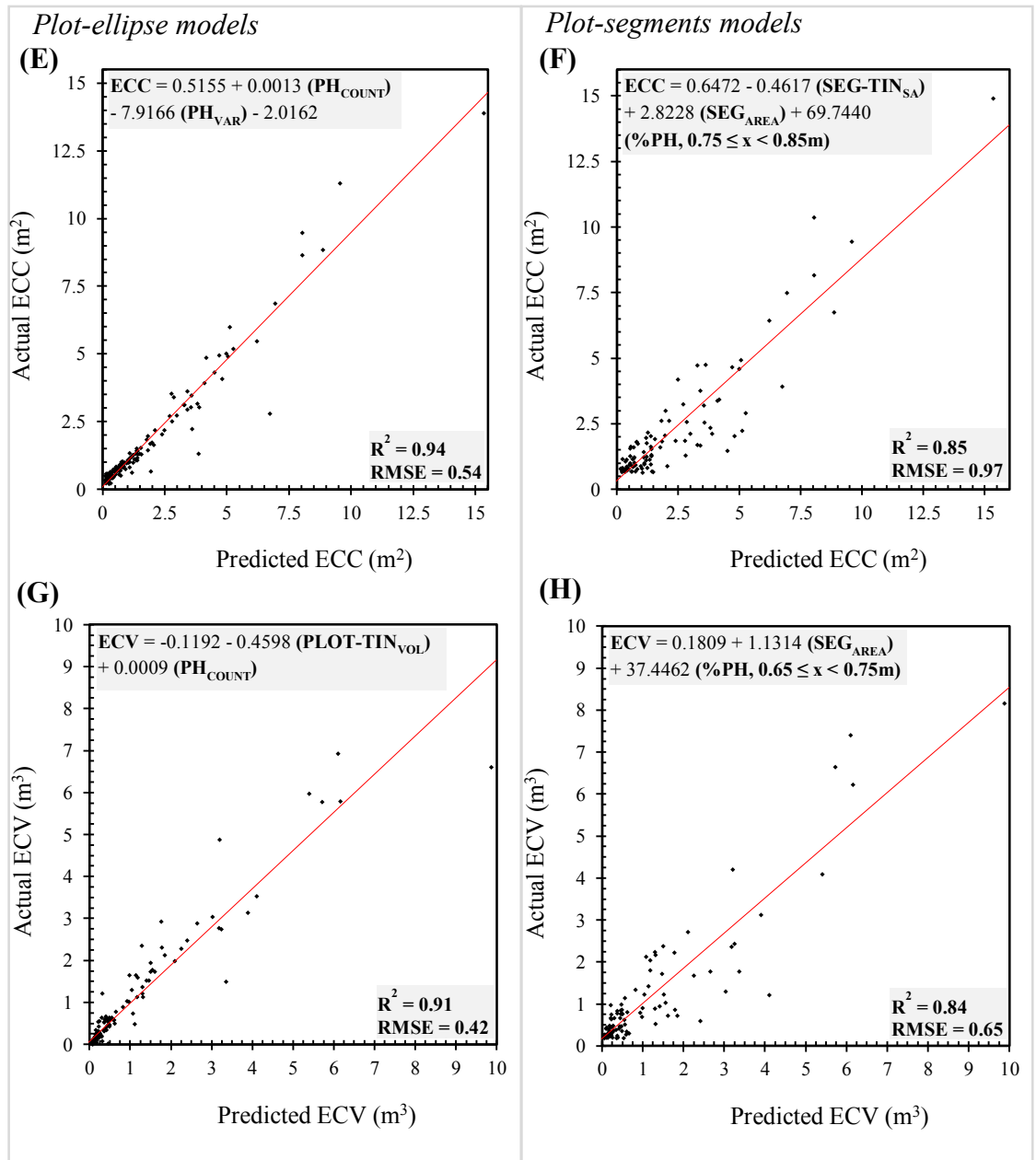


**Figure 17b.** Predictive MLR models: ECC (E)(F) and ECV (G)(H). Actual vs. predicted.

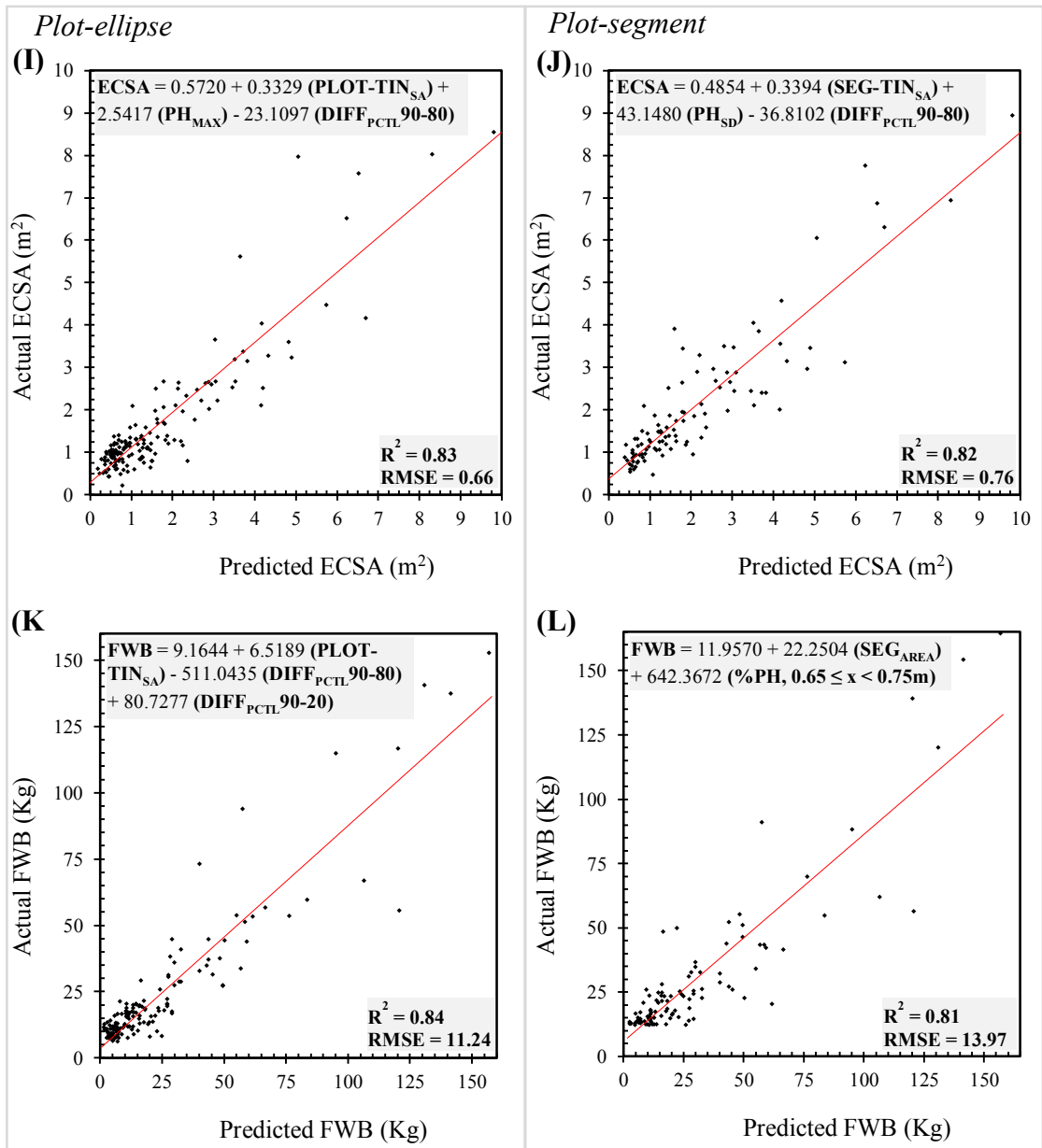


**Figure 17c.** Predictive MLR models: ECSA (I)(J) and FWB (K)(L). Actual vs. predicted.

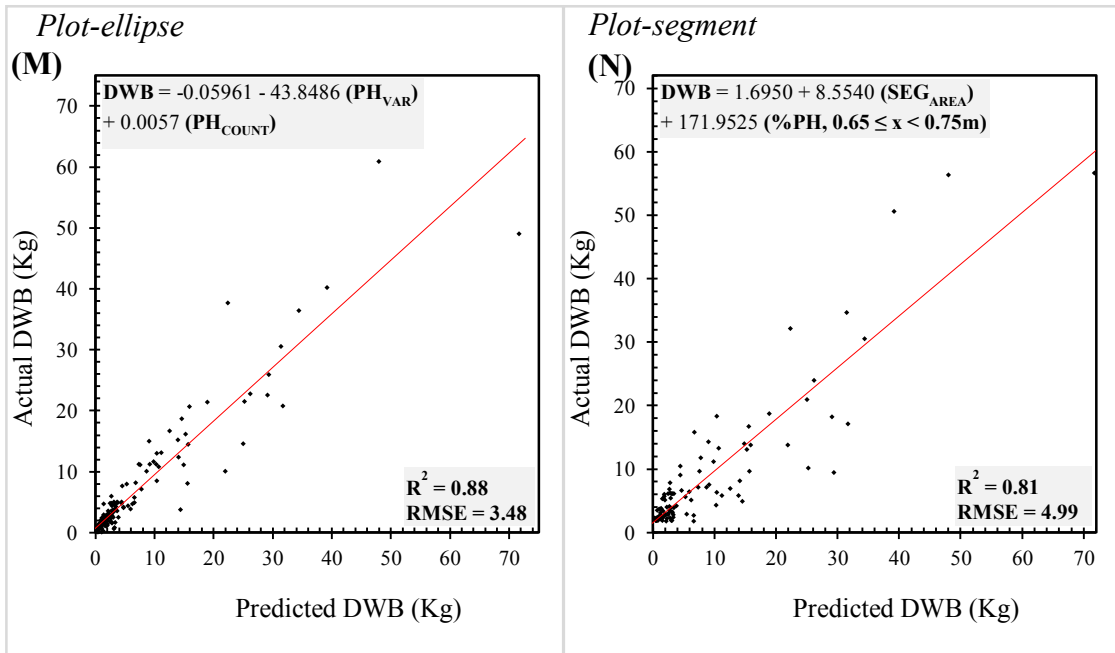


**Figure 17d.** Predictive MLR models: DWB (M)(N). Actual vs. predicted.

### 7.32 Plot Geometry, Selected Predictors, and Structure

Plot-ellipse and plot-segment predictive MLR models demonstrated significant results with K-fold and predicted vs. actual explanations of variation in field measured values greater than 70% for all field metrics, except  $PP_{\text{HEIGHT}}$ . Since few studies have yet to quantify the structure of any *Cactacea* species using sUAS-SfM PH-derived or TIN-derived predictors, direct comparisons of selected predictors and model performance is difficult. Still, both plot geometries (plot-ellipse/plot-segment) showed similar prediction results for ECC, ECV (highest  $R^2$  values), and  $PP_{\text{HEIGHT}}$  (lowest  $R^2$  values) field metrics, even given a difference of 51 observations and the large difference between the total number of plot-segment extracted points (66,920) and plot-ellipse extracted points (257,630) used to calculate predictor values.

In addition, for the moderate plot-segment K-fold ECC  $R^2=0.70$  and predicted vs. actual ECC  $R^2=0.85$  values, which represent plot-segment polygon areas (ECC) that presumptively eliminated many non-PP points, predictive MLR model results suggest that despite fundamental differences exhibited by plot geometries, the adequate prediction ( $R^2>80\%$ ) of many field metrics may not be heavily influenced by the presence of non-PP points. When referencing studies that used Lidar-based quantification of rangeland vegetation structure, a common source of prediction error is attributed to the inclusion or prohibition of points from non-target vegetation architectures/structures that can skew PH-derived predictor values (Spaete et al. 2011; Su and Bork 2006). Such findings were equally expected for this study given the unknown effects of certain vegetation architectures on sUAS-SfM point placement; though results indicate some degree of plot geometry flexibility in prediction accuracy. This may be

explained by the fact that surrounding grassy land cover generally consists of low point sums with low point Z-ranges. When calculating PH-derived or TIN-derived predictor values for medium to large PP cacti with high PH<sub>COUNT</sub> values, it is reasonable to assume that inclusion of some non-PP point values would not significantly skew the values of predictors selected by each predictive MLR model.

Likewise, of the 39 PH-derived statistical predictors originally calculated for statistical analysis, only 7 different PH-derived statistical predictors (PH<sub>MAX</sub>, DIFF<sub>PCTL90-80</sub>, DIFF<sub>PCTL90-20</sub>, PH<sub>60PCTL</sub>, PH<sub>65PCTL</sub>, %PH,  $0.65 \leq x < 0.75\text{m}$ , and %PH,  $0.75 \leq x < 0.85\text{m}$ ) were used in 5 plot-ellipse models and all plot-segment models. Importantly, these predictors mathematically represented the cluster of PHs located near the top of PP cacti or other vegetation canopies, otherwise the “point shell” (Fig. 14). This was expected given several findings presented by Dandois and Ellis (2010), Lisein et al. (2013), and Mathews and Jensen (2013) whose sUAS-SfM-derived dense point clouds of deciduous forests and trestle grapevines correspondingly featured point shell characteristics accredited to limited LoS penetration of vegetation foliage gaps.

Additionally, five plot-ellipse models (CLAD<sub>COUNT</sub>, PP<sub>HEIGHT</sub>, ECV, ECSA, and FWB) also utilized the two TIN-derived predictors that were calculated (PLOT-TIN<sub>SA</sub> and PLOT-TIN<sub>VOL</sub>) where four of these models (CLAD<sub>COUNT</sub>, PP<sub>HEIGHT</sub>, ECSA, and FWB) also utilized point shell predictors. Plot-ellipse predictions of ECC and DWB were the only models that didn't use TIN-derived and point shell predictor combinations, instead incorporating PH<sub>COUNT</sub> as the dominant predictor in 4 models; though PH<sub>COUNT</sub> was absent in all plot-segment models. Similar to plot-ellipse models, SEG-TIN<sub>SA</sub> was used in three plot-segment models (PP<sub>HEIGHT</sub>, ECC, and ECSA) where SEG<sub>AREA</sub> was used

in the remaining four models ( $CLAD_{COUNT}$ , ECC, ECV, FWB, DWB). In contrast, predictors which described the point distribution around a mean ( $PH_{SD}$  and  $PH_{VAR}$ ) were only chosen in one plot-ellipse and one plot-segment model as these variables generally provided weak 1:1 explanations of variance below 48% for all field metrics (Table 7). Therefore, it can be generally surmised that successful non-collinear models are those which incorporate 2-D area or 3-D surface area and volume-based predictors in addition to point shell predictors that inclusively define the “shape and shell” of PP cacti.

Furthermore, relationships between PP cacti structure and plot-ellipse model predictions can be seen in Fig. 18A-B which shows sorted ascending graphs of predicted vs. actual values of  $CLAD_{COUNT}$  (sorted by size class) and  $PP_{HEIGHT}$  field metrics. In Fig. 18A, the  $CLAD_{COUNT}$  predicted vs. actual values (significantly correlated with ECC, ECV, and ECSA) show that large plot-ellipses generally demonstrate decreased variance between predicted vs. actual values compared to small and medium plot-ellipses. As plot-ellipse size decreases,  $CLAD_{COUNT}$  predictions begin to slightly overestimate actual  $CLAD_{COUNT}$  values. In fact, predicted values overestimate the majority of small plot-ellipses. Similar model behavior can also be seen in Fig. 18B where predicted  $PP_{HEIGHT}$  values overestimate actual  $PP_{HEIGHT}$  values as  $PP_{HEIGHT}$  decreases and then slightly underestimates actual  $PP_{HEIGHT}$  values as  $PP_{HEIGHT}$  increases.

This behavior may partially be explained by the effects of sampling bias on model fit caused by the varying morphologies of a heterogeneous PP cacti population. This is a common limitation for predictive MLR models of biophysical metrics whose distributions are frequently nonparametric or near-logistic (A.F. Zuur et al 2009). This

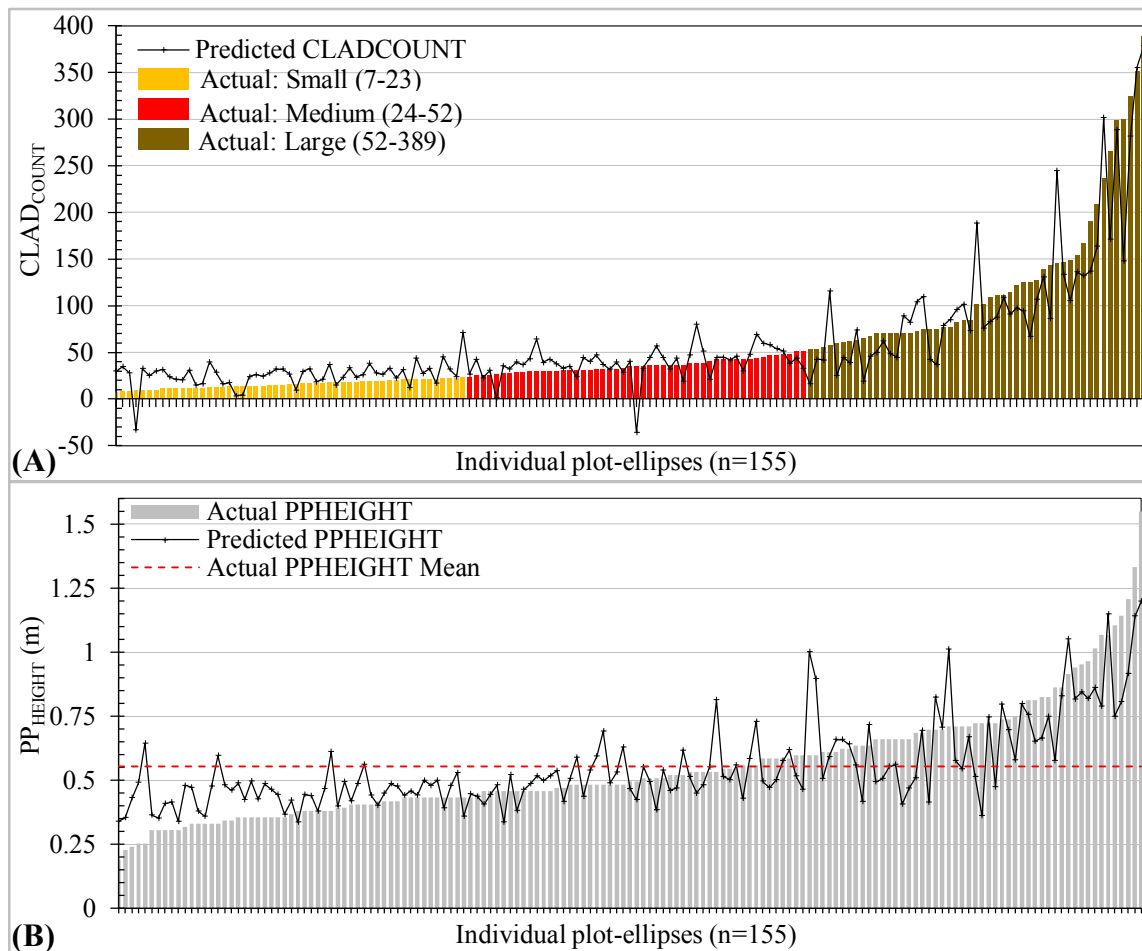


**Figure 18.** Sorted ascending graphs (actual vs. predicted): CLAD<sub>COUNT</sub> (A) and PP<sub>HEIGHT</sub> (B). (A) CLAD<sub>COUNT</sub> graph shows quantile classification for 3 sizes (small, medium, large) from actual values.

may be alleviated in future study efforts by integrating either higher term parametric regression models with perhaps larger training datasets, using semi-parametric generalized linear models (GLM), or even nonparametric regression models commonly used in ecology and Lidar-based forest structure prediction (K-nearest neighbor, RF, spline, kriging, etc.) (Guisan, Edwards, and Hastie 2002; Penner, Pitt, and Woods 2013). However, based on visual analysis results a certain percentage of overestimation error for small PP cacti may be still explained by LoS limitations. Since LoS has been known to influence output sUAS-SfM dense point cloud positional accuracy and density for target

vegetation features, it is reasonable to assume that small PP cacti amidst tallgrass cover with point characteristics virtually indistinguishable from tallgrasses will reasonably have a higher probability of generating skewed point-height-derived or TIN-derived predictor values.

#### **7.4 Sources of Error and Limitations of Practical Application**

In this study the RF model has demonstrated to be to be a robust classifier of a high number of complex OBIA segments attributed to its ability to model large nonparametric distributions; though classification accuracies have been known to be affected by skewed between-class training instances (Belgiu and Dragut 2016). Since the training dataset consisted of 918 PP class segments which covered of a total area of only 30.21 m<sup>2</sup> (0.30 % of the total study site area), compared to 16,773 non-PP class segments (5% randomized subset) which covered a total area of 3000.89 m<sup>2</sup> (30.02 % of the total study site area) it is reasonable to assume that a certain degree of sample size-based misclassification error occurred. While adopting novel OBIA classification accuracy assessment methods versus traditional pixel-based assessments may help better understand OBIA segment classification nuances (MacLeaan and Congalton 2012), more practical sample bias effects on misclassification are most likely attributed to how segment scale/geometry represents different PP cacti land cover and structural attributes. As such, ideal segment geometries and between-class sample sizes may be impractical for some rangeland ecosystems where target vegetation is scarce or whose canopy cover is heavily mixed with non-target vegetation species canopy cover.

Aside from proper site selection, one classification-based strategy to mitigate

sampling design limitations is to incorporate a feature/attribute selection scheme/algorithm (RF-based, regression-based, genetic algorithm, etc.) that eliminates redundant or collinear attributes prior to using a nonparametric supervised machine learning algorithm like the RF or SVM model. Decision tree-based attribute selection algorithms will also help overcome the “black box” nature of some RF models and boost interpretation of chosen RF model attributes while helping to generalize application to similar rangeland ecosystems.

For species-scale sUAS-SfM segmentation/classification of rangelands in near-climax successional stages or vegetation canopy is biodiverse and heavily mixed, it is suggested that training segment scale/geometry for target vegetated land covers capture the majority of a plant’s pixel-area for the majority of the population. At the same time, non-target land cover training segment scale/geometry needs to at least eliminate inclusion of target vegetated land cover to curb misrepresentation in a classification model. Admittedly, these strategies may need to vary for different rangeland ecosystems. For arid rangeland ecosystems with more isolated and distinct vegetation cover boundaries, it is predicted that segmentation/classification of PP cacti using sUAS-SfM may actually be more successful due to the higher probability of land cover class separation. For degraded rangelands defined by an extreme prevalence of interconnected PP cacti cover, the high number of “pure segments” would also likely produce successful segmentation/classification results.

Aside from sample bias, GPS GCP positional accuracy and sUAS-acquired digital image quality (resolution, distortion, noise, etc.) are common data collection-based sources of error known to affect a sUAS-SfM-derived dataset’s pixel (RGB) and point

(XYZ) values. These in turn affect the accuracy of OBIA segment scale/geometry, segment attribute values, and PH-derived statistical predictor values used in classification/detection and structural prediction models. More abstract sources of error that may equally affect pixel and point values are likely related to how SfM algorithms specifically capture and represent certain types of vegetation surfaces. Since these sources of error are yet quantified, it is unknown how to reduce or compensate for them in a rangeland environment and should be a focus for future study efforts if sUAS-SfM is to be used more effectively for vegetation analyses overall. As such, incorporating more expensive survey-grade GPS equipment, camera systems, and proprietary SfM software, etc. is not explicitly suggested to improve upon future OBIA classification/detection and structural prediction results for PP cacti or other rangeland vegetation species.

Instead, a more practical solution to curb data collection-based sources of error is to incorporate detailed flight planning designs that utilize an adequate number of total input images with a high percent of overlap (80-90%); where images from different flight plans use varying perspectives (nadir, high-oblique, low-oblique, etc.) and pixel-to-ground ratios that reflect target/non-target rangeland vegetation architectures (leaf orientation, leaf size, maximum height, reflectivity, etc.) and study objectives. A supplementary strategy is to utilize opportunistic sUAS image acquisition periods where rangeland conditions (scene illumination, phenology, ecological health, successional stage, etc.) also reflect study objectives. For this study, a sUAS image acquisition in winter after post-grazing conditions may have decreased non-target vegetation spectral and structural influences.

Lastly, computational efficiency is a realistic limitation to current and future

sUAS-SfM rangeland remote sensing research. This is because the SfM workflow is the most computationally demanding data processing phase whose efficiency is defined by the number and resolution (image file size) of input imagery and desired output dataset quality. An effective strategy to reduce SfM processing time is to initially acquire numerous digital stills with a high percent of overlap (80-90%) defined by a high acquisition interval, sUAS flight speed, and pixel-to-ground ratio. Redundant or excessive images can be easily removed prior to or during SfM modeling as opposed to having too few input images to model from.

## 8.0 CONCLUSIONS

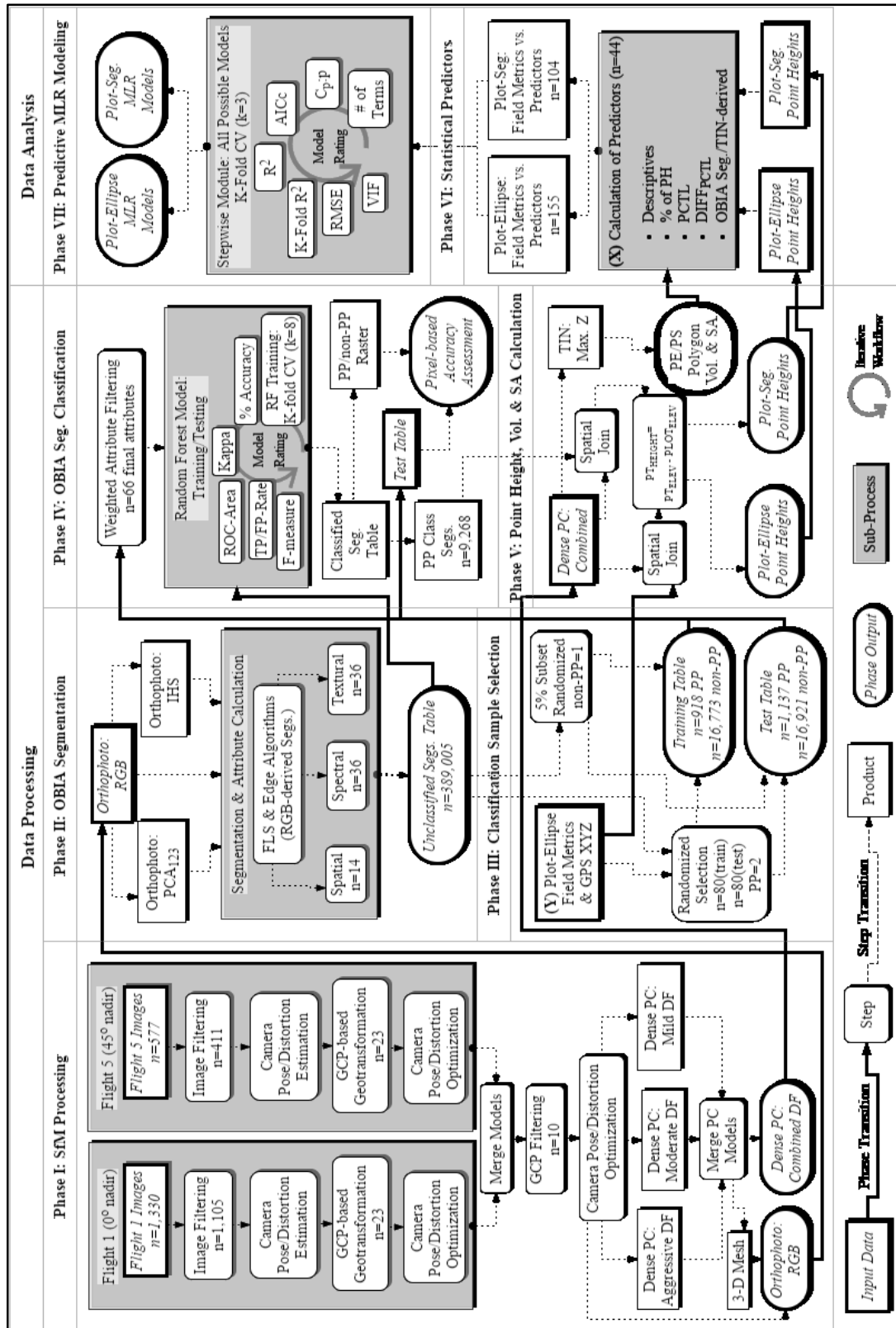
In this study, low altitude sUAS-acquired digital imagery of a near-climax rangeland was input into a proprietary SfM software whereby several VHR datasets were generated in order to quantify the species-scale presence/absence and structure of a heterogeneous PP cacti population. Results from the classification/detection of a sUAS-SfM-derived RGB orthophoto indicated that, despite significant overall classification accuracy and adequate detection rates, RF model uncertainty for the PP class can likely be attributed to segment scale/geometry, PP cacti structure, and LoS issues. Future strategies for segmentation/classification may therefore need to incorporate supplementary Z-based datasets which could better separate rangeland land covers *for* segmentation or *within* classification models. Results from predictive MLR models indicate that predictor combinations which describe both point “shell and shape” characteristics of the sUAS-SfM-derived dense point cloud, generally contributed to the highest R<sup>2</sup> values while prediction accuracy for small PP cacti in tallgrass cover may be largely determined by LoS limitations. Future studies need to more extensively examine relationships between vegetation surfaces/architectures and resulting sUAS-SfM point characteristics.

Overall, findings suggest that sUAS-SfM remote sensing techniques are a valuable tool in which to monitor and quantify low-statured rangeland vegetation where the proposed methodology can be feasibly adapted to the study of other understudied, keystone, or invasive rangeland vegetation species, ecological processes, and degradation processes. The proposed study therefore provides a proof of concept that is anticipated to improve upon existing data collection techniques associated with ESD/STM or other

labor intensive site-scale rangeland monitoring systems that can utilize on demand VHR datasets for a rapidly changing ecosystem vital to natural and agronomic systems. Still, further applications in other rangeland environments are essential for the identification of common limitations in order to streamline techniques and continuously resolve traditional rangeland remote sensing limitations caused by low-statured rangeland plant structure.

# APPENDIX SECTION

## Appendix A: Detailed Study Workflow Diagram



## Appendix B: OBIA Segment Attributes

Spatial Attributes	PP	non-PP
	$\bar{X}$	$\bar{X}$
Feature Length (m)	0.960	0.744
Feature Compactivity	0.190	0.212
Feature Convexity	1.357	1.247
Feature Roundness	0.438	0.480
Feature Elongation	1.667	1.678
Feature Main Direction	89.687	86.871
Feature Minor Axis (m)	0.140	0.109
Feature # of Holes	0.149	0.099

Textural Attributes		PP	non-PP
		$\bar{X}$	$\bar{X}$
<b>Red</b>	Range	37.84	37.59
	Mean	130.18	127.28
	Var.	216.93	212.88
	Entropy	-0.64	-0.64
<b>Green</b>	Range	36.76	36.24
	Mean	131.20	133.45
	Entropy	-0.64	-0.64
<b>Blue</b>	Range	42.55	37.95
	Mean	129.29	120.96
	Var.	275.45	216.16
	Entropy	-0.64	-0.64
<b>PCA<sub>1</sub></b>	Range	67.31	1861.22
	Var.	676.44	6.28E+11
	Entropy	-0.65	-0.65
<b>PCA<sub>2</sub></b>	Range	5.79	1800.67
	Entropy	-0.94	-0.85
<b>PCA<sub>3</sub></b>	Range	5.47	1801.50
	Mean	67.52	-247.40
	Var.	4.99	6.28E+11
	Entropy	-0.58	-0.59
<b>Hue</b>	Mean	155.72	112.65
	Var.	2169.04	516.63
<b>Saturation</b>	Range	0.05	0.05
	Mean	0.05	0.12
	Entropy	-0.79	-0.72
<b>Intensity</b>	Range	0	5.61E+14
	Mean	0	0
	Var.	0	0
	Entropy	-0.66	-0.64

Spectral Attributes*		PP	non-PP
		$\bar{X}$	$\bar{X}$
<b>Red</b>	SD	11.38	10.01
	Min.	105.03	109.84
	Max.	154.41	147.73
<b>Green</b>	SD	11.06	9.66
	Min.	106.69	116.59
	Max.	154.70	153.15
<b>Blue</b>	Mean	128.98	121.96
	SD	12.79	10.11
	Min.	101.14	103.36
<b>PCA<sub>1</sub></b>	Mean	223.75	220.70
	SD	20.19	17.09
	Min.	179.74	189.25
	Max.	267.39	253.95
<b>PCA<sub>2</sub></b>	Mean	61.04	67.69
	SD	2.12	1.33
	Max.	65.71	70.20
<b>PCA<sub>3</sub></b>	SD	1.80	1.35
	Min.	63.65	67.37
<b>Hue</b>	Mean	155.62	112.99
	SD	34.93	10.81
	Min.	94.44	94.84
	Max.	228.39	133.42
<b>Saturation</b>	Mean	0.05	0.12
	Min.	0.02	0.09
	Max.	0.10	0.15
<b>Intensity</b>	Mean	0	0
	SD	0	0
	Min.	0	0
	Max.	0	0

\*8-bit

## REFERENCES

- Amiraslani, F., and D. Dragovich. 2013. Image Acquisition for Detection of Vegetation Change Based on Long-Term Rainfall in an Arid Rangeland in Western NSW, Australia. *Environmental Earth Sciences* 70 (1): 83-95.
- Amos, B., and F. R. Gehlbach. 1988. *Edwards Plateau Vegetation: Plant Ecological Studies in Central Texas*. Baylor University Press.  
<http://books.google.com/books?id=w-xyQgAACAAJ>.
- Bastin, G. N., and J. A. Ludwig. 2006. Problems and Prospects for Mapping Vegetation Condition in Australia's Arid Rangelands. *Ecological Management & Restoration* 7: 71-74.
- Batte, C. D. 1984. Soil Survey of Comal and Hays Counties. Soil Conservation Service United States Department of Agriculture.  
[http://www.nrcs.usda.gov/Internet/FSE\\_MANUSCRIPTS/texas/TX604/0/ComalandHays.pdf](http://www.nrcs.usda.gov/Internet/FSE_MANUSCRIPTS/texas/TX604/0/ComalandHays.pdf).
- Bedunah, D. J., and J. P. Angerer. 2012. Rangeland Degradation, Poverty, and Conflict: How Can Rangeland Scientists Contribute to Effective Responses and Solutions? *Rangeland Ecology & Management* 65 (6): 606-612.

- Belgiu, M., and L. Dragut. 2016. Random Forest in Remote Sensing: A Review of Applications and Future Directions. *ISPRS Journal of Photogrammetry and Remote Sensing* 114: 24-31.
- Bemis, S. P., S. Micklethwaite, D. Turner, M. R. James, S. Akciz, S. T. Thiele, and H. A. Bangash. 2014. Ground-Based and UAV-Based Photogrammetry: A Multi-Scale, High-Resolution Mapping Tool for Structural Geology and Paleoseismology. *Journal of Structural Geology* 69 (November): 163-178.
- Bestelmeyer, B. T. 2006. Threshold Concepts and Their Use in Rangeland Management and Restoration: The Good, the Bad, and the Insidious. *Restoration Ecology*: 325-329.
- Blanchard, S. D., M. K. Jakubowski, and M. Kelly. 2011. Object-Based Image Analysis of Downed Logs in Disturbed Forested Landscapes Using Lidar. *Remote Sensing* 3 (11): 2420-2439.
- Boltz, S., and G. Peacock. 2002. Ecological Sites: Understanding the Landscape. *Rangelands* 24 (5): 18-21.
- Booth, D. T., and S. E. Cox. 2008. Image-Based Monitoring to Measure Ecological Change in Rangeland. *Frontiers in Ecology and the Environment* 6 (4): 185-190.

- Briske, D. D., S. D. Fuhlendorf, and F. E. Smeins. 2005. State-and-Transition Models, Thresholds, and Rangeland Health: A Synthesis of Ecological Concepts and Perspectives. *Rangeland Ecology & Management* 58 (1): 1-10.
- Browning, D. M., A. S. Laliberte, and A. Rango. 2011. Temporal Dynamics of Shrub Proliferation: Linking Patches to Landscapes. *International Journal of Geographical Information Science* 25 (6): 913-30.
- Brown, J. R. 2010. Ecological Sites: Ecological Sites: Their History, Status, and Future. *Rangelands* 32 (December): 5-8.
- Bryson, M., and S. Sukkarieh. 2011. *Detecting Wheel Cacti by Using Unmanned Aerial Vehicles and Innovative Classification Algorithms*. 11/018. Rural Industries Research and Development Corporation.  
<https://rirdc.infoservices.com.au/downloads/11-018>.
- Cao, J., E. T. Yeh, N. M. Holden, Y. Qin, and Z. Ren. 2013. The Roles of Overgrazing, Climate Change and Policy As Drivers of Degradation of China's Grasslands. *Nomadic Peoples* 17 (2): 82-101.

- Clower, D. F. 1980. "Soil Survey of Brown and Mills Counties, Texas." Soil Conservation Service United States Department of Agriculture.  
[http://www.nrcs.usda.gov/Internet/FSE\\_MANUSCRIPTS/texas/TX602/0/Brown.pdf](http://www.nrcs.usda.gov/Internet/FSE_MANUSCRIPTS/texas/TX602/0/Brown.pdf).
- Crandall, D. J., O. Andrew, S. Noah, and D. P. Huttenlocher. 2013. SfM with MRFs: Discrete-Continuous Optimization for Large-Scale Structure from Motion. *IEEE Transactions on Pattern Analysis & Machine Intelligence* 35 (12): 2841-2853.
- Hanselka, C. W., and J. C. Paschal. 1991. Prickly Pear Cactus: A Texas Rangeland Enigma. *Rangelands* 13 (3): 109-111.
- Dandois, J. P., and E. C. Ellis. 2013. High Spatial Resolution Three-Dimensional Mapping of Vegetation Spectral Dynamics Using Computer Vision. *Remote Sensing of Environment* 136 (September): 259-276.
- Dillard, J. 2005. *White-Tailed Deer Food Habits and Preferences in the Cross Timbers and Prairies Region of Texas*. PWD RP: W7000-1017 (05/05). [Austin, TX]: Texas Parks and Wildlife, c2005.  
<http://libproxy.txstate.edu/login?url=http://search.ebscohost.com/login.aspx?direct=true&db=cat00022a&AN=txi.b1705683&site=eds-live&scope=site>.

- Duraiappah, A.K. 1998. Poverty and Environmental Degradation: A Review and Analysis of the Nexus. *World Development* 26 (12): 2169-2179.  
doi:10.1016/S0305-750X(98)00100-4.
- Easdale, M. H., and S. E. Domptail. 2014. Fate Can Be Changed! Arid Rangelands in a Globalizing World – A Complementary Co-Evolutionary Perspective on the Current ‘desert Syndrome. *Journal of Arid Environments* 100-101 (February): 52-62.
- Eldridge, D. J., R.S.B. Greene, and C. Dean. 2011. Climate Change Impacts on Soil Processes in Rangelands. *Soil Health and Climate Change, Soil Biology* 29: 237-255. [http://dx.doi.org/10.1007/978-3-642-20256-8\\_11](http://dx.doi.org/10.1007/978-3-642-20256-8_11).
- Estornell, J., L. A. Ruiz, and B. Velázquez-Martí. 2011. Study of Shrub Cover and Height Using LIDAR Data in a Mediterranean Area. *Forest Science* 57 (3): 171-179.
- Everitt, J. H., C. L. Gonzalez, M. A. Alaniz, and G. V. Latigo. 1981. Food Habits of the Collared Peccary on South Texas Rangelands. *Journal of Range Management* 34 (2): 141-144.

- Flinders, J. T., D. A. Quinton, and R. G. Horejsi. 1979. Influence of Brush Control on White-Tailed Deer Diets in North-Central Texas. *Journal of Range Management* 32 (2): 93-97.
- Fonstad, M. A., J. T. Dietrich, B. C. Courville, J. L. Jensen, and P. E. Carbonneau. 2013. Topographic Structure from Motion: A New Development in Photogrammetric Measurement. *Earth Surface Processes & Landforms* 38 (4): 421-430.
- Freeman Center. 2015. Weather. [http://www.txstate.edu/freemanranch/weather\\_data.html](http://www.txstate.edu/freemanranch/weather_data.html) (last accessed October 15, 2015).
- Fritz, A., T. Kattenborn, and B. Koch. 2013. UAV-based photogrammetric point clouds—Tree stem mapping in open stands in comparison to terrestrial laser scanner point clouds. *International Archives of the Photogrammetry, Remote Sensing and Spatial Information Sciences*, XL (1/W2): 141-146.  
<http://www.int-arch-photogramm-remote-sens-spatial-inf-sci.net/XL-1-W2/141/2013/isprsarchives-XL-1-W2-141-2013.pdf>.
- Fuhlendorf, S. D., D. D. Briske, and F. E. Smeins. 2001. Herbaceous Vegetation Change in Variable Rangeland Environments: The Relative Contribution of Grazing and Climatic Variability. *Applied Vegetation Science* 4 (2): 177-188.

- Glenn, E., M. S. Smith, and V. Squires. 1998. On Our Failure to Control Desertification: Implications for Global Change Issues, and a Research Agenda for the Future. *Environmental Science and Policy* 1 (January): 71-78.
- Godínez-Álvarez, H., T. Valverde, and P. Ortega-Baes. 2003. Demographic Trends in the Cactaceae. *Botanical Review* 69 (2): 173-203.
- Grant, V., and K. A. Grant. 1979. Hybridization and Variation in the Opuntia Phaeacantha Group in Central Texas. *Botanical Gazette* 40 (2): 208-215.
- Grant, V., and K.A. Grant. 1980. Clonal Microspecies of Hybrid Origin in the Opuntia Lindheimeri Group. *Botanical Gazette* 141 (1): 101-106.
- Grant, V., and K.A. Grant. 1982. Natural Pentaploids in the Opuntia Lindheimeri-Phaeacantha Group in Texas. *Botanical Gazette* 143(1): 117-120.
- Griffith, G., S. Bryce, J. Omernik, and A. Rogers. 2007. "Ecoregions of Texas." Texas Commission on Environmental Quality.  
[http://www.tceq.state.tx.us/assets/public/comm\\_exec/pubs/as/199.pdf](http://www.tceq.state.tx.us/assets/public/comm_exec/pubs/as/199.pdf).
- Guevara, J. C., P. Suassuna, and P. Felker. 2009. Opuntia Forage Production Systems: Status and Prospects for Rangeland Application. *Rangeland Ecology & Management* 62 (5): 428-434.

- Guisan, A., T.C. Edwards, and T. Hastie, 2002. Generalized Linear and Generalized Additive Models in Studies of Species Distributions: Setting the Scene. *Ecological Modelling* 157 (2002): 89-100.
- Harwin, S., and A. Lucieer. 2012. Assessing the Accuracy of Georeferenced Point clouds Produced via Multi-View Stereopsis from Unmanned Aerial Vehicle (UAV) Imagery. *Remote Sensing* 4 (6): 1573-1599.
- Hellesen, T., and L. Matikainen. 2013. An Object-Based Approach for Mapping Shrub and Tree Cover on Grassland Habitats by Use of LiDAR and CIR Orthoimages. *Remote Sensing* 5 (2): 558-583.
- Hernandez, A. J., and R. D. Ramsey. 2013. A Landscape Similarity Index: Multitemporal Remote Sensing to Track Changes in Big Sagebrush Ecological Sites. *Rangeland Ecology & Management* 66 (1): 71-81.
- Hernandez, F., S. E. Henke, N. J. Silvy, and D. Rollins. 2003. The Use of Prickly Pear Cactus as Nesting Cover by Northern Bobwhites. *Journal of Wildlife Management* 67 (2): 417-423.
- Higginbottom, T. P., and E. Symeonakis. 2014. Assessing Land Degradation and Desertification Using Vegetation Index Data: Current Frameworks and Future Directions. *Remote Sensing* 6 (10): 9552-9575.

- Hilker, T., E. Natsagdorj, R. H. Waring, A. Lyapustin, and Y. Wang. 2014. Satellite Observed Widespread Decline in Mongolian Grasslands Largely due to Overgrazing. *Global Change Biology* 20 (2): 418-428.
- Hilty, J., and A. M. Merenlender. 2003. Studying Biodiversity on Private Lands. *Conservation Biology* 17 (1): 132-137.
- Hodlmoser, M., B. Micusik, and M. Kampel. 2013. Sparse Point cloud Densification by Using Redundant Semantic Information. In *Proceedings of the 3<sup>rd</sup> International Conference on 3-D Vision*, Seattle, USA, June 2013.  
[https://www.dropbox.com/s/i9lttu4z48i38h/Hoedlmoser\\_etal-3-DV2013\\_2.pdf](https://www.dropbox.com/s/i9lttu4z48i38h/Hoedlmoser_etal-3-DV2013_2.pdf).
- Hulet, A., B. A. Roundy, S. L. Petersen, R. R. Jensen, and S. C. Bunting. 2014. Cover Estimations Using Object-Based Image Analysis Rule Sets Developed Across Multiple Scales in Pinyon-Juniper Woodlands. *Rangeland Ecology & Management* 67 (3): 318-327.
- Hunt, E. R. Jr., J. H. Everitt, J. C. Ritchie, M. S. Moran, S. T. Booth, G. L. Anderson, P. E. Clark, and M. S. Seyfried. 2003. Applications and Research Using Remote Sensing for Rangeland Management. *Photogrammetric Engineering & Remote Sensing* 69 (6): 675-693.

James, M. R., and S. Robson. 2014. Mitigating Systematic Error in Topographic Models Derived from UAV and Ground-Based Image Networks. *Earth Surface Processes & Landforms* 39 (10): 1413-1420.

King, E. G., and R. J. Hobbs. 2006. Identifying Linkages among Conceptual Models of Ecosystem Degradation and Restoration: Towards an Integrative Framework. *Restoration Ecology* 14 (3): 369-378.

Klebenow, D. A., and G. M. Gray. 1968. Food Habits of Juvenile Sage Grouse. *Journal of Range Management* 21 (2): 80-83.

Laliberte, A. S., J. E. Herrick, A. Rango, and C. Winters. 2010. Acquisition, Orthorectification, and Object-Based Classification of Unmanned Aerial Vehicle (UAV) Imagery for Rangeland Monitoring. *Photogrammetric Engineering & Remote Sensing* 76 (6): 661-672.

Laliberte, A. S., and A. Rango. 2009. Texture and Scale in Object-Based Analysis of Subdecimeter Resolution Unmanned Aerial Vehicle (UAV) Imagery. *IEEE Transactions on Geoscience & Remote Sensing* 47 (3).

[http://libproxy.txstate.edu/login?url=http://search.ebscohost.com/login.aspx?direct=true&db=edsagr&AN=edsagr.US201400042368&site=eds-live&scope=site.](http://libproxy.txstate.edu/login?url=http://search.ebscohost.com/login.aspx?direct=true&db=edsagr&AN=edsagr.US201400042368&site=eds-live&scope=site)

Laliberte, A. S., and A. Rango. 2011. Image Processing and Classification Procedures for Analysis of Sub-Decimeter Imagery Acquired with an Unmanned Aircraft over Arid Rangelands. *GIScience & Remote Sensing* 48 (1): 4-23.

Laliberte, A. S., A. Rango, and J. Herrick. 2007. Unmanned Aerial Vehicles for Rangeland Mapping and Monitoring: A Comparison of Two Systems. In *Proceeding of ASPRS 2007 Annual Conference*, Tampa, FL.

Laliberte, A. S., A. Rango, and C. Winters. 2011. UAS Remote Sensing Missions for Rangeland Applications. *Geocarto International* 26 (2): 141-156.

Lisein, J., M. Pierrot-Deseilligny, S. Bonnet, and P. Lejeune. 2013. A Photogrammetric Workflow for the Creation of a Forest Canopy Height Model from Small Unmanned Aerial System Imagery. *Forests (19994907)* 4 (4): 922-944.

Lucieer, A., S. Robinson, D. Turner, S. Harwin, and J. Kelcey. 2012. Using a Micro-UAV for Ultra-high Resolution Multi-sensor Observations of Antarctic Moss Beds. In *ISPRS-International Archives of Photogrammetry and Remote Sensing, Spatial Information Sciences*. XXXIX-B1 (July): 429-33.

doi:10.5194/isprsarchives-XXXIX-B1-429-2012.

- Mancini, F., M. Dubbini, M. Gattelli, F. Stecchi, S. Fabbri, and G. Gabbianelli. 2013. Using Unmanned Aerial Vehicles (UAV) for High-Resolution Reconstruction of Topography: The Structure from Motion Approach on Coastal Environments. *Remote Sensing* 5 (12): 6880-6898.
- Mathews, A. J., and J. L. R. Jensen. 2013. Visualizing and Quantifying Vineyard Canopy LAI Using an Unmanned Aerial Vehicle (UAV) Collected High Density Structure from Motion Point cloud. *Remote Sensing* 5 (5): 2164-2183.
- Maynard, C. L., R. L. Lawrence, G. A. Nielsen, and G. Decker. 2007a. Ecological Site Descriptions and Remotely Sensed Imagery as a Tool for Rangeland Evaluation. *Canadian Journal of Remote Sensing* 33 (2): 109–15. doi:10.5589/m07-014.
- Maynard, C. L., R. L. Lawrence, G. A. Nielsen, and G. Decker. 2007b. Modeling Vegetation Amount Using Bandwise Regression and Ecological Site Descriptions as an Alternative to Vegetation Indices. *GIScience & Remote Sensing* 44 (1): 68-81. doi:10.2747/1548-1603.44.1.68.
- McKeon, G. M., G. S. Stone, J. I. Syktus, J. O. Carter, N. R. Flood, D. G. Ahrens, D. N. Bruget, C. R. Chilcott, D. H. Cobon, R. A. Crowley, S. J. Crimp, G. W. Fraser, S. M. Howden, P. W. Johnston, J. G. Ryan, C. J. Stokes, and K. A. Day. 2009. Climate Change Impacts on Northern Australian Rangeland Livestock Carrying Capacity: A Review of Issues. *The Rangeland Journal* 31 (1): 1-29.

- Meadows, M. E., and M. T. Hoffman. 2002. The Nature, Extent and Causes of Land Degradation in South Africa: Legacy of the Past, Lessons for the Future? *Area* 34 (4): 428-437.
- Mitchell, J. J., N. F. Glenn, T. T. Sankey, D. R. Derryberry, M. O. Anderson, and R. C. Hruska. 2011. Small-Footprint Lidar Estimations of Sagebrush Canopy Characteristics. *Photogrammetric Engineering & Remote Sensing* 77 (5): 521-530.
- Mundt, J. T., D. R. Streutker, and N. F. Glenn. 2006. Mapping Sagebrush Distribution Using Fusion of Hyperspectral and Lidar Classifications. *Photogrammetric Engineering & Remote Sensing* 72 (1): 47.
- Oliensis, J. 2000. A Critique of Structure-from-Motion Algorithms. *Computer Vision & Image Understanding* 80 (2): 172-214.
- Olsoy, P. J., N. F. Glenn, and P. E. Clark. 2014. Estimating Sagebrush Biomass Using Terrestrial Laser Scanning. *Rangeland Ecology & Management* 67 (2): 224-228.
- Olsoy, P. J., N. F. Glenn, P. E. Clark, and D. R. Derryberry. 2014. Aboveground Total and Green Biomass of Dryland Shrub Derived from Terrestrial Laser Scanning. *ISPRS Journal of Photogrammetry and Remote Sensing* 88 (February): 166-173.

- Peña, J. M., J. Torres-Sánchez, A. I. de Castro, M. Kelly, and F. López-Granados. 2013. Weed Mapping in Early-Season Maize Fields Using Object-Based Analysis of Unmanned Aerial Vehicle (UAV) Images. *Plos One* 8 (10): e77151-e77151. doi:10.1371/journal.pone.0077151.
- Penner, M., D.G. Pitt, and M.E. Woods. 2013. Parametric vs. Nonparametric LiDAR Models for Operational Forest Inventory in Boreal Ontario. *Canadian Journal of Remote Sensing* 39 (5): 426-443.
- Pintus, R., E. Gobbetti, and R. Combet. 2011. Fast and Robust Semi-Automatic Registration of Photographs to 3-D Geometry. In *Proceedings of the 12th International Conference on Virtual Reality, Archaeology and Cultural Heritage*, 9-16. Prato, Italy: Eurographics Association.
- Folse, L. J., and K. A. Arnold. 1978. Population ecology of Roadrunners (*Geococcyx californianus*) in South Texas. *The Southwestern Naturalist* 23 (1): 1-27.
- Powell, A. M., and J. F. Weedin. 2001. Chromosome Numbers in Chihuahuan Desert Cactaceae. III. Trans-Pecos Texas. *American Journal of Botany* 88 (3): 481-485.

Previtali, M., L. Barazzeti, and M. Scaioni. 2011. Multi-Step and Multi-Photo Matching for Accurate 3-D Reconstruction. In International Archives of Photogrammetry, Remote Sensing and Spatial Information Sciences Commission III-WG/1, Photogrammetric Image Analysis, 38 (3/W22): 103-108.

Quinton, D. A., and A. K. Montei. 1977. Preliminary Study of the Diet of Rio Grande Turkeys in North-Central Texas. *The Southwestern Naturalist* 22 (4): 550-553.

Rango, A., A. Laliberte, J. E. Herrick, C. Winters, K. Havstad, C. Steele, and D. Browning. 2009. Unmanned Aerial Vehicle-Based Remote Sensing for Rangeland Assessment, Monitoring, and Management. *Journal of Applied Remote Sensing* 3 (1): 033542–033542 – 15. doi:10.1117/1.3216822.

Reeves, M. C., and J. E. Mitchell. 2011. Extent of Coterminous US Rangelands: Quantifying Implications of Differing Agency Perspectives. *Rangeland Ecology & Management* 64 (6): 585-597.

Reyes-Agüero, J. A., J. R. Aguirre R., and A. Valiente-Banuet. 2006. Review: Reproductive Biology of *Opuntia*: A Review. *Journal of Arid Environments* 64 (January): 549-585.

- Riaño, D., E. Chuvieco, S. L. Ustin, J. Salas, J. R. Rodríguez-Pérez, L. M. Ribeiro, D. X. Viegas, J. M. Moreno, and H. Fernández. 2007. Estimation of Shrub Height for Fuel-Type Mapping Combining Airborne LiDAR and Simultaneous Color Infrared Ortho Imaging. *International Journal of Wildland Fire* 16 (3): 341-348.
- Ricketts, T. H. 1999. *Terrestrial Ecoregions of North America: A Conservation Assessment*. Ecoregions Assessments Series. Island Press.  
[http://books.google.com/books?id=DRI\\_RhheUhQC](http://books.google.com/books?id=DRI_RhheUhQC).
- Sankey, J. B., D. J. Law, D. D. Breshears, S. M. Munson, and R. H. Webb. 2013. Employing Lidar to Detail Vegetation Canopy Architecture for Prediction of Aeolian Transport. *Geophysical Research Letters* 40 (9): 1724-28.  
doi:10.1002/grl.50356.
- Sant, E. D., G. E. Simonds, R. D. Ramsey, and R. T. Larsen. 2014. Assessment of Sagebrush Cover Using Remote Sensing at Multiple Spatial and Temporal Scales. *Ecological Indicators* 43 (August): 297-305.
- Sayre, N. F., W. deBuys, B. T. Bestelmeyer, and K. M. Havstad. 2012. 'The Range Problem' After a Century of Rangeland Science: New Research Themes for Altered Landscapes." *Rangeland Ecology & Management* 65 (6): 545-552.

- Scalise, J. L. 2011. Food Habits and Selective Foraging by the Texas Tortoise (*Gopherus berlandieri*). <https://digital.library.txstate.edu/handle/10877/2496>.
- Short, H. L. 1977. Food Habits of Mule Deer in a Semidesert Grass-Shrub Habitat. *Journal of Range Management* 30(3): 206-229.
- Western Energy and Land Use Team, (USA), and Henry L. Short. 1985. "Habitat suitability index models." *Biological Report (USA) AGRIS, EBSCOhost* (accessed February 26, 2015).
- Spaete, L. P., N. F. Glenn, D. R. Derryberry, T. T. Sankey, J. J. Mitchell, and S. P. Hardegree. 2010. Vegetation and Slope Effects on Accuracy of a LiDAR-Derived DEM in the Sagebrush Steppe. *Remote Sensing Letters* 2 (4): 317-326.  
doi:10.1080/01431161.2010.515267.
- Sparks, D. R. 1968. Diet of Black-Tailed Jackrabbits on Sandhill Rangeland in Colorado. *Journal of Range Management* 21 (4): 203-208.
- Sperlich, M., T. Kattenborn, B. Koch, and G. Kattenborn. 2014. Potential of Unmanned Aerial Vehicle Based Photogrammetric Point clouds for Automatic Single Tree Detection. *International Archives of the Photogrammetry, Remote Sensing & Spatial Information Sciences* (40-43): 139-144.  
<http://www.dgpf.de/neu/Proc2014/proceedings/papers/Beitrag270.pdf>.

- Streutker, D. R., and N. F. Glenn. 2006. LiDAR Measurement of Sagebrush Steppe Vegetation Heights. *Remote Sensing of Environment* 102 (January): 135-145.
- Su, J., and E. Bork. 2006. Influence of Vegetation, Slope, and Lidar Sampling Angle on DEM Accuracy. *Photogrammetric Engineering & Remote Sensing* 72 (11): 1265-1274.
- Svoray, T., A. Perevolotsky, P. M. Atkinson. 2013. Ecological Sustainability in Rangelands: The Contribution of Remote Sensing. *International Journal of Remote Sensing* 34 (17): 6216-6242.
- Talbot, C. J., S. B. Campbell, M. Hansen, and A. B. Price. 2010. Information Technologies and Ecological Site Descriptions. *Rangelands* 32 (6): 55-59.
- Taylor, R. B., and E. C. Hellgren. 1997. Diet of Feral Hogs in the Western South Texas Plains. *The Southwestern Naturalist* 42 (1): 33-39.
- Tiznado-Hernandez, M. E., J. Fortiz-Hernandez, A.J. Ojeda-Contreras, and A. Rodriguez-Felix. 2010. Use of the Elliptical Mathematical Formula to Estimate the Surface Area of Cladodes in Four Varieties of *Opuntia ficus-indica*. *Journal of the Professional Association for Cactus Development* 12: 98-109.

- Tomasi, C., and J. Zhang. 1996. Is Structure-From-Motion Worth Pursuing? In *Robotics Research*, edited by Georges Giralt and Gerhard Hirzinger, 391–400. Springer London. [http://dx.doi.org/10.1007/978-1-4471-0765-1\\_42](http://dx.doi.org/10.1007/978-1-4471-0765-1_42).
- Tonkin, T.N., N.G. Midgley, D.J. Graham, and J.C. Labadz. 2014. The Potential of Small Unmanned Aircraft Systems and Structure-from-Motion for Topographic Surveys: A Test of Emerging Integrated Approaches at Cwm Idwal, North Wales. *Geomorphology* 226 (December): 35-43.
- Trucco, E., and A. Verri. 1998. Motion. In *Introductory Techniques for 3-D Computer Vision*. New Jersey: Prentice Hall.
- Turner, D., A. Lucieer, and C. Watson. 2011. Development of an Unmanned Aerial Vehicle (UAV) for Hyper Resolution Vineyard Mapping Based on Visible, Multispectral and Thermal Imagery. In *International Symposium on Remote Sensing of Environment 2011*, 10 April-15 April 2011, Sydney, Australia.
- Turner, D. A., A. Lucieer, and C. Watson. 2012. An Automated Technique for Generating Georectified Mosaics from Ultra-High Resolution Unmanned Aerial Vehicle (UAV) Imagery, Based on Structure from Motion (SfM) Point clouds. *Remote Sensing* 4 (5): 1392-1410.

- Twidwell, D., B. W. Allred, and S. D. Fuhlendorf. 2014. Summary of a National-Scale Assessment of the Ecological Site Description (ESD) Database. *Rangelands* 36 (4): 13-17.
- Ueckert, D. N., W. P. Meinzer, and J. T. Flinders. 1975. Foodniche of Coyotes in the Rolling Plains of Texas. *Journal of Range Management* 28 (1): 22-27.
- Vermeire, L. T., and A. D. Roth. 2011. Research Articles: Plains Prickly Pear Response to Fire: Effects of Fuel Load, Heat, Fire Weather, and Donor Site Soil. *Rangeland Ecology & Management* 64 (July): 404-413.
- Villamil, M. B., N. M. Amiotti, and N. Peinemann. 2001. Soil Degradation Related to Overgrazing in the Semi-Arid Southern Caldenal Area of Argentina. *Soil Science* 166 (7): 441-452.
- Volotao, C. F. de Sa, L.V. Dutra, and R. D. C. Santos. 2012. Image Segmentation with Image and Shape Phase Analysis. In *Proceedings of the 4th GEOBIA*, 598–601. Rio de Janeiro, Brazil. <http://mtc-m18.sid.inpe.br/col/sid.inpe.br/mtc-m18/2012/05.18.14.45/doc/167.pdf?languagebutton=en>.
- Volotao, C. F. de Sa. 2013. Image Segmentation Using IHS Space and Object-Based Analysis. Doctorate in Applied Computing, San Jose: MCT/INPE. <http://urlib.net/8JMKD3MGP7W/3-DDRPP>.

- Von Wehrden, H., J. Hanspach, P. Kaczensky, J. Fischer, and K. Wesche. 2012. Global Assessment of the Non-Equilibrium Concept in Rangelands. *Ecological Applications* 22 (2): 393-399.
- Wallace, L. 2013. Assessing the Stability of Canopy Maps Produced from UAV-LiDAR Data. *2013 IEEE International Geoscience & Remote Sensing Symposium - IGARSS*, January, 3879.
- Wallace, L., A. Lucieer, C. Watson, and D. Turner. 2012. Development of a UAV-LiDAR System with Application to Forest Inventory. *Remote Sensing* 4 (6): 1519-1543.
- Wang, X., P. Felker, A. Paterson, Y. Mizrahi, A. Nerd, and A. Mondragon-Jacobo. 1996. Cross-Hybridization and Seed Germination in Opuntia Species. *J.PACD*: 49-60.
- Wang, Y. 2011. *A Comparison Study of Five 3-D Modeling Systems Based on the SfM Principles*. Technical Report TR 2011-01. Visualsize Inc.  
[http://www.visualsize.com/tutorial/VS\\_TR.pdf](http://www.visualsize.com/tutorial/VS_TR.pdf).
- Wendel, A., A. Irschara, and H. Bischof. 2011. Automatic Alignment of 3-D Reconstructions Using a Digital Surface Model. *2011 IEEE Computer Society Conference on Computer Vision & Pattern Recognition Workshops (CVPRW)*, January, 29.

- West, N. E. 2003. Theoretical Underpinnings of Rangeland Monitoring. *Arid Land Research and Management* 17 (4): 333-3346. doi:10.1080/713936112.
- Westoby, M. J., J. Brasington, N. F. Glasser, M. J. Hambrey, and J. M. Reynolds. 2012. 'Structure-from-Motion' Photogrammetry: A Low-Cost, Effective Tool for Geoscience Applications. *Geomorphology* 179 (0): 300-314. doi:10.1016/j.geomorph.2012.08.021.
- Whitehead, K., C. H. Hugenholtz, S. Myshak, O. Brown, A. LeClair, A. Tamminga, T. E. Barchyn, B. Moorman, and B. Eaton. 2014. Remote Sensing of the Environment with Small Unmanned Aircraft Systems (UASs), Part 2: Scientific and Commercial Applications. *Journal of Unmanned Vehicle Systems* 02 (03): 86-102. doi:10.1139/juvs-2014-0007.
- Zarco-Tejada, P. J., R. Diaz-Varela, V. Angileri, and P. Loudjani. 2014. Tree Height Quantification Using Very High Resolution Imagery Acquired from an Unmanned Aerial Vehicle (UAV) and Automatic 3-D Photo-Reconstruction Methods. *European Journal of Agronomy* 55 (April): 89-99.
- Zhang, C., Z. Xie, and D. Selch. 2013. Fusing Lidar and Digital Aerial Photography for Object-Based Forest Mapping in the Florida Everglades. *GIScience & Remote Sensing* 50 (5): 562-573.

Zuur, A.F., E. Ieno, N. Walker, A. Saveliev, G. Smith. 2009. Limitations of Linear Regression Applied on Ecological Data. In *Mixed Effects Models and Extensions in Ecology with R. Statistics for Biology and Health*, 11-33. New York: Springer-Verlag.